Plate Boundary and Volcano Deformation in the Azores Analyzed by Satellite-based Geodetic Techniques

Tese de Doutoramento

João Pedro Martins Teixeira d'Araújo

Doutoramento em

Geologia

Ponta Delgada
2022

Plate Boundary and Volcano Deformation in the Azores Analyzed by Satellite-based Geodetic Techniques

Tese de Doutoramento

João Pedro Martins Teixeira d'Araújo

Orientadores

Professora Doutora Teresa de Jesus Lopes Ferreira

Professor Doutor Freysteinn Sigmundsson

Tese especialmente elaborada para obtenção do grau de Doutor em Geologia

This research was supported by FRCT – Regional Foundation for Science and Technology

João d'Araújo was supported by Ph.D. Grant from Regional Foundation for Science and Technology (ACORES-10-5369-FSE-00000)

Ao meu filho.

“Tudo o que ouvimos é uma opinião, não um facto. Tudo o que vemos é uma perspectiva, não a verdade.” Marco Aurélio

Contents

List of Figures

List of Tables

Abstract

Ground deformation in the Azores, at the triple junction between the Eurasian, Nubian, and North American plates, has been mapped with GNSS (Global Navigation Satellite System) and InSAR (Interferometric Synthetic Aperture Radar) satellite-based geodetic measurements to improve tectonic motion estimates and for understanding volcanic unrest. Time-dependent coordinates, spanning a maximum of more than 20 years (2000-2022), from more than 100 GNSS stations were computed and analyzed. Of these GNSS stations, about 20 were operated continuously across the Azores, and 80 were operated episodically on the São Miguel Island. InSAR data from São Miguel Island (2017-2019) and São Jorge (2022) was analyzed. Results from the continuous GNSS stations show that the Eurasian-Nubian plate boundary in the Azores behaves as a diffuse ultra-slow oblique spreading center with focused deformation found in the Central Group and São Miguel islands. The velocity field obtained from data of the continuous GNSS stations (2000-2016) was modeled by approximating segments of the Eurasian-Nubian plate boundary with vertical rectangular dislocations with right-lateral motion and opening below a locking depth. Best-fit models have a deep motion that accounts for almost half of predicted Eurasian-Nubian relative plate motion. The velocity field obtained from data of the GNSS stations of São Miguel Island (2004-2016) shows in more detail the spreading focused in the central area of the island. Inferred ground deformation from GNSS data from São Miguel Island shows transient volcanic deformation in Fogo volcano, with periods of inflation in 2004-2006, 2011-2013, and a deflation period in 2013-2016. The velocity field from Fogo volcano was modeled using sources of pressure change embedded within uniform elastic half-space. The best fit modeled sources are located near the eastern and northeastern rim of the Fogo caldera,

and to the east of it, at depths of 3.2-3.7 km. A combined GNSS and InSAR data analysis shows renewed inflation at Fogo volcano in 2018-2019. A combined analysis of GNSS and InSAR data reveals that at São Jorge Island in 2022, after 60 years of repose, magma reached almost the surface within a few hours of the seismicity onset with no precursory signals. Results from analysis of geodetic data show that a sudden diking event occurred below São Jorge Island, with transient deformation recorded over two weeks and higher seismicity recorded during months after the start of the activity. The geodetic data from São Jorge was modeled using a segmented vertical dyke with multiple opening patches, with best-fit results indicating a maximum opening of more than one meter in two different areas, at 4-6 km and 7-9 km depth.

Resumo

A deformação crustal nos Açores, na junção tripla entre as placas Eurasiática, Africana e Norte Americana, foi mapeada através das técnicas de medição geodésicas espaciais GNSS (*Global Navigation Satellite System*) e InSAR (*Interferometric Synthetic Aperture Radar*) para melhorar as estimativas de movimento tectónico e a compreensão de crises vulcânicas na região. As posições de mais de 100 estações GNSS, abrangendo um período de mais de 20 anos (2000-2022), foram calculadas e analisadas. Das 100 estações, cerca de 20 foram operadas continuamente em várias ilhas dos Açores e 80 foram operadas episodicamente em São Miguel. Foram também analisados dados InSAR de São Miguel (2018-2019) e São Jorge (2022). Os resultados das estações GNSS contínuas localizadas nas várias ilhas mostram que a fronteira entre as placas Eurasiática e Africana nos Açores se comporta como um centro de expansão oblíquo, ultra-lento e difuso, com deformação focalizada encontrada no Grupo Central e em São Miguel. O campo de velocidade obtido a partir dos dados das estações GNSS contínuas (2000-2016) foi modelado, aproximando-se segmentos da fronteira entre as placas Eurasiática e Africana nos Açores a deslocamentos rectangulares verticais embutidos em profundidade com movimento de desligamento direito e abertura. Os deslocamentos rectangulares verticais modelados que refletem deformação à superfície com melhor ajuste às observações refletem um movimento que corresponde aproximadamente a metade do movimento relativo entre as placas Eurasiática e Africana previsto por modelos de tectónica de placas. O campo de velocidade obtido a partir de dados GNSS das estações de São Miguel (2004-2016) mostra com maior detalhe o movimento de expansão centrado na ilha. O campo de velocidade mostra também deformação vulcânica transiente na zona central da ilha, com períodos de inflação em

2004-2006, 2011-2013, e um período de deflação em 2013-2016. O campo de velocidade da zona central de São Miguel obtido a partir dos dados GNSS foi modelado usando fontes de pressão embutidas num semi-espaço elástico uniforme. As fontes de pressão modeladas que refletem deformação à superfície com melhor ajuste às observações estão localizadas perto da borda leste e nordeste da caldeira do Fogo, e a leste dela, a profundidades na ordem de 3.2-3.7 km. A análise combinada de dados GNSS e InSAR mostra uma nova inflação no vulcão do Fogo em 2018-2019. A análise combinada de dados GNSS e InSAR mostra que em São Jorge em 2022, após 60 anos de repouso, magma atingiu quase a superfície poucas horas após o início da sismicidade e sem sinais precursores. Os resultados da análise de dados geodésicos de São Jorge mostram que uma intrusão através de um dique ocorreu por baixo da ilha, com deformação transiente registada por um período de duas semanas e sismicidade alta registada durante vários meses após o início da atividade. Os dados geodésicos de São Jorge foram modelados usando um dique vertical segmentado com múltiplos fragmentos rectangulares com movimento de abertura. O dique segmentado modelado que reflete deformação à superfície com melhor ajuste às observações indica abertura máxima de mais de um metro em duas áreas diferentes, a 4-6 km e 7-9 km profundidade.

Acknowledgements

This document is the result of several years of research work, including data collection during GNSS surveys and management of continuous GNSS stations in the field, as well as curation and analysis of extended data sets in the laboratory and presentation of results and interpretations. Many individuals and institutions supported this project during all the stages of the research. I take this opportunity to acknowledge and convey my gratitude to everyone that contributed to this project and especially the following:

- ***Prof. Freysteinn Sigmundsson*** for his impeccable availability, patience, and tireless effort during countless hours spent reviewing the manuscript. His immense knowledge, great sensitivity to express ideas more clearly, and suggestion of analysis techniques and interpretations were fundamental for improving the manuscript. He also had an important motivational role, with his great care during numerous online meetings and when showing appreciation for my capabilities during hard times.

- ***Prof. Teresa Ferreira***, who was greatly responsible for the conclusion of this work with her patience, knowledge, and support in all matters, from bureaucratic tasks to comprehensive reviews of the manuscript. She had a crucial leadership role in creating bridges with other contributors and managing discussion meetings, especially during the São Jorge unrest. I also want to thank her for her care and understanding of personal issues in the last months of the thesis project.

- ***Dr. Jun Okada*** for all his support during his stay at São Miguel. I am grateful to him for sharing knowledge about the GNSS technique, including using GNSS

equipment, data collection and curation, data processing, analysis, and interpretation of results. He also had a major role in the management and operation of GNSS surveys, and data curation.

- ***Maria Lorenzo***, for her friendship and great companionship. I appreciate the good moments we shared during our laboratory and field work tasks, her relaxed nature, and her spontaneity. She was instrumental in the extended GNSS data curation and management and operation of GNSS surveys.

- ***Dr. Andy Hooper*** and ***Dr. Milan Lazecky*** from Leeds University for their collaboration and enthusiasm during the São Jorge unrest. I appreciate their availability and openness in sharing data sets from InSAR and results from LICSAR software, modeling strategies, and numerous productive discussions about interpretations that were crucial to the conclusion of the São Jorge unrest chapter.

- ***FRCT – Regional Foundation for Science and Technology*** for their financial support during the PhD.

- ***REPRAA – Rede de Estações Permanentes da Região Autónoma dos Açores*** and especially ***Marlene Antunes***, for her readiness support for transferring GNSS data-sets and clarifying metadata issues.

- ***Bernese staff*** and especially ***Pierre Fridez*** for his availability to help solve problems related to GNSS data processing using Bernese software.

- ***Dr. Xiaohua Xu*** for his availability and detailed explanations regarding processing InSAR data sets using the GMTSAR software.

- ***IVAR – Instituto de Vulcanologia e Avaliação de Riscos*** and ***CIVISA – Centro de Informação e Vigilância Sismovulcânica dos Açores*** to pro-

vide the conditions, logistics, and access to equipment and data needed for the realization of the project. I would like to recognize the important contribute from all the board members of IVAR and CIVISA, and in particular ***Dr. Rui Marques***, director of CIVISA, for his prompt availability for managing the resolution of all kinds of technical difficulties that occurred during the work.

- All the ***Professors*** and ***Researchers*** in the Department of Geosciences that influenced my academic career by supporting with their knowledge and especially professor ***João Luís Gaspar***, for inviting and encouraging me to do research in geodesy.

- All members of CIVISA and IVAR that contributed directly and indirectly, and especially all operators responsible for the location of seismic events used in this study.

- All engineering staff responsible for preparing, maintaining, and installing equipment. I would like to highlight the role of ***Engº. Carlos Primo*** for his tireless support with computer issues and his immense patience, especially when dealing with a bad mood on my part. I would also like to appreciate ***Ernesto Sousa*** and ***Vitor Sousa*** for their technical support regarding often heavy-duty tasks from GNSS fieldwork.

- ***Dr. Rita Silva*** for her support with seismic data and manuscript reviews. I appreciate her sharing of the seismic data sets and explanations regarding methodology details.

- ***Dr. Rita Carmo*** for her comprehensive reviews and words of encouragement.

- ***Patrícia Raposo*** and ***Rui Correia*** for helping with endless bureaucratic tasks.

- ***João Carvalho*** for his collaboration in the discussion of ideas, suggestions, and especially his friendship.
- All operators that participated in the GNSS surveys and especially ***Maxim Pavlov***, ***Luís Cabral*** and ***Miguel Barreto***, for their companionship and fun moments during extended hours of fieldwork.
- My close family and friends, for their encouragement and all conditions provided along the years that allowed me to conclude this thesis. A special thanks to them, and especially my mother, for their understanding during periods of intense work and absence and for the enormous support provided in all matters that allowed me to spend more time working on the project.

Preamble

This thesis comprises a set of integrated studies in the Azores archipelago about crustal deformation. The main focus is the study of plate spreading in the region and volcano deformation in two areas: São Miguel and São Jorge islands. Two techniques of space geodesy are used to study crustal deformation, the Global Navigation Satellite System (GNSS) and the Interferometric Synthetic Aperture Radar (InSAR).

The GNSS, a ground-based technique used worldwide in most volcano observatories, has been used in the Azores for over 20 years. The InSAR is a remote sensing technique also used worldwide but with few applications in the Azores until recently. The lack of applications of InSAR technique has been due to technical constraints, namely the low number of available images of the region and high decorrelation of the images due to dense vegetation, and challenging atmospheric conditions. When successfully applied, the combination of GNSS and InSAR techniques allows a good tracking in time and space of volcano deformation evolution during volcano unrest episodes.

This study of crustal deformation in the Azores addresses both the plate motion and transient volcano deformation and the relationship between both processes. For the first time, the combination of the GNSS and InSAR techniques to measure volcano deformation is successfully implemented in the Azores in two case studies, in the Fogo volcano (São Miguel Island) and São Jorge Island. The study contributes to a better understanding of volcano deformation during recent unrest episodes in the two areas and gives insights into magmatic processes. In addition to combined GNSS and InSAR data results, other significant results using only the GNSS technique are obtained. It is shown that the Eurasian-Nubian plate boundary in the Azores behaves as a diffuse ultra-slow oblique spreading center with focused deformation in the Central Group

islands and the central part of São Miguel Island. Inflation was mapped at Fogo volcano, São Miguel Island for the 2003-2006, 2011-2013, and 2018-2019 periods due to magma intrusion or mixed magma-hydrothermal processes.

GNSS data from more than 20 years is analyzed in the study, including continuous and episodic GNSS data from 2000 to 2022. The continuous GNSS data is from stations installed permanently across the Azores islands, and the episodic GNSS data is from stations observed periodically on São Miguel Island. The GNSS data is used to study the regional tectonic motion and transient volcano deformation at São Miguel and São Jorge islands. In addition, InSAR data is analyzed and integrated with the available GNSS data to study volcano unrest at Fogo in 2018-2019 and São Jorge in 2022. Multiple methods are used in the data analysis. Velocities are computed and modeled using analytical inversion techniques to estimate subsurface sources that explain the deformation. Other data, such as locations of earthquakes, are also integrated into the analysis. Information from other studies in geodesy, seismicity, petrology, and other fields is also used.

The first chapter, *General Introduction*, provides a literature review of the study area. The first section of this chapter describes the geologic setting and geodynamics of the area, including the Azores in general in the first sub-section and, in particular, São Miguel and São Jorge islands in the second and third sub-sections, respectively. The second section of the first chapter presents information about historical seismic and volcanic activity in the Azores and, in particular, São Miguel and São Jorge islands. The second chapter, *Methods*, describes instrumentation used in each technique, data collection, and analysis. This chapter is divided into three sections, *GNSS Data and Processing*, *InSAR Data and Processing*, *Modeling*, and *Seismic Data*. The *GNSS Data and*

Processing section is divided into sub-sections, including *Continuous GNSS Stations*, *Episodic GNSS Stations*, *GNSS Data Processing*, *Time Series Analysis*, and *Velocity Estimation*. The *InSAR Data and Processing* section is divided into two sub-sections that explain the procedures used to analyze the InSAR data using two programs, *GMTSAR* and *LICSAR*. In the sub-section *Modeling*, information about modeling the geodetic data is presented, including about plate spreading, Fogo volcano and São Jorge deformation modeling. The results and interpretations are presented in three chapters, including *Eurasian-Nubian Plate Spreading*, *Fogo Volcano Deformation*, and *São Jorge Volcano Deformation*. The *Eurasian-Nubian Plate Spreading* chapter presents results from spreading in the Azores, and includes sub-chapters *Azores Inter-Island Spreading*, *São Miguel Intra-Island Spreading*, and *Discussion*. The first sub-chapter *Azores Inter-Island Spreading* is divided in three parts, including the presentation of velocities in the ITRF2014 reference frame, velocities detrended from predicted tectonic motion, and modeling results. The *Fogo Volcano Deformation* presents results from multiple transient deformation episodes in the Fogo volcano, which are divided into sub-sections, including *Time-Series and Seismicity*, *Modeling*, *Velocity Field*, and *Discussion*. The *Velocity Field* sub-chapter is divided into several parts related with different periods of activity at Fogo volcano, including *2004-2006 Inflation*, *2007-2011 Stable Period*, *2011-2013 Inflation*, *2013-2016 Deflation*, and *2018-2019 Inflation*. The chapter *São Jorge Volcano Deformation* shows results from the 2022 deformation episode in São Jorge Island. This chapter is divided into sub-chapters where results are presented, including about *Seismicity*, *GNSS*, *InSAR*, and *Modeling*. A *Discussion* sub-chapter is also included. In the last chapter *Conclusions*, the main findings and conclusions from the study are presented.

1 General Introduction

1.1 Geologic Setting and Geodynamics

1.1.1 Azores

The Azores comprises nine islands of volcanic nature located in the Atlantic Ocean between latitudes of 37-40° N and longitudes of 25-31° W (Figure 1.1). The islands are geographically distributed in three groups: the Corvo and Flores islands form the Western Group, while Graciosa, Terceira, São Jorge, Faial, and Pico islands form the Central Group, and São Miguel and Santa Maria form the Eastern Group. São Jorge Island is located in the middle of the Central Group between latitudes 38.5-38.8° N and longitudes 28.4-27.7° W. São Miguel Island is the northern-most island of the Eastern Group located between latitudes 37.7-37.9° N and longitudes 25.1-25.9° W. The islands emerge from the so-called Azores platform, an area of anomalously thickened crust roughly defined by the 2000 m isobath (Needham & Francheteau, 1974). The crustal thickness in the Azores is estimated to be 14-17 km (Escartin et al., 2001; Spieker et al., 2018).

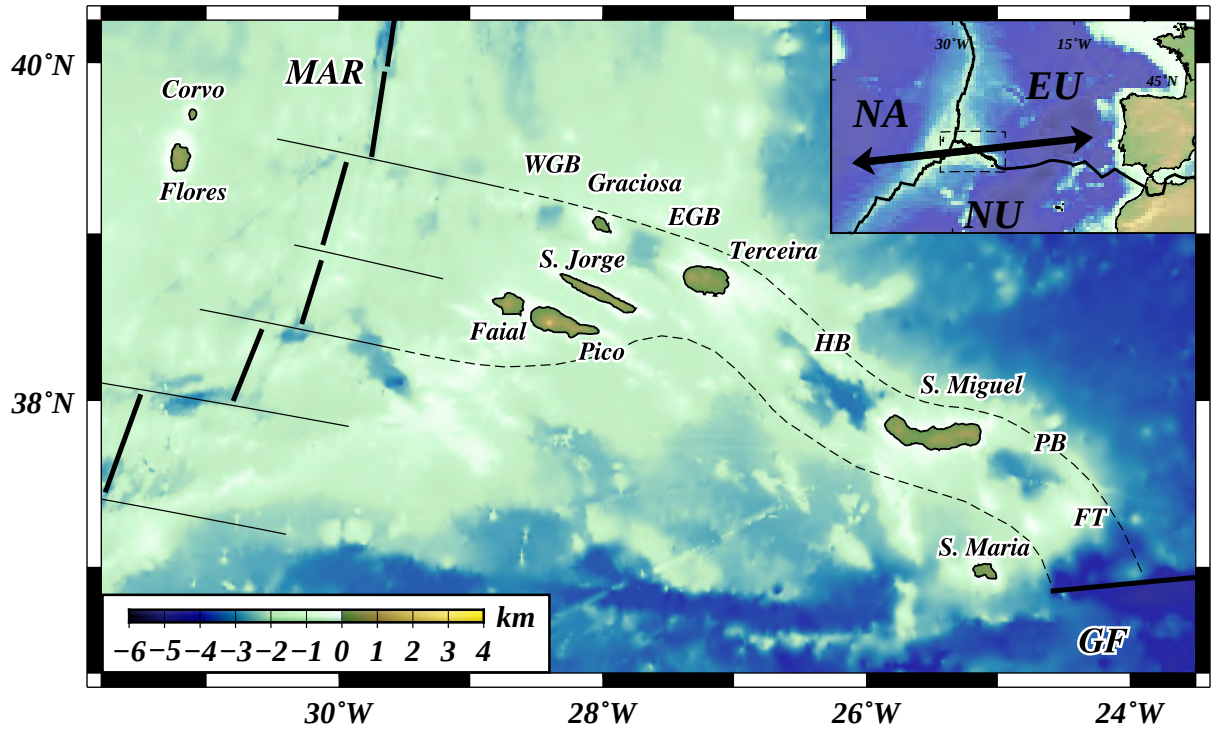

Figure 1.1: Overview of the tectonic setting of the Azores Plateau roughly defined by the 2000 m isobath. MAR segments are represented by heavy black lines and the intersecting fracture zones by narrow black lines (Luis et al., 1994). The Terceira Rift comprises, from west to east, the West Graciosa Basin (WGB), Graciosa Island, East Graciosa Basin (EGB), Terceira Island, Hirondelle Basin (HB), São Miguel Island, Povoação Basin (PB) and Formigas Through (FT). The Gloria Fault (GF) is located east of Santa Maria Island. The GF and plate boundaries (inset) (DeMets et al., 2010) are represented by heavy black lines. The dashed lines delimit a proposed area of the Eurasian-Nubian inter-plate deformation zone. The bathymetric and topographic data have been derived from 30 arc seconds resolution digital elevation model (Becker et al., 2009). The arrows in the inset show the opening rate of 4.7 ± 0.1 mm yr^{-1} in the direction of N(88.0 ± 3.8)°E between EU and NU plates according to the ITRF2014 plate motion model (Altamimi et al., 2017), calculated at the average location of all GNSS sites to the east of MAR. Modified from D'Araújo et al. (2022).

The Azores is located in the junction where the American, Eurasian, and Nubian tectonic plates meet, leading to the existence of important fracture systems in the region, namely the Mid-Atlantic Ridge and the Terceira Rift. The Mid-Atlantic Ridge (MAR) constitutes the boundary between the North American and the other two plates, crossing the Azores between the Western and Central Group islands. The MAR is an oceanic spreading ridge that displays a gradual increase of the opening velocity from the southern limit of the Azores Plateau to the northern limit, with opening velocities of 19.5 mm yr^{-1} and 22.8 mm yr^{-1} calculated at 38° N and 40° N points, respectively, using the MORVEL model (DeMets et al., 2010). It comprises six segments between 37° N and 40° 30' N, each varying in length from 50 to 60 km, and separated by transform faults of general direction E-W (Luis et al., 1994). From lower to higher latitudes, there is a gradual change in the direction of the MAR from NE-SW to NS.

The Central and Eastern group islands, to the east of MAR, lie in a zone of intense seismic and volcanic activity, in an area with general WNW-ESE direction. The so-called Terceira Rift (TR) (Machado, 1959; Searle, 1980) is an important geological structure east of the MAR. It comprises a series of basins alternating with volcanic highs aligned NW-SE to WNW-ESE direction. The TR extends from the west of Graciosa Island to Formigas Through between 36°48'N/24°30'W and 39°20'N/28°50'W. From NW to SE, the TR includes the West Graciosa Basin, Graciosa Island, East Graciosa Basin, Terceira Island, Hirondelle Basin, São Miguel Island, Povoação Basin and Formigas Through. To the south of the TR, other geological structures extend from the east of the MAR, including the São Jorge and Faial-Pico alignments which have a general WNW-ESE direction defined by the main orientation of the islands and their volcanic systems, and adjacent submarine volcanic ridges.

While the boundary between the North American plate and the other two plates in the Azores domain is well defined by the MAR, the location, spatial extension, and kinematics of the boundary between the Eurasian and Nubian plates are still uncertain. Previous GNSS (Global Navigation Satellite System) geodetic measurements in the Azores show that to the east of the MAR, Graciosa and Santa Maria islands have displacements close to predicted Eurasian and Nubian motion, respectively. In contrast, the other islands display an intermediate motion (D'Araújo et al., 2022; Fernandes et al., 2006). Spreading at the Eurasian-Nubian plate boundary is accommodated in a broad area between the MAR and the Gloria Fault, including Faial, Pico, São Jorge, Terceira, and São Miguel islands. According to plate motion models based on geologic and geodetic data (Altamimi et al., 2017; Argus et al., 2010; DeMets et al., 2010), the predicted plate spreading between the Eurasian and Nubian plates in the Azores is slow compared to most active plate spreading regions, with velocity of the Eurasian plate with respect to the Nubian plate in the range of 4.2-4.8 mm yr^{-1} and direction of N(73-88)°E. The plate boundary is highly oblique to this direction with a strike ranging N(45-75)°W. The plate spreading between the Eurasian and Nubian plates is accommodated in a complex deformation zone with right-lateral shear and extension. Observations from morpho-tectonic analysis (Lourenço et al., 1998) and previous campaign GNSS surveys in the Central Group islands (Fernandes et al., 2006; Marques et al., 2013), and São Miguel Island (J. Okada et al., 2015; Trota et al., 2006) show evidence that the Eurasian-Nubian boundary is diffuse, with strain focusing in some areas accommodating most of the spreading.

1.1.2 São Miguel Island

São Miguel is the largest island in the Azores archipelago. It has an E-W elongated shape and is 64 km long and 8-15 km wide. The maximum elevation of 1103 m is located in the eastern part of the island. The geology and volcanism of São Miguel Island have been extensively studied (e.g. Croasdale et al., 1978; Ferreira, 2000; Guest et al., 1999; Moore, 1990; Queiroz, 1997; Wallenstein, 1999). There are three active central volcanoes on the island, each containing a prominent caldera containing a lake: Sete Cidades, Fogo (Água de Pau), and Furnas (Figure 1.2). The Sete Cidades volcano is located on the western part of São Miguel Island, while Fogo and Furnas volcanoes are located in the central and eastern parts of the island, respectively (Moore, 1990). Two volcanic fissure zones link these three active volcanoes, the Picos fissure zone between Sete Cidades and Fogo volcanoes and the Achada das Furnas (Congro) fissure zone between Fogo and Furnas volcanoes. The inactive Povoação volcano is located east of Furnas volcano and is the oldest part of São Miguel Island. Most faults on São Miguel Island are normal and strike NW or WNW, parallel to the Terceira Rift (Carmo et al., 2015; Ferreira et al., 2015).

Previous studies using data from episodic GNSS measurements (Jónsson et al., 1999; Sigmundsson et al., 1995; Trota et al., 2006) and continuous GNSS measurements (D'Araújo et al., 2022; J. Okada et al., 2015) show that the eastern and western parts of São Miguel Island are moving away from each other, with a relatively small area in the central part of the island accommodating spreading motion between the Eurasian and Nubian plates.

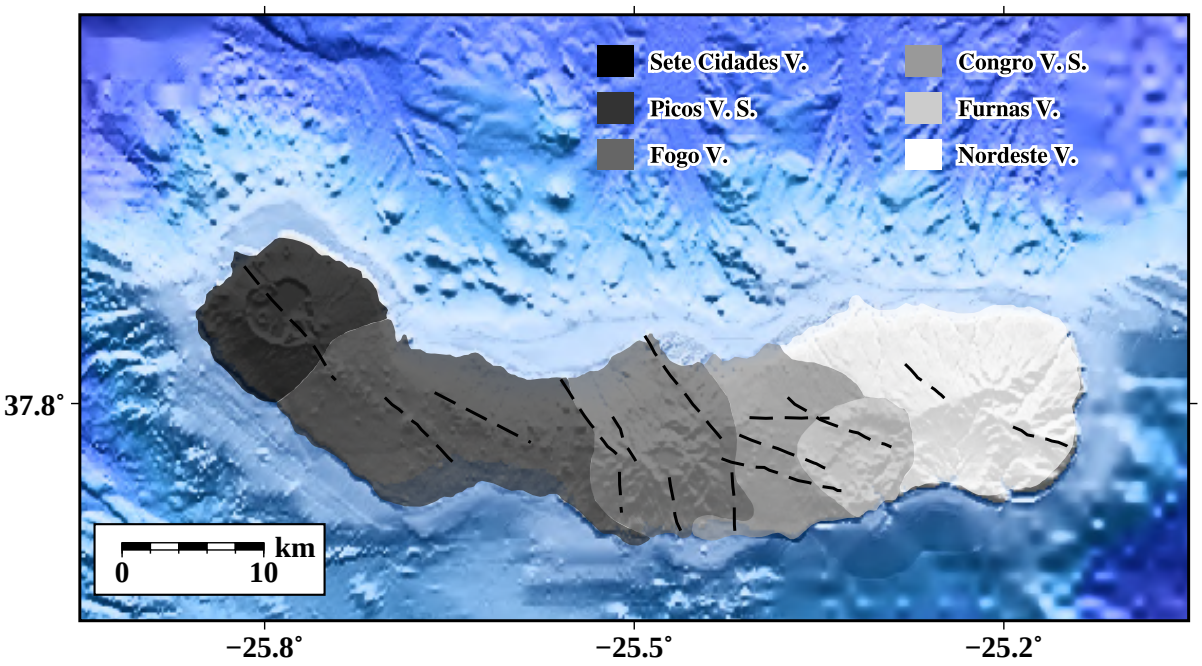

Figure 1.2: Volcanic map of São Miguel with gray areas representing the central volcanoes (Sete Cidades, Fogo, Furnas, and Povoação) and volcanic fissure zones (Picos and Congro) (Moore, 1990). Dashed lines represent the main fault zones of the island (Carmo et al., 2015). The bathymetric and topographic data have been derived from EMODnet portal (EMODnet, 2022).

.

The geology of the Fogo (Água de Pau) volcano has been extensively studied (e.g., Croasdale et al., 1978; Moore, 1990; Walker & Croasdale, 1971; Wallenstein, 1999). Fogo volcano rises to almost 1 km above sea level and contains a summit caldera, partially occupied by Fogo lake. A predominant NW–SE to NNW–SSE trending fault system crosses the volcano (Carmo et al., 2015). This direction is particularly evident in the northern part of the volcano from the volcanic alignments extending from the coast to the summit area. Several volcanic forms exist on Fogo, including scoria and pumice cones, hydro-volcanic forms, lava flows and domes (Wallenstein, 1999).

Geothermal fields are exploited on the north flank of Fogo volcano and supply two power plants. The geothermal wells exploit three different aquifers that reach up to ∼1.5 km depth (Carvalho et al., 2006). According to studies based on geological, geophysical, and geochemical data (Duffield & Muffler, 1984; Gandino et al., 1985), the deep hot water from the hydrothermal system convects upward beneath the upper north flank of the volcano. The hot water supplies an area of lateral outflow in the subsurface that links with the aquifers at lower altitudes. An hydrothermal system at 1 km depth and a magma chamber at depths of around 4 or 5 km are inferred from an anomalous low-density body observed from gravity inversion below the Fogo caldera (Camacho et al., 1997). A study using seismic tomography (Zandomeneghi et al., 2008) has, however, not found anomalies that can be related to magma at shallow depth.

1.1.3 São Jorge Island

São Jorge is a particularly long and narrow island, approximately 55 km long and 7 km wide, reaching a maximum altitude of 1053 m at Pico da Esperança, in the central part of the island (Figure 1.3). High and steep sea cliffs characterize São Jorge Island. In some coastline areas, there are rocky platforms locally known as "Fajãs," where the steepness of the cliffs decreases in the direction of the sea. Some of these result from the pilling up of lava flow reaching the sea, others from rock debris accumulation due to landslides. Most population lives in these areas. Several geological studies (Hildenbrand et al., 2008; Marques et al., 2018; P. Silva et al., 2012) reveal that the peculiar elongated shape of São Jorge Island and the existence of high coastal cliffs is related to flank instability resulting from a large number of dyke intrusions parallel to the trend of the island. It has been suggested that dykes have intruded major pre-existing fractures and control the internal structure of the island, compartmentalized by large unstable blocks assembled from the near-vertical emplacement of the dyke intrusions (Hildenbrand et al., 2008).

Estimated velocities from episodic GNSS measurements in São Jorge show intra-island deformation (Marques et al., 2013; Mendes et al., 2013). Results show that the NW sector of the island moves at a rate of 1.1 mm/yr to N53ºE relative to the SE sector (Mendes et al., 2013), suggested to be related to local volcanic processes or seafloor spreading occurring to the west of the island.

Based on stratigraphic studies, there are three volcanic fissure zones on São Jorge Island (Forjaz & Fernandes, 1975; Madeira & da Silveira, 2003), the older Topo fissure zone in the eastern part of the island, the Rosais fissure zone in the western part and the younger

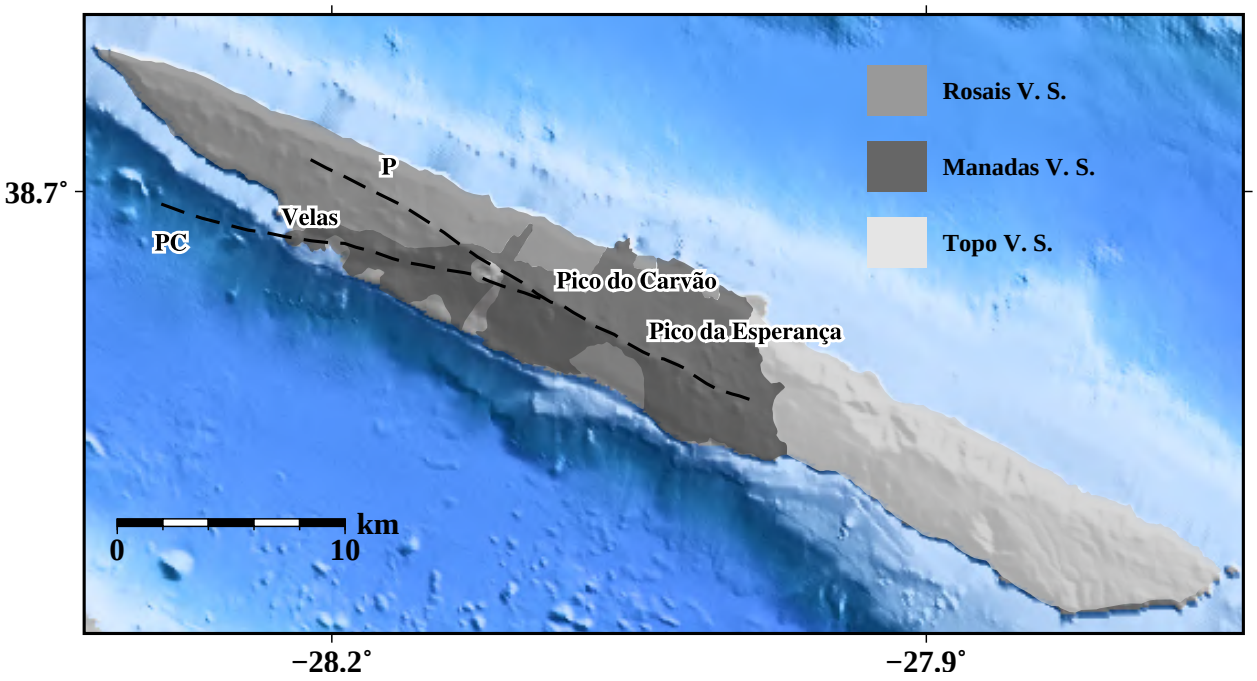

Figure 1.3: Volcanic map of São Jorge Island with gray areas representing the volcanic systems (Rosais, Manadas, and Topo) (Madeira & da Silveira, 2013). Dashed lines represent the main fault zones of Picos (P), and Pico do Carvão (PC). The bathymetric and topographic data have been derived from EMODnet portal (EMODnet, 2022).

Manadas fissure zone that partially overlays the other two units.

The shape of São Jorge and adjacent submarine volcanic ridges display the main orientation of the Eurasian-Nubian plate boundary. The main fault zones on the island also display this orientation, namely the Picos and Pico do Carvão normal-dextral WNW-ESE fault zones that dominate the younger western half of the island (Madeira & da Silveira, 2003). The Picos Fault Zone crosses the island in an N115°E direction. The Pico do Carvão Fault Zone has a slightly more eastward direction compared to the Picos Fault Zone with an N105°E direction. The Pico do Carvão Fault Zone extends from Pico do Carvão cinder cone, where it merges with the Picos Fault Zone, to Velas and to the site of the 1964 submarine eruption to the west (Madeira & da Silveira, 2003).

1.2 Seismic and Volcanic Activity

1.2.1 Azores

Reports of seismic locations show that larger tectonic earthquakes in the east of the Mid-Atlantic Ridge (M>4) have been occurring almost entirely in rift basins away from the islands (Borges et al., 2007; Gaspar et al., 2015). On the other hand, seismic events on the islands typically have lower magnitudes, as reported during periods of volcano unrest (D'Araújo et al., 2022; J. Okada et al., 2015; R. Silva et al., 2012).

Most higher magnitude tectonic earthquakes with estimated focal mechanisms are consistent with normal faulting (e.g. Bezzeghoud et al., 2014; Borges et al., 2007; Buforn et al., 1988) along WNW–ESE and NNW–SSE trends, with magnitudes in the range of 5-7 (Borges et al., 2007; Nunes & Ribeiro, 2001).

Since the fifteenth century, at least 31 destructive earthquakes and 28 volcanic eruptions (Figure 1.4) have been recorded in the Azores (Gaspar et al., 2015). Major earthquakes often triggered landslides and even small tsunamis. Subaerial volcanic eruptions range from Hawaiian to sub-Plinian types. Most seismic activity is located on the Mid-Atlantic Ridge, the Terceira Rift, and the Faial-Pico alignment towards the Mid-Atlantic Ridge. Some areas are more affected by seismic activity than others. For example, the central area of São Miguel Island has experienced increased seismic activity during volcanic unrest (D'Araújo et al., 2022; J. Okada et al., 2015; R. Silva et al., 2012). On the other hand, seismicity in the last decades shows a significant seismic gap in the São Jorge area (Gaspar et al., 2015). In general, recorded seismic and volcanic activity to the east of the Mid-Atlantic Ridge defines a 100 km-wide structure extending roughly with an NW–SE trend from east of Santa Maria

to the west of Graciosa, bending in an E-W direction (Gaspar et al., 2015).

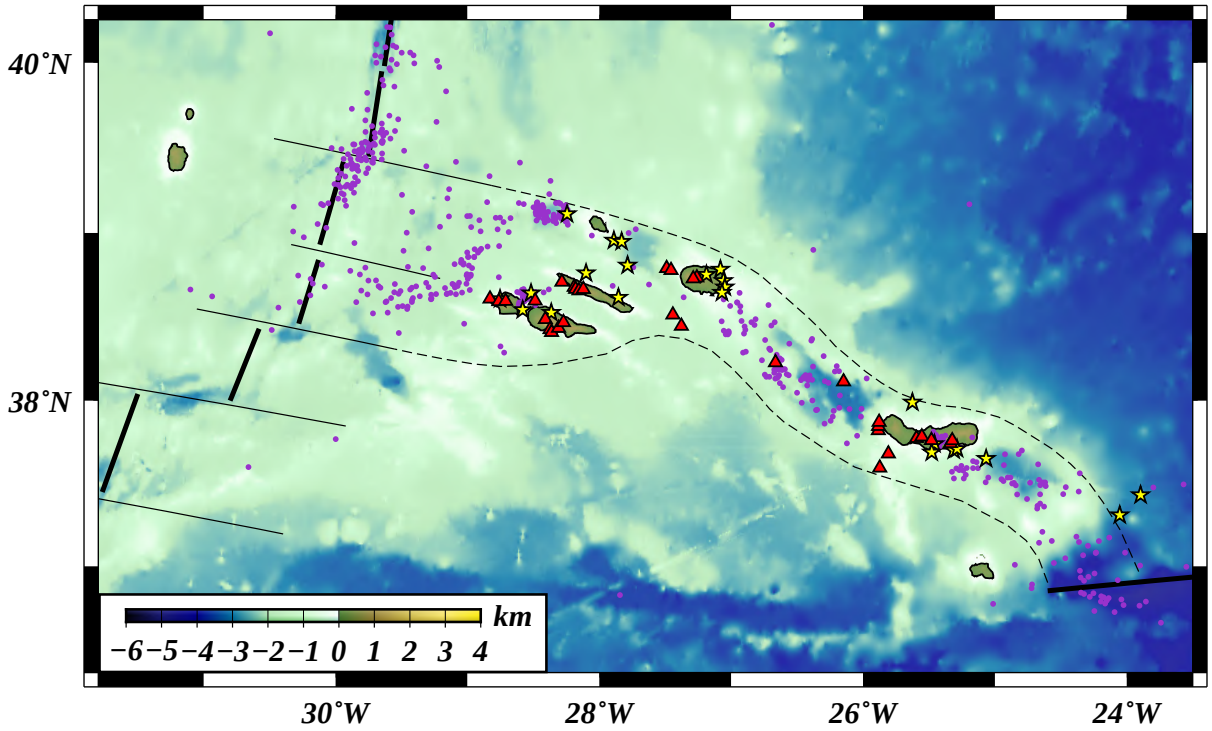

Figure 1.4: Historical seismic and volcanic activity in the Azores. Purple circles are recorded earthquakes ($M_L \geq 3$) between April 2000 and January 2017 (CIVISA database). Yellow stars are historical earthquakes, and red triangles are historical eruptions (Gaspar et al., 2015). The dashed lines delimit a proposed area of the Eurasian-Nubian inter-plate deformation zone (D'Araújo et al., 2022). The bathymetric and topographic data have been derived from 30 arc seconds resolution digital elevation model (Becker et al., 2009).

.

1.2.2 São Miguel Island

Most seismic activity at São Miguel occurs in the central part of the island, at the Fogo-Congro area, which is one of the most seismically active regions of the Azores. In this area, the strongest historical earthquake to affect São Miguel in 1522 triggered a landslide that partially buried the capital of the island at that time, Vila Franca do Campo. In the last century, multiple seismic swarms were recorded in the Fogo-Congro area (Nunes & Oliveira, 1999; Tryggvason et al., 1989). More recently, three unrest episodes occurred in the area, with seismicity and crustal deformation observed, in 2003-2006 (R. Silva et al., 2012; Trota et al., 2006), in 2011-2012 (J. Okada et al., 2015), and in 2018-2019. Different processes have been suggested to be related to the most recent unrest episodes. The 2003-2006 episode in the Fogo volcano is attributed to a magma intrusion (Trota, 2008) or the ascension of hydrothermal fluids from depth to lower levels of the crust (R. Silva et al., 2012). On the other hand, the 2011-2012 episode is attributed to increased pressure in the Fogo volcano and subsequent lateral diffusion of fluids percolating existing fissures at the Congro area to the east (J. Okada et al., 2015).

Some 50 eruptions occurred at São Miguel Island in the last 5000 years, spanning a variety of eruptive styles, from Hawaiian to Plinian types (Croasdale et al., 1978). In historical times, since the 15^{th} century, the last sub-aerial eruptions on Fogo and Furnas volcanoes occurred in 1563 and 1630, respectively (Figure 1.5). In Sete Cidades volcano, several historical submarine eruptions occurred a few kilometers offshore, but there is no clear evidence of sub-aerial activity. Presently, thermal manifestations occur at the surface of the volcanoes, with hot springs on the northern flank of the Fogo volcano and inside the Furnas caldera.

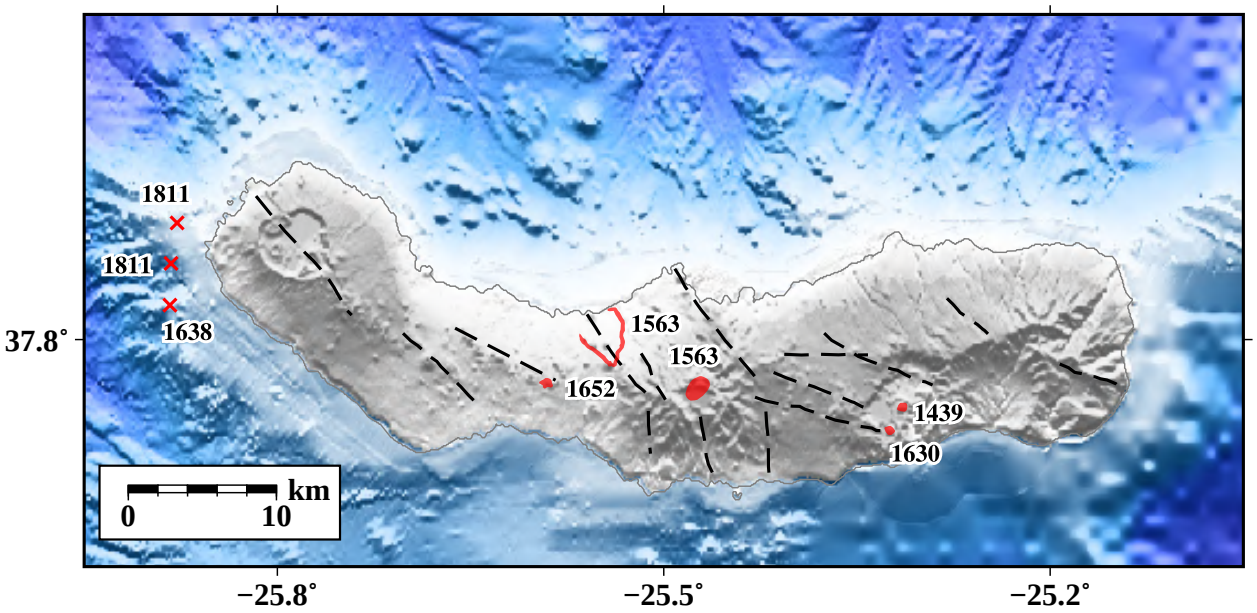

Figure 1.5: Historical eruptive activity in São Mguel Island. Red areas are sub-aerial eruptions, namely the Fogo 1563 effusive flank eruption and explosive caldera eruption (Wallenstein, 1999), the 1652 eruption on Picos volcanic system (Ferreira et al., 2015), and the 1439 and 1630 dome eruptions in the Furnas caldera (Cole et al., 1999). The submarine eruptions in Sete Cidades volcano are marked by red crosses (Gaspar et al., 2015). The bathymetric and topographic data have been derived from EMODnet portal (EMODnet, 2022).

At least six eruptions occurred in the last 5000 years at Fogo, including the 1563 eruption. The last eruption in 1563 was associated with an initial explosive phase inside the caldera and a second effusive phase four days later at the northern flank of the volcano (Wallenstein, 1999). Pumice deposits associated with the 1563 eruption (Walker & Croasdale, 1971) have an estimated volume of $\sim$0.2 km^3.

1.2.3 São Jorge Island

The area between Faial-Pico and Graciosa-Terceira islands, where São Jorge Island is located, has been the stage of some of the strongest historical earthquakes in the Azores. The earthquakes with higher estimated magnitudes closer to São Jorge Island were events related to offshore rupture faults, namely the $M = 7.4$ in 1757, the $M = 7.2$ in 1980, and the $M = 5.8$ in 1998 (Gaspar et al., 2015).

There are records of three eruptions in São Jorge during historical times, two on land in 1580 and 1808, and a probable submarine eruption in 1964 (Figure 1.6). The sequence of volcanic events during the 1580 and 1808 eruptions has been analyzed by interpretation of historical reports and analysis of samples from erupted products (Zanon & Viveiros, 2019). The 1580 and 1808 eruptions occurred along trending fissures in the range of N100-120° that opened for several kilometers. More evolved magma erupted in the initial stages of both eruptions, while more primitive magma erupted in the later stages. It was inferred that un-erupted magma from the 1580 event was stored and evolved at a minimum depth of 16 km before erupting in 1808.

An unrest episode in 1964 was the first to be monitored using instrumental seismology (Machado & Forjaz, 1964; Zbyszewski & Rosa, 1977). The seismic crisis during this episode lasted about ten days. Around 300 earthquakes were felt in the first two days, but afterwards, the frequency of events dropped. In the first three days, the seismicity was located in the central part of São Jorge Island, close to the previous historical eruptive vents. After that, the seismic epicenters migrated to NW. The earthquakes in the central part of the island were shallower at about 5 km depth, while the events in the NW were deeper, in the range of 10-20

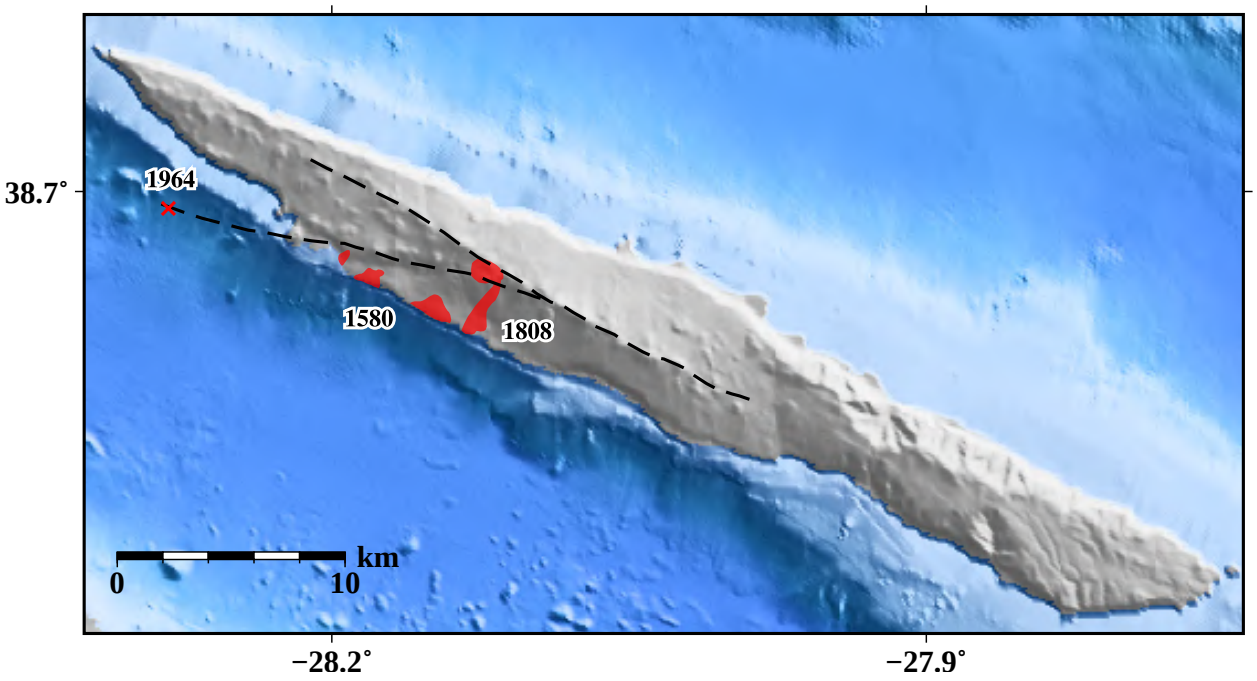

Figure 1.6: Historical eruptive activity in São Jorge Island. Red areas are sub-aerial eruptions (Zanon & Viveiros, 2019). A red cross marks the 1964 submarine eruption (Gaspar et al., 2015). The bathymetric and topographic data have been derived from EMODnet portal (EMODnet, 2022).

km. The strongest recorded earthquake was a 4.8 magnitude event (Gaspar et al., 2015). About 400 buildings were destroyed due to seismic activity, with signs of submarine eruptive activity being reported on the 4^{th} day of activity (Machado & Forjaz, 1964; Zbyszewski & Rosa, 1977).

2 Methods

2.1 GNSS Data and Processing

GNSS refers to any combination of operational space-based navigation systems (Dzurisin, 2007) In this study, the GNSS data was from the GPS (Global Positioning System) and GLONASS (Global Navigation Satellite System) systems. The GNSS technique allows measuring 3-D positions of a station in an absolute reference frame. The positions are obtained by processing with specialized software data recorded on the ground with special equipment and data from an array of satellites (e.g. Dach & Walser, 2015).

A receiver and an antenna occupy each GNSS station. The GNSS satellites transmit a signal that the receiver can decipher. The receiver is attached to the antenna, which is fixed to the ground and tuned to the satellite signals. GNSS satellite signals include dual-frequency phase and pseudo-range data. In order to have millimeter accuracy positioning from GNSS data, it is necessary to process the data and resolve ambiguities in the GNSS signals by using differencing methods. Phase ambiguity is the unknown number of whole wavelengths in the signal between a receiver and a satellite. Double difference methods are used to remove correlated errors and facilitate the phase ambiguity resolution. During the data processing, baselines representing the distance between two receivers are computed to apply differencing methods. Besides ambiguity resolution, several factors affect the quality of observations, such as problems with receiver clock synchronization, temporary loss of tracked signals (cycle slip), antenna phase offsets, and loading effects from ocean tides and troposphere. These factors can be minimized during data processing.

The GNSS stations can be occupied episodically or continuously. The episodic stations

are occupied during surveys. Each station is occupied for a limited time, usually 24-48 hours. After that, the equipment is moved to other network stations until all stations are occupied. The continuous stations are occupied permanently for an extended period of time. The data from local episodic and continuous GNSS stations are processed together with data from an array of fiducial stations, and data from satellite orbits. The fiducial stations are international stations operating continuously, used as a reference to calculate the positions of the local stations in a global reference frame. The time-dependent positions of the local stations in a global reference frame can be detrended from tectonic motion estimates for the area in order to estimate local transient deformation such as volcano deformation.

2.1.1 Continuous GNSS Stations

Data from 19 continuous GNSS stations were used in the current study (Figure 2.1 and Table A1 in Appendix A). Continuous GNSS station measurements in the Azores began in 2000 with the installation of the PDEL station in Ponta Delgada, São Miguel Island. In 2002 RIB1 station (Figure 2.2) was installed on São Miguel Island, and in 2003 three additional stations were installed: QBN1 in São Miguel Island and NOV1 and SRPC on Terceira Island. In 2005, HTN1, PCNG, and RCHA stations were installed on São Miguel Island. On the same island, BVF1 was installed in 2007. A regional continuous GNSS network (REPRAA, 2021) was created by the Azores government to support users interested in precise GNSS data. Three stations were installed in 2008: AZGR on Graciosa Island, FRNS on São Miguel Island, and TERC on Terceira Island. Other three stations started operating in 2009: FLRS on Flores Island, PIED on Pico Island, and VFDC on São Miguel Island. These were followed by the PTRP (AZTP) station installed on Pico Island in 2010, QEMD station on São Jorge

Island in 2012, and HORT station on Faial Island in 2013. The most recent BSRP station was installed on Pico Island in 2018.

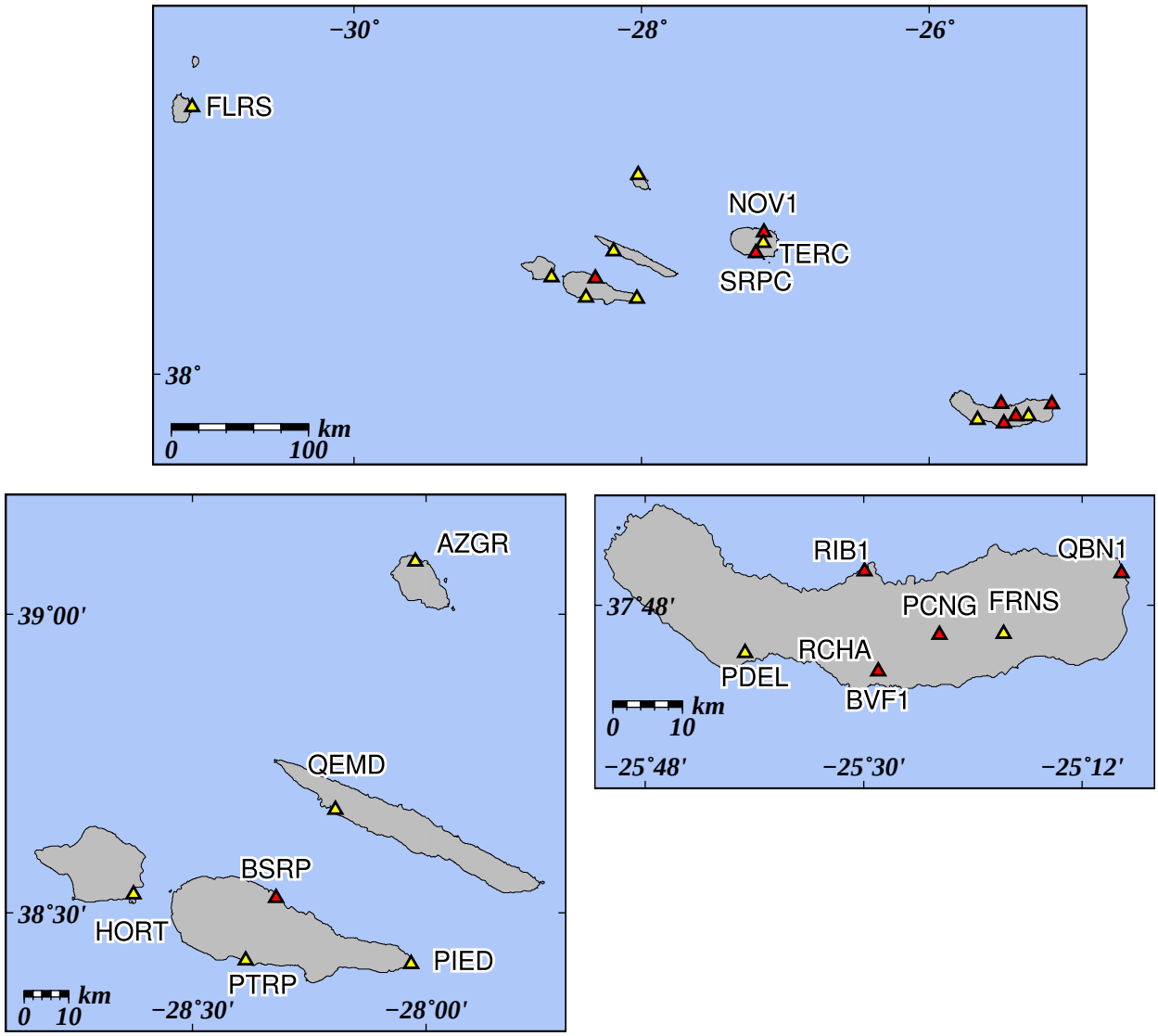

Figure 2.1: Continuous GNSS stations in Azores (Upper), Faial, Pico, São Jorge and Faial (Lower-left), and São Miguel (Lower-right). Red triangles are stations from the CIVISA network and yellow triangles are stations from the REPRAA network. 4-character codes of stations are denoted.

Most of the continuous GNSS monuments of CIVISA (Centro de Informação e Vigilância Sismovulcânica dos Açores) consist of a ∼1-meter high stainless steel rod screwed in a stain-

Figure 2.2: Site of continuous GNSS station RIB1.

less steel benchmark cemented directly into a solid bedrock or a concrete platform with a deep foundation in soil. The benchmarks were leveled during the installation, and the GNSS antennas were fastened to the top of the rod. Choke ring antennas were used, with radomes covering most of them. Some stations are located in public buildings, with antennas fixed at the top, while other stations are located in remote places. Currently, most remote stations contain solar panels, batteries, and data transmission devices. However, some stations have been operated without data transmission devices for several years, and data were collected intermittently. This resulted in data gaps on some stations, especially during the first years of observation. The data files from continuous GNSS stations with data transmission were

downloaded automatically daily via ADSL or digital radio to the CIVISA database.

Continuous GNSS data analyses allow us to discriminate well between long-term displacements, such as plate motion, and local short-term displacements, such as volcano deformation. Compared to continuous GNSS, the data from episodic GNSS observations have several limitations, such as lower temporal resolution, high susceptibility to severe atmospheric conditions, multipath error, and bad satellite geometry, resulting in lower precision of the estimated velocities.

2.1.2 Episodic GNSS Stations

The first episodic GNSS measurements at São Miguel Island were carried out in 1993-1997, with a few GNSS benchmarks installed in the island (Jónsson et al., 1999; Sigmundsson et al., 1995). An effort to increase the GNSS network at São Miguel started in 2000, with new benchmarks installed in the following years (Trota, 2008). Most episodic GNSS stations are stainless steel benchmarks installed directly on bedrock or on top of public buildings, and some stations are geodetic pillars from the Portuguese Geodetic Institute (Figure 2.3).

Data from about 80 episodic GNSS stations was recorded at São Miguel Island between September 2004 and August 2019 (Figure 2.4 and Table A2 in Appendix A). The episodic GNSS stations were measured during annual surveys. Each annual survey lasted around four consecutive weeks, between July and September. Each benchmark was measured between two consecutive days, from around 4 PM on the first day until 2 PM on the following day. Data from each day was analyzed separately. Thus, the episodic GNSS stations have, in general, two daily position estimates per year from consecutive days.

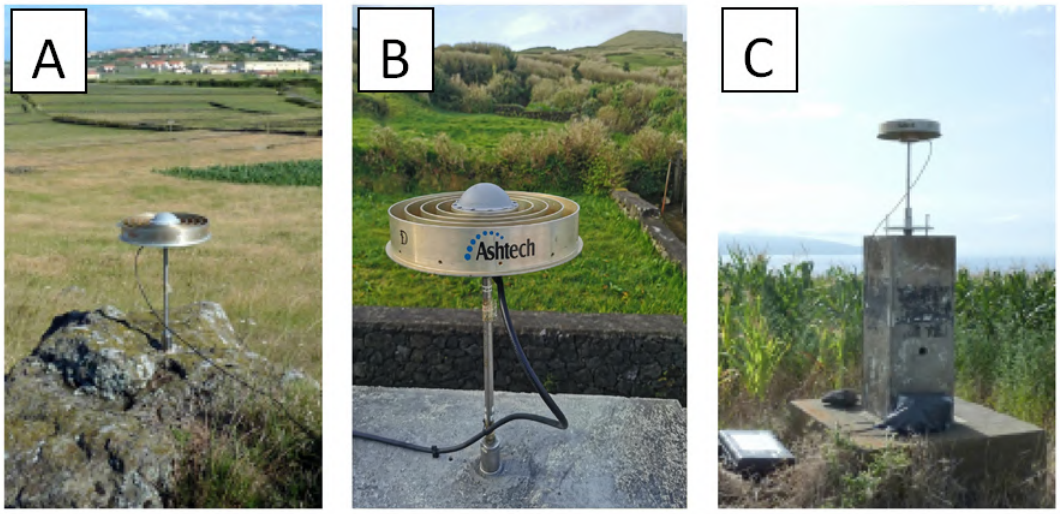

Figure 2.3: Sites of episodic GNSS stations installed directly on bedrock (A), on top of public buildings (B), and on geodetic pillars (B).

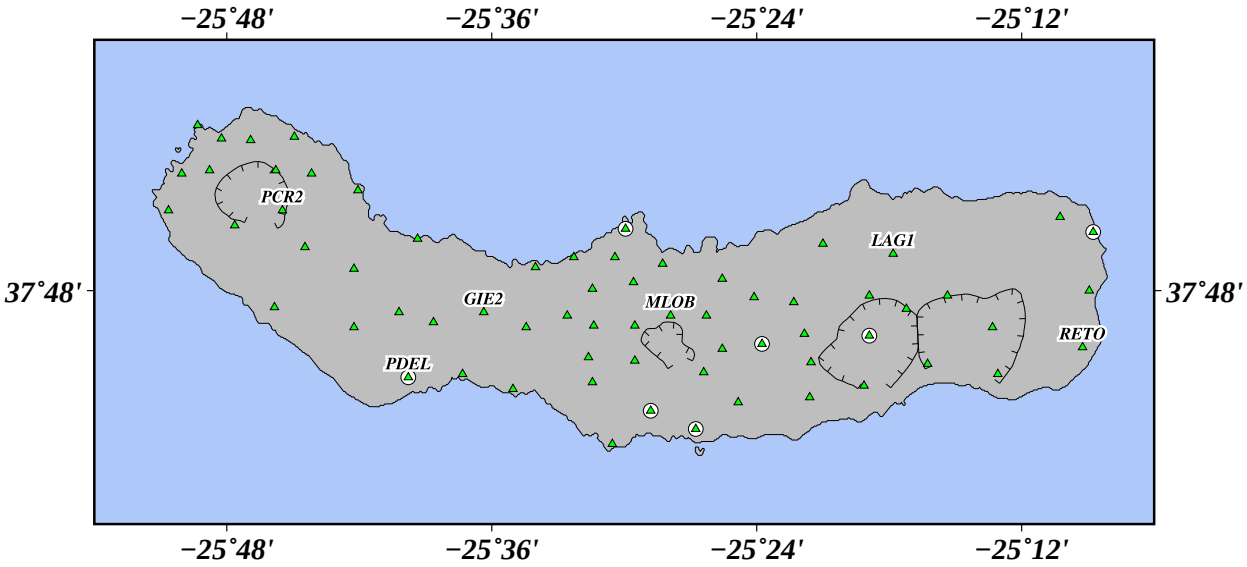

Figure 2.4: GNSS station network of São Miguel Island. Green triangles are episodic GNSS stations. Green triangles with white circles are continuous GNSS stations. The continuous GNSS station PDEL is denoted. The episodic GNSS stations PCR2, GIE2, MLOB, LAG1, and RETO with time series shown in Figure 2.5 are also denoted.

2.1.3 GNSS Data Processing

Dual-frequency phase and pseudo-range data at 30-second intervals were recorded at all GNSS stations in 24-hour-long RINEX-2 files (RINEX version 2), with antenna elevation angle limit set in the range of 5-15°, depending on the local terrain and open-sky visibility.

The daily positions of the GNSS stations were calculated with Bernese 5.2 software (Dach & Walser, 2015) with the RINEX-2 files as input, and reprocessed precise satellite orbits (Selmke et al., 2020) from the Center for Orbit Determination in Europe (CODE) aligned to the ITRF2014 reference frame (Altamimi et al., 2016). Data from about 50 stations from the International GNSS Service (IGS) was also used. The data were analyzed using the following strategy: (1) preprocessing, including receiver clock synchronization and cycle slip correction; (2) initial ionosphere-free analysis with computation, analysis, and removal of residuals; (3) ambiguity resolution scheme using multiple strategies depending on the length of the baseline: Code-Based Widelane (WL), Phase-Based Widelane (L5), Quasi-Ionosphere-Free (QIF) and Direct L1/L2; (4) computation and analysis of station coordinate solutions and uncertainties.

After checking the data quality from the GNSS time series analysis performed by JPL, fiducial stations were selected with data available for the entire study period with no significant gaps and offsets in the time series. All the daily coordinate solutions were transformed into the ITRF2014 reference frame with a 3-parameter Helmert solution imposed on the coordinates of 20 fiducial stations from the IGS (ALGO, BOR1, BREW, DRAO, DUBO, GODE, GODZ, JOZE, MAR6, MATE, NYAL, ONSA, STJO, THU3, WILL, WSRT, WTZR, YEBE, YELL, and ZIMM). The processing utilizes absolute antenna phase center offset models from

the IGS (Schmid et al., 2016), ocean tidal loading effects from FES2004 model (Lyard et al., 2006), troposphere refraction effects from Vienna Mapping Function data (Böhm et al., 2006), and zenith path delay corrections from the European Centre for Medium-Range Weather Forecasts.

2.1.4 Time Series Analysis

The coordinate time series of the continuous GNSS stations resulting from data processing in the ITRF2014 reference frame were evaluated using the FODITS program included in the Bernese 5.2 software. FODITS allows computing functions that fit times series. The functions include four elements: outliers, discontinuities, linear velocities, and periodic functions. A statistical test, based on the defined user level of significance, terminates the analysis when the model adequately represents the time series (Dach & Walser, 2015).

The discontinuities in the time series of continuous GNSS result from equipment changes or ground deformation processes. Known equipment changes at the continuous GNSS stations (see Table A3 in Appendix A) were detected as discontinuities in the time series using FODITS (see Table A4 in Appendix A). Besides these known discontinuities, there are others of unknown origin (see Table A4 in Appendix A). These discontinuities may relate to unreported equipment changes or ground deformation processes. Sometimes, it is impossible to check equipment changes, especially from older data sets and the REPRAA agency stations. Unknown discontinuities were found in the time series of AZGR, PDEL, and SRPC stations located in relatively stable areas where no significant seismic activity was recorded. These discontinuities are sudden and classified as unreported equipment changes. Additional unknown discontinuities were found in the time series of stations located around the

Fogo volcano. These discontinuities are more gradual and occur during the 2003-2006 and 2011-2012 unrest periods of the Fogo volcano, and were classified as ground deformation events.

The amplitudes of the vertical component of the seasonal signals found in the time series (see Table A5 in Appendix A) are small when compared with centimeter-level values found at continuous GNSS stations in other regions of the world, such as Iceland, where water and snow loading effects are large (Drouin et al., 2016). Amplitudes of seasonal signals estimated in this study are in the range of 0.7-1.9 mm in the horizontal components and 0.5-2.1 mm in the vertical component. Seasonal signals are more evident in the north component than in the east and up components. The direction of horizontal annual motion is towards direction of 136° to 170° at most stations. Estimating seasonal signals for the time series of HORT, HTN1, NOV1, and QEMD stations was not possible because of the short period of observations and data gaps.

Besides outliers, discontinuities, and periodic functions, FODITS was used to compute linear velocities (see Table A6 in Appendix A). The time series of most continuous stations, excluding the stations located at Fogo volcano, have a single linear velocity estimation showing that they move at a stable rate. However, stations PDEL, FRNS, and SRPC (see Figure 2.1) have velocity changes, with a maximum rate of 4 mm/yr in the FRNS station. The stations at Fogo volcano have higher velocity changes, in the range of 6-10 mm/yr.

Outliers, discontinuities from equipment changes, and annual seasonal signals computed using FODITS were removed from the time series in the ITRF2014 reference frame. Other discontinuities and velocity changes were not removed from the time series. As an example, the time series of the PDEL station is shown in Figure 2.5 before and after removing outliers,

discontinuities from equipment changes, and annual seasonal signals.

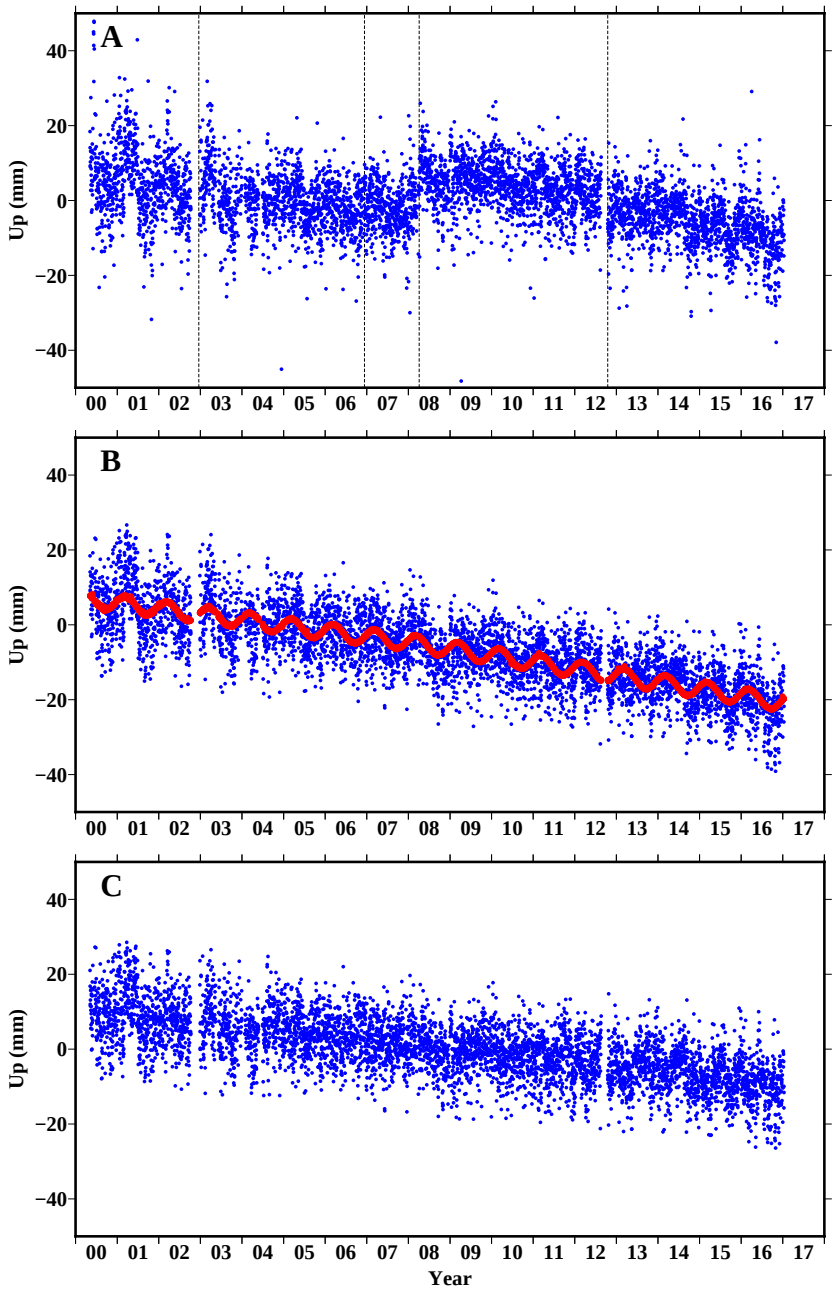

Figure 2.5: Time series of the vertical component of the PDEL station for the period between May 2000 and January 2017, relative to ITRF2014 reference frame with A) all solutions from Bernese 5.2 processing before the time series analysis using FODITS program, B) solutions with filtered-out discontinuities and outliers found from FODITS program analysis, and C) filtered solutions from discontinuities, outliers and seasonal signals found from FODITS program analysis.

The time series of the GNSS stations in the ITRF2014 reference frame were detrended to visualize the local deformation signals better. This was implemented by removing ITRF2014 predicted motion (Altamimi et al., 2017) of a stable plate interior as shown in Figure 2.6. The time series of the FLRS station is relative to predicted stable North American plate motion, while all others are relative to predicted stable Eurasian plate motion.

A global scaling factor estimate for each coordinate uncertainty component was computed by scaling the formal uncertainties estimated in the data processing (Geirsson et al., 2006), using a statistical analysis of the time series of PDEL and QBN1 reference stations. First, a scaling factor was calculated for each reference station. This was done by dividing the standard deviation of the coordinate residuals by the median value of the formal uncertainties. The global scaling factor was calculated by averaging the scaling factors of the two reference stations and was used to scale the formal uncertainties of the other stations.

The time series of episodic GNSS stations of São Miguel Island in the ITRF2014 reference frame for the 2004-2016 period were detrended by removing the ITRF2014 predicted motion of Eurasian plate (Altamimi et al., 2017) as shown in Figure 2.7.

The time series of the continuous GNSS stations used in the São Jorge data analysis in the ITRF2014 reference frame for the 2017-2022 period were detrended by removing the predicted plate motion estimated by the station velocities of the 2000-2016 stable period. For the BSRP station installed in 2018, the velocity of the closest station PTRP was used to detrend. The 2000-2016 velocities were removed from the estimated linear fit of the time series for the period between March 2017 and the initial day of São Jorge activity. The uncertainties of the time series were calculated using the formal uncertainty values obtained from data processing, scaled with the previously computed global scaling factor.

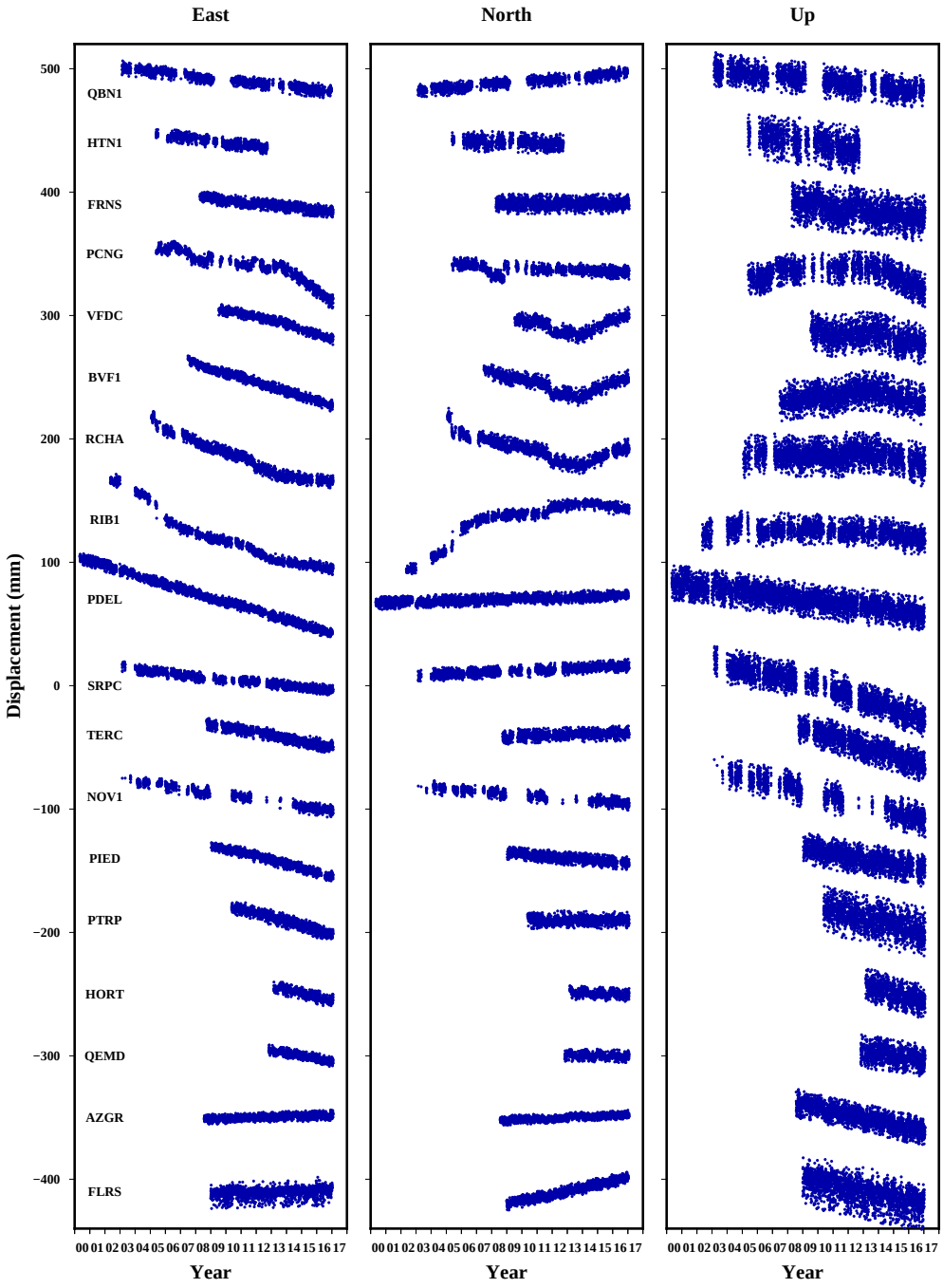

Figure 2.6: Time series of the continuous GNSS stations in east, north, and up components for the period between May 2000 and January 2017, relative to the ITRF2014 plate motion model. The time series of the FLRS station is relative to predicted North American plate motion, while all others are relative to predicted Eurasian plate motion. Reproduced from D'Araújo et al. (2022).

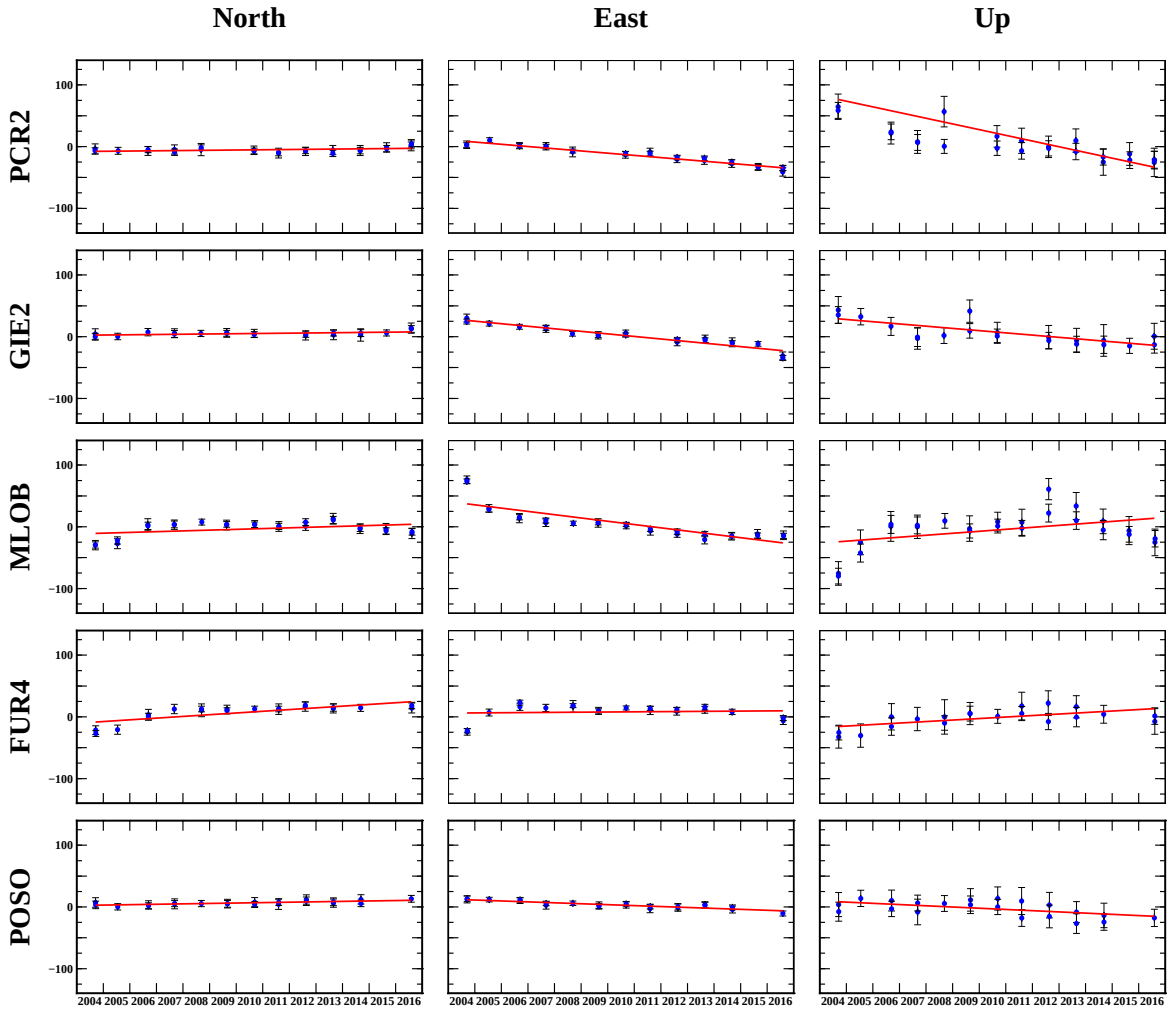

Figure 2.7: Time series of the episodic GNSS stations PCR2, GIE2, MLOB, FUR4, and POSO in east, north, and up components for the period between 2004 and 2016, relative to ITRF2014 predicted motion of Eurasian plate (Altamimi et al., 2017). The stations from top to bottom are located at São Miguel Island from west to east (see Figure 2.4). Blue dots represent the positions of the stations, error bars the standard deviations at the 1σ level and red lines the linear regression estimated to compute velocities.

2.1.5 Velocity Estimation

Velocity maps using GNSS data were computed for different areas, including the Azores network, São Miguel Island network, Fogo Volcano network, and São Jorge Island network.

The velocities of the continuous GNSS stations from the Azores network in the ITRF2014 reference frame for the 2000-2016 period were estimated using linear fitting of the data. Similarly to Geirsson et al. (2006), the velocity uncertainty was estimated from the variance of residuals of the regression and the length of the time series:

$$\sigma_v = \sigma/T \tag{1}$$

Here, σ is the standard deviation of the residuals, and T is the length of the time series in years. A correlation factor between the horizontal velocity error components is computed from the covariance of the residuals. The velocity field was estimated by computing the velocities of the GNSS stations relative to the ITRF2014 predicted motion (Altamimi et al., 2017). The velocity of the FLRS station is relative to predicted stable North American plate motion, while all others are relative to predicted stable Eurasian plate motion.

The velocities of the episodic GNSS stations from São Miguel network in the ITRF2014 reference frame for the 2004-2016 period were estimated with the same strategy used for the continuous GNSS stations.

The velocities of the GNSS stations located at Fogo volcano were not estimated together with the other stations because of the transient disturbances in the time series. The velocities of the GNSS stations from the Fogo volcano network in the ITRF2014 reference frame were calculated between survey periods using the data available from the start date of a specific

survey and the end date of another survey (see Table A7 in Appendix A). In order to have better velocity estimates, only stations with at least two daily position estimates in every year of the period in the analysis were used. The velocity field of the Fogo network was estimated by computing the velocities of the GNSS stations relative to the average velocity of PDEL and QBN1 continuous GNSS stations, used as reference. These two stations are located in areas with no recurrent seismic activity and show stable displacements with no transient deformation.

The velocities of the São Jorge network in the ITRF2014 reference frame were estimated using two methods. For the initial period of activity, the velocity was computed by equating the median displacement between 17-19 March and 20-22 March of 2022 over the period between the two date intervals. For the period afterward, the velocity was estimated using linear fitting of the data from the first 15 days of activity, between 19 March and 3 April. The velocity field of the São Jorge network was estimated by computing the velocities of the GNSS stations relative to the velocities of the stations estimated for the 2000-2016 stable period. For the BSRP station installed in 2018, the velocity of the closest station PTRP was used.

2.2 InSAR Data and Processing

Interferometric synthetic aperture radar (InSAR) is a remote-sensing radar technique that uses two or more synthetic aperture radar (SAR) images to generate maps of surface deformation (Dzurisin, 2007). The satellite systems that collect SAR images employ a sensor that sends out microwaves that backscatter the earth's surface and redirects back toward the sensor. The deformation is obtained by processing with specialized software data recorded from satellite systems with SAR instruments (e.g. Lazecký et al., 2020; Sandwell et al., 2011).

There are several satellite systems with SAR instruments. The Sentinel-1 system, for example, transmits C-band signals with ∼5 cm wavelength. The signals are characterized by two fundamental properties: amplitude and phase. The amplitude is related to the reflective quality of objects on the ground, while the phase is related to the distance between the sensor and the earth's surface. SAR satellites travel from the north pole towards the south pole (descending orbit) or the south pole towards the north pole (ascending orbit). The same area is revisited along the two orbits.

The InSAR technique uses two or more SAR images of the same area to create interferograms representing ground deformation during the time interval between the image acquisitions. Only one dimension is measured with InSAR, along the satellite's line-of-sight (LOS), defined as the straight line between a SAR sensor and the ground surface.

Apart from ground deformation, an interferogram includes contributions from a variety of factors, such as the different viewing geometries of the parent images, topography, and tropospheric noise. The contributions from these factors can be minimized during data processing.

One of the initial stages of InSAR data processing is aligning one or more slave images with the master image. The distance between two acquisition spots perpendicular to the satellite viewing direction is known as the perpendicular baseline. Images can be selected with the desired perpendicular baseline and timespan to minimize image alignment problems.

Phase unwrapping is one of the most critical stages of InSAR data processing, which is needed to obtain the absolute phase change in the interferogram.

Coherence gives a quantitative measure of the amount of noise in the interferogram. Images with much noise are said to lack coherence or be decorrelated. Troposphere noise problems can be addressed using tropospheric delay map products. Another approach to minimize tropospheric noise is to form a time series of deformation from a stack of images, which averages out the noise.

2.2.1 GMTSAR

Data from C-band synthetic aperture radar (SAR) from Sentinel 1-A satellite were used to analyze crustal deformation at Fogo volcano from May 2017 to June 2019. Single Look Complex (SLC) images were used, including 63 images from ascending track 104 and 64 from descending track 111 (Figure 2.8). In addition, precise orbital information from the Alaska Satellite Facility was used and the 1-arc-second Shuttle Radar Topography Mission digital elevation model.

The InSAR data of São Miguel Island was analyzed with the GMTSAR software (Sandwell et al., 2011). A coherence-based small baseline subset time-series technique method (SBAS) was used with atmospheric corrections using common-point stacking to calculate InSAR time series (Xu et al., 2017).

It is known that C-band data from InSAR can be strongly decorrelated by several factors such as high vegetation, land use, and bad meteorologic conditions (Morishita & Hanssen, 2014; Wei & Sandwell, 2010). The image from 17 June 2018, in the middle of the observation period, was used as the master image to minimize the perpendicular baselines between interferometric pairs. Interferograms with a 50-day temporal threshold and a 100-meter perpendicular baseline threshold were used. The short temporal threshold and perpendicular baseline were set to mitigate the decorrelation effects. In addition, a 0.15 coherence threshold was set to mask data from areas with more decorrelation (Xu et al., 2017).

Higher coherence is found in urban areas near the coastline (Figure 2.8B). Relatively high coherence is also found in remote areas with high altitudes in Sete Cidade, Fogo and Povoação volcanoes, in areas where vegetation height is lower (Elias et al., 2016). The

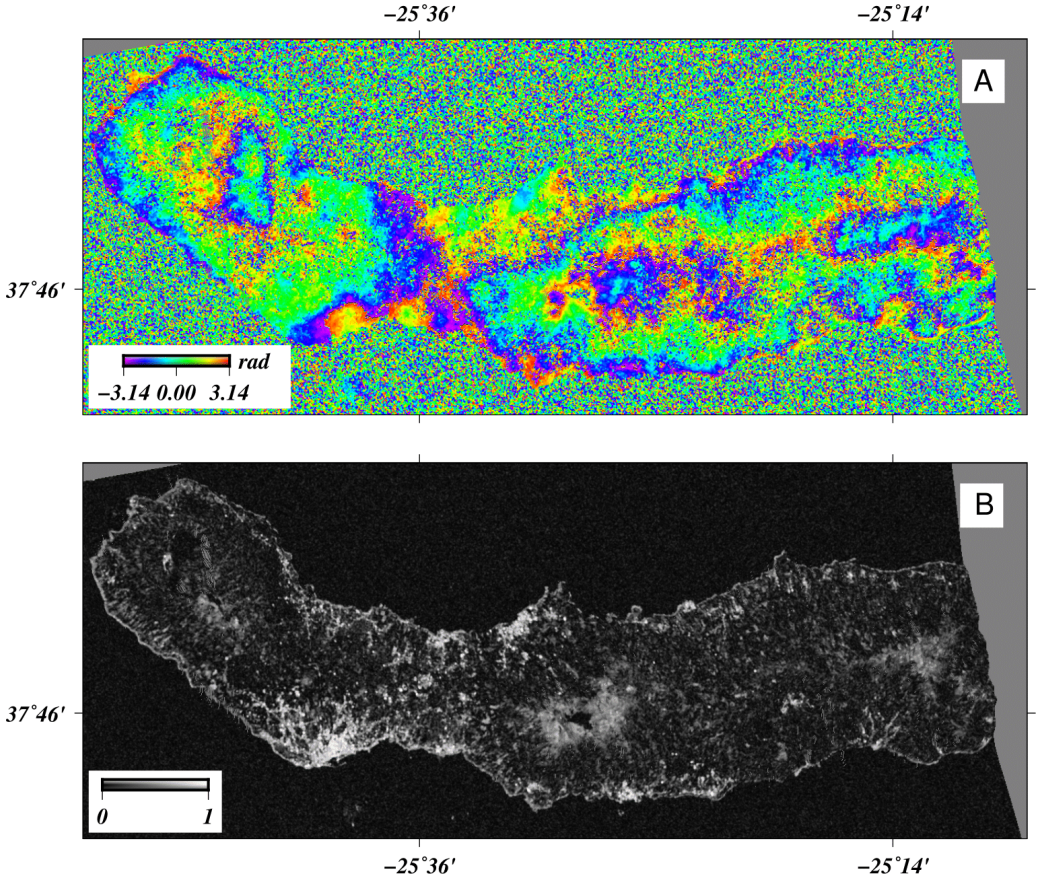

Figure 2.8: A) Interferogram generated from GMTSAR by adding 61 interferograms from ascending track images from May 2017 to June 2019 following the selection of interferometric pairs with a 100-meter perpendicular baseline threshold and 50-day temporal threshold. B) Average coherence of the interferogram generated.

lower density of vegetation facilitates the SAR waves to penetrate and backscatter from the surface. In particular, Água de Pau volcano contains an extensive natural reserve area with low vegetation surrounding the caldera. However, large areas of the island, from low to mid altitudes, are woodlands and pastures, with lower correlation values and higher noise signals.

2.2.2 LICSAR

In order to extract information on crustal deformation related to the 19-20 March 2022 activity in São Jorge Island, processed interferograms from Sentinel-1A mission were used. The original processing was performed using the standard LiCSAR software (Lazecký et al., 2020). Eight interferograms were generated in temporally shortest connections between acquisitions. The phase delay measurements were significantly affected by troposphere signals and not entirely corrected by modeling with Generic Atmospheric Correction Online Service (GACOS) products (Yu et al., 2018). Especially in the ascending satellite pass (evening acquisitions), it was observed that the magnitude of the tropospheric signal is comparable to the signal due to deformation.

To further decrease noise, InSAR time series were calculated from the unwrapped GACOS-corrected interferograms from April 2019 to August 2022 in two datasets from ascending and descending satellite passes, respectively. The time series were calculated by weighted least-squares inversion as implemented in the LiCSBAS (Morishita et al., 2020), using coherence measure to calculate weights. The time series reflects the positions in the LOS direction, with respect to the median values of coherent pixels around 38.607°N, 27.979°W, and temporally with respect to the date of the event. LOS velocities were calculated by a least squares inversion of the time series for the periods before and after the 19-20 March 2022 activity, and the event-related deformation offset was estimated.

The estimated offset in the LOS direction was projected into vertical (plus N-S horizontal component) and E-W horizontal components by a decomposition operation (Wright et al., 2004).

The color fringes from the 36-day interferogram between 13 February 2022 and 21 March 2022 (Figure 2.9) depict the amount of surface deformation. The scale represented by the fringe is about 3 cm (half of Sentinel 1-A central wavelength). In this interferogram, the spectrum of colors indicate a decrease in the LOS between the the satellite and the surface in the north and south flanks of the island consistent with inflation in the surface. The existence of at least two fringes indicates LOS displacement of about 6 cm.

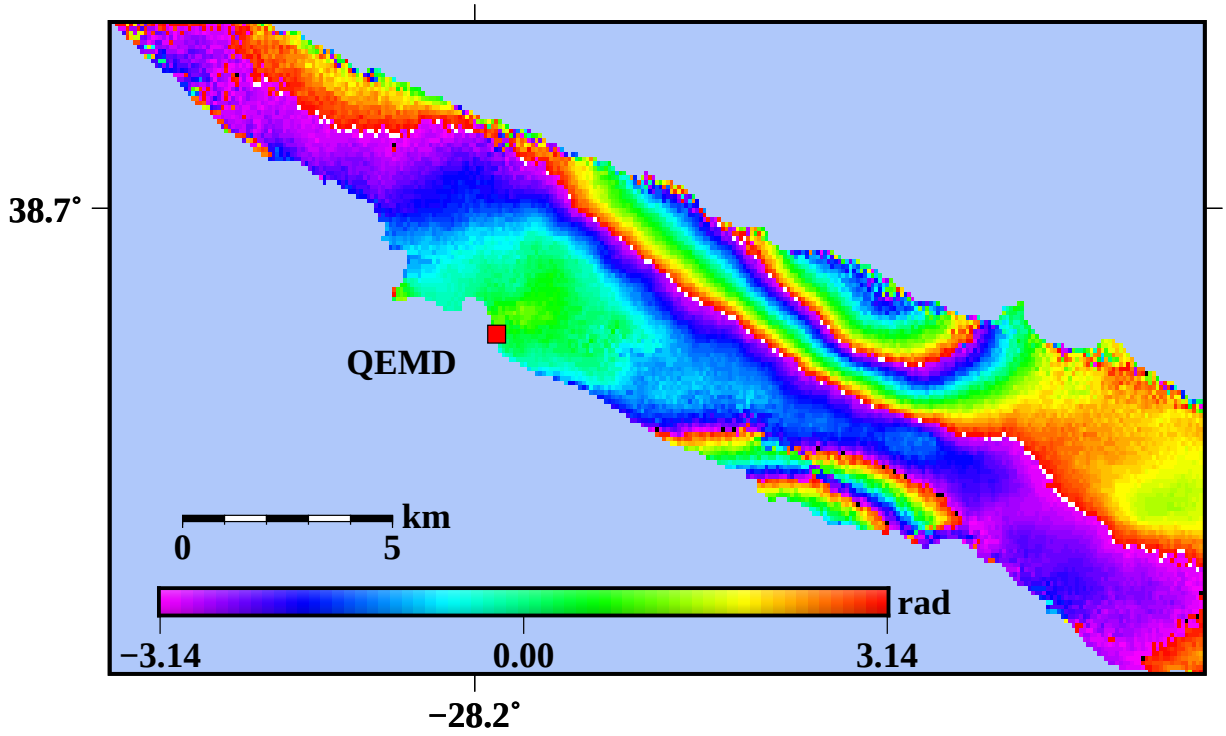

Figure 2.9: 36-day interferogram from ascending track 257 between 13 February 2022 and 21 March 2022.

2.3 Modeling

2.3.1 Eurasian-Nubian Plate Spreading Modeling

Previous studies of geodetic measurements across oblique spreading plate boundaries such as the Reykjanes Peninsula, southwest Iceland (Árnadóttir et al., 2006; Keiding et al., 2008) have used analytical models of opening and shearing dislocation sources to fit observed horizontal velocity fields. Following this approach, dMODELS software (Battaglia et al., 2013) was used for the inversion of the available GNSS data from the Azores GNSS network (D'Araújo et al., 2022). The Eurasian-Nubian plate boundary was approximated to segments with infinitely long-buried vertical rectangular dislocations embedded within uniform elastic half-space (Y. Okada, 1985). The modeling was performed for the Central Group and São Miguel islands in separate runs using different dislocations. The dislocations are assumed to have opening and right-lateral slip displacements. The dislocations have a locking depth, considered to represent the depth of the brittle-ductile boundary in the crust. The brittle crust is locked while the ductile part below opens and slips freely.

An inversion of the data was performed to estimate the best fit values of the locking depth, opening and right-lateral slip by determining the minimum value of the chi-square statistic between observed velocities of the continuous GNSS sites and model predictions.

2.3.2 Fogo Volcano Deformation Modeling

Numerous geodetic studies on active volcanoes have used analytical inverse models to fit observed velocity fields (e.g. DeGrandpre et al., 2017; Lechner et al., 2019; Mattioli et al., 2010; Papoutsis et al., 2013; Rodríguez-Molina et al., 2021). Following this approach, GBIS software (Bagnardi & Hooper, 2018) based on a Bayesian method was used for the inversion of the available GNSS data sets (D'Araújo et al., 2022), allowing the characterization of posterior probability density functions of source parameters, formulated by taking into account uncertainties in the data. The data from the main periods of deformation was modeled, namely the 2004-2006, 2011-2013, and 2018-2019 inflation periods and the 2013-2016 deflation period.

Modeling was performed to evaluate the hypothesis that deformation during each period can be explained by a single source embedded in an isotropic elastic half-space. Three different sources were used, namely point-pressure (Mogi, 1958), prolate spheroid (X.-M. Yang, Davis, & Dieterich, 1988), and penny-shaped (Fialko et al., 2001) sources. For each main deformation period, the inversion was done using the three source types, and best-fit parameters were estimated. The Poisson's ratio was set to 0.3 and the shear modulus to 5.4 GPa during the inversion using estimated average values obtained from laboratory studies of volcanic rock samples from multiple areas (Heap et al., 2020). The software was set to search randomly for the central horizontal location of the sources in a squared area with a 5 km length centered at a point between the Fogo caldera lake and the ARE1 station to the east (see Table A2 in Appendix A). This area is the approximate location of an inferred magma chamber. The software was also set to search randomly for the source depth in the

1-20 km range, following crustal thickness estimates in the Azores.

Three different models for each deformation period were compared by performing statistical analysis of the modeling results (e.g., Battaglia & Hill, 2009; DeGrandpre et al., 2017; Di Vito et al., 2016). The chi-square statistic was computed as:

$$\chi^2 = \sum_{n=1}^{N} \frac{(O_i - P_i)^2}{P_i} \tag{2}$$

The chi-square statistic was defined as the weighted sum of squared deviations between observed (O_i) and predicted (P_i) full displacement vectors from modeling. For each period, it was used data from the total number of available stations N located inside the GNSS network. The misfit between observed and predicted velocities is given by the chi-square per degree of freedom defined as:

$$\chi^2_\nu = \frac{\chi^2}{\nu} \tag{3}$$

The degrees of freedom (ν) were defined as the number of data points minus the number of parameters to be estimated. χ^2_ν values much greater than one indicate poor data fitting, while values closer to one indicate better fitting. The lowest chi-square values per degree of freedom represent the best fit between observed and predicted values. For each period of deformation, the point-pressure source model, which has the fewest parameters, was used as the null hypothesis.

In order to assess if the more complex models are statistically significant, F-tests were computed between the models and the point-pressure source model. The F statistic was calculated as follows:

$$F_{(Np_X - Np_M),\nu_X} = \frac{(\chi^2_{\nu M}\nu_M - \chi^2_{\nu X}\nu_X)/(Np_X - Np_M)}{\chi^2_{\nu X}} \quad (4)$$

In the previous expression, M is the Mogi model, X is the more complex model to be compared, ν the degrees of freedom, and Np is the number of source parameters. If the F statistic is greater than the critical value of the F-distribution (F_{crit}) for some desired false-rejection probability, then the smaller χ^2_ν obtained with a more complex model is statistically significant. The F-distribution was tested for false-rejection probabilities of 95% and 99%.

2.3.3 São Jorge Island Deformation Modeling

Similarly to the Fogo volcano modeling, the inversion of the data set from São Jorge Island was performed using GBIS software using source models embedded in an isotropic elastic half-space. The Poisson's ratio was set to 0.3 and the shear modulus to 5.4 GPa during the inversion using estimated average values obtained from laboratory studies of volcanic rock samples from multiple areas (Heap et al., 2020).

A first attempt was made for the inversion of the 19-20 March deformation using a single opening rectangular dislocation source (Y. Okada, 1985). The software was set to search randomly for the horizontal location of the source across the island and the depth in the range of 1-20 km. Another attempt was performed using a single opening rectangular dislocation source constrained with the location of the seismic events in the 19-20 March period.

More complex modeling of distributed dyke opening was performed using a two-segment dyke, divided up into 1.5x1.5 km rectangular patches with opening motion (Y. Okada, 1992). The locations of seismic events were used to constrain the orientation of the segments. The eastern segment is shallower, extending between 3 and 7 km depth, with an N115°E

orientation. The western segment is deeper, extending between 7 and 13 km depth, with an N105°E orientation.

For the post-March 19 period, the GNSS data was modeled using a single opening rectangular dislocation source (Y. Okada, 1985). The size and location of the dislocation were constrained by the western segment of the two-segmented set of multiple patches modeled previously.

2.4 Seismic Data

Geodetic data are compared to observed seismic activity by CIVISA (Centro de Informação e Vigilância Sismovulcânica dos Açores). The CIVISA seismic network in the Azores (CIVISA, 2022) comprises about 50 stations of which 18 are located at São Miguel Island and 7 are located at São Jorge Island. In the CIVISA database, there are two types of magnitudes: duration magnitudes (M_D) and local magnitudes (M_L) (R. Silva et al., 2015). Data from 2000 to 2022 was used in this study. The most representative magnitude type for this study period is the M_D magnitude. The recorded seismic events are mainly volcano-tectonic (VT), but occasionally events with volcanic characteristics (VL) occur. The VT events have clear P and S phases, while the VL events sometimes do not have a clear P phase onset and often lack a clear S phase. Compared with the VT events, the VL events have lower frequencies of around 2-3 Hz. From the total recorded events for the study period, we select the ones recorded at least in four seismic stations, with computed duration magnitudes (M_D) of at least 2.0 and a maximum error of 0.3 s. The error corresponds to the propagation time residual of the seismic phase given by the difference between the observed arrival time of the signal and the predicted arrival time estimated from a local velocity model. About 10% of the total recorded events correspond to the selection used.

3 Eurasian-Nubian Plate Spreading

This chapter presents results from inter-island spreading in the Azores, namely in the Central Group, and intra-island spreading on São Miguel Island using data from continuous GNSS stations (see Figure 2.1) from the 2000-2016 period (D'Araújo et al., 2022) and results from intra-island spreading on São Miguel Island from a dense array of episodic GNSS stations from the 2004-2016 period (see Figure 2.4). Velocities of the GNSS stations in the ITFR2014 reference frame were estimated initially and detrended using plate motion estimates (see Methods). Modeling results and discussion of results from Eurasian-Nubian plate spreading are also presented in this chapter.

The regional deformation field was analyzed from the estimated velocities of the more stable continuous GNSS stations. The data from the stations located around Fogo volcano affected by transient deformation were excluded from the analysis. Most previous ground deformation studies conducted in the Azores have relied on sparse GNSS data, mostly from annual campaign surveys (Fernandes et al., 2006; Marques et al., 2013; Mendes et al., 2013; Miranda et al., 2012; Trota et al., 2006). Besides lower temporal resolution, the data from campaign observations have several limitations, such as high susceptibility to severe atmospheric conditions, multipath error, and bad satellite geometry, resulting in lower precision of the estimated velocities. The number of stations used in this study is small compared with some previous GNSS campaign surveys. Still, the higher temporal resolution of the continuous GNSS data allows for estimating velocities with higher precision. Therefore, continuous GNSS data analyses allow discriminating better between long-term displacements, such as plate motion, and local short-term displacements, such as volcano deformation.

3.1 Azores Inter-Island Spreading

3.1.1 ITFR2014 Velocities

The velocities in the ITFR2014 reference frame show differential motion between the continuous GNSS stations (Table 3.1). The FLRS station on the North American plate is moving at a rate of 22.4 mm yr^{-1} in the direction of N23°W. In contrast, all other stations located east of the Mid-Atlantic Ridge are moving at a rate of $20.6^{+1.9}_{-1.5}$ mm yr^{-1} to N(40^{+3}_{-3})°E in the same reference frame.

Table 3.1: Velocities of the more stable continuous GNSS stations in the ITRF2014 reference frame, with 1σ Uncertainties, in East, North, and Up components, and correlation factor between horizontal components. Reproduced from D'Araújo et al. (2022).

		Velocity (mm yr^{-1})			
Station	Date Interval	E	N	U	Corr
AZGR	2008/07 - 2016/07	15.5 ± 0.2	16.3 ± 0.2	-2.7 ± 0.6	-0.2
FLRS	2009/01 - 2017/01	-8.6 ± 0.6	20.7 ± 0.3	-2.7 ± 1.1	-0.2
FRNS	2008/07 - 2016/07	14.7 ± 0.3	16.0 ± 0.4	-1.4 ± 0.9	0.0
HORT	2013/03 - 2016/03	12.2 ± 0.6	15.1 ± 0.6	-3.5 ± 1.5	-0.2
*HTN*1	2005/05 - 2012/05	14.5 ± 0.3	15.5 ± 0.5	-1.8 ± 1.1	0.0
*NOV*1	2003/02 - 2016/02	13.5 ± 0.2	14.8 ± 0.2	-2.9 ± 0.4	0.1
PDEL	2000/05 - 2016/05	12.3 ± 0.1	16.3 ± 0.1	-1.5 ± 0.4	-0.1
PIED	2009/01 - 2017/01	12.2 ± 0.3	14.7 ± 0.3	-2.2 ± 0.7	-0.1
PTRP	2010/05 - 2016/05	12.3 ± 0.4	15.2 ± 0.5	-2.9 ± 1.3	0.0
*QBN*1	2003/07 - 2016/07	14.6 ± 0.2	17.0 ± 0.2	-1.3 ± 0.4	0.2
QEMD	2012/11 - 2016/11	13.0 ± 0.5	15.5 ± 0.5	-1.7 ± 1.3	0.2
SRPC	2003/02 - 2016/02	14.1 ± 0.1	16.5 ± 0.2	-3.7 ± 0.5	0.1
TERC	2008/09 - 2016/09	13.1 ± 0.3	16.1 ± 0.3	-3.9 ± 0.7	-0.1

3.1.2 Detrended Velocities

Various plate motion models provide estimates of plate spreading direction and full plate velocity across the Azores. The ITRF2014 plate motion model (Altamimi et al., 2017) was used, which has a Eurasian-Nubian full plate velocity close to the GEODVEL2010 model (Argus et al., 2010) (see Table A8 in Appendix A). The horizontal velocity of the FLRS station was compared with predicted stable North American displacement, and the velocities of the stations located in the Central Group and São Miguel Island were compared with both predicted stable Eurasian and Nubian velocities.

The detrended time series of the continuous GNSS stations from the Central Group and São Miguel islands are shown in Figures 3.1 and 3.2, respectively, together with seismicity results. There are differences in the time span of the time series of the continuous GNSS stations. The station with the longest time series is PDEL spanning almost 17 years, whereas the station with the shortest time series is HORT, with nearly four years. There are some gaps in the time series, mostly at remote stations operating without data transmission devices. The time series from PDEL, HTN1, FRNS, and QBN1 stations at São Miguel Island and the stations at the other islands show stable displacements. In contrast, the time series of RIB1, RCHA, BVF1, VFDC, and PCNG stations located at Fogo volcano, in São Miguel Island, show significant variations in the rate of the displacement, as a result of unrest episodes at the volcano during the study period.

The velocity field of the continuous GNSS stations are shown Figure 3.3. The velocity of the FLRS station is relative to predicted stable North American plate motion, while all others are relative to predicted stable Eurasian plate motion.

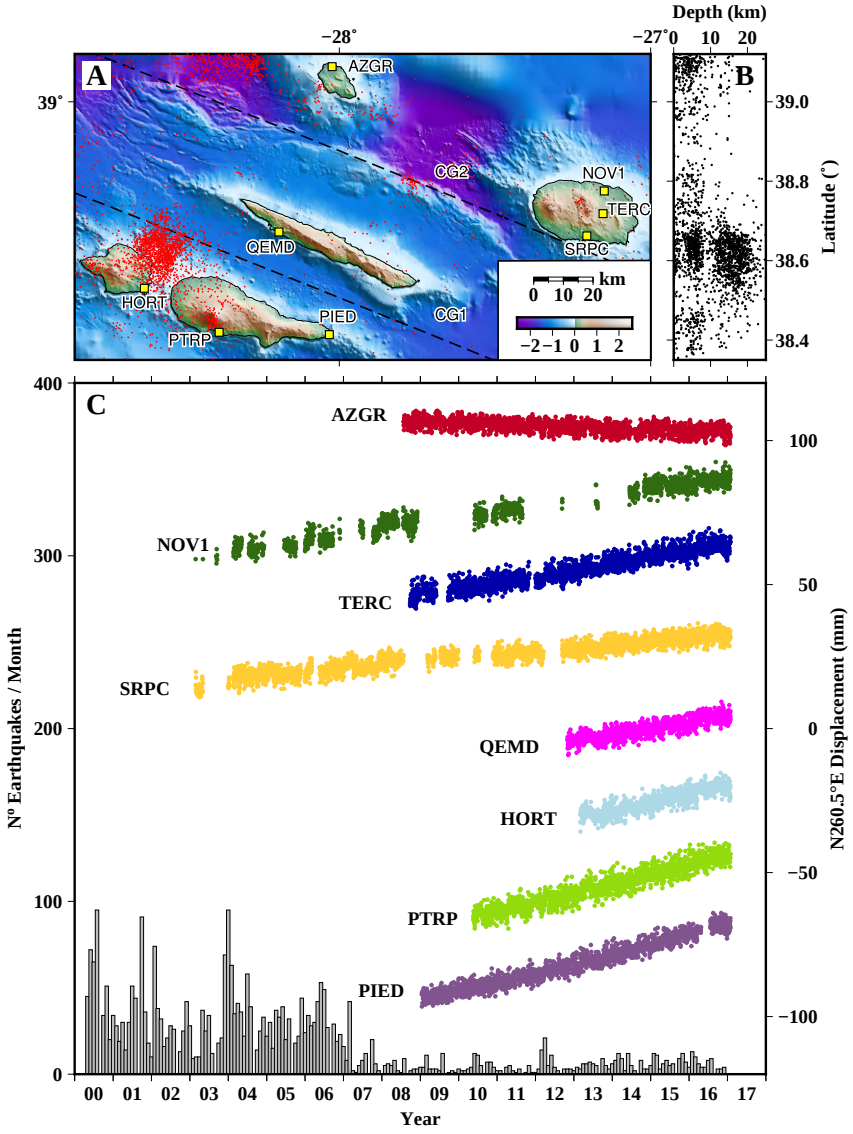

Figure 3.1: A - Location of the continuous GNSS stations AZGR, NOV1, TERC, SRPC, QEMD, HORT, PTRP, and PIED located in the Central Group. Red circles are recorded earthquakes ($M_D \geq 2$). Dashed lines are the surface projection of the vertical dislocation of the CG1 and CG2 models for the area. B - Time series of horizontal displacement at the continuous GNSS stations movement relative to predicted Eurasian motion, in the direction of predicted Eurasian motion (N260.5°E). The times series are shifted from top to bottom to display the continuous GNSS stations movement from the north (AZGR) to the south (PIED). The vertical gray bars are the monthly number of earthquakes in the area ($M_D \geq 2$). Reproduced from D'Araújo et al. (2022).

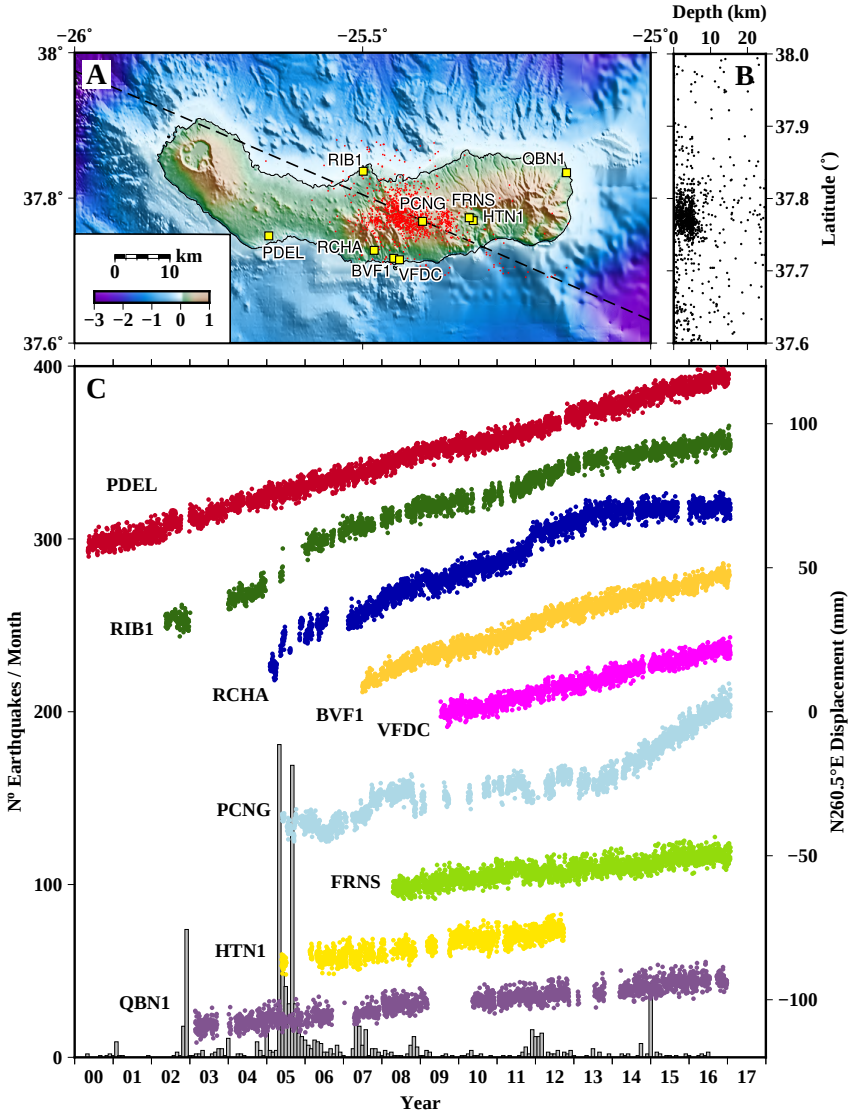

Figure 3.2: A - Location of the continuous GNSS stations PDEL, RIB1, RCHA, BVF1, VFDC, PCNG, FRNS, HTN1, and QBN1 located in São Miguel Island. Red circles are recorded earthquakes ($M_D \geq 2$), concentrated between Fogo and Furnas volcanoes. Dashed line is the surface projection of the vertical dislocation of the SM model for the area. B - Time series of horizontal displacement at the continuous GNSS stations movement relative to predicted Eurasian motion, in the direction of predicted Eurasian motion (N260.5°E). The times series are shifted from top to bottom to display the continuous GNSS stations movement from the west (PDEL) to the east (QBN1). The vertical gray bars are the monthly number of earthquakes in the area ($M_D \geq 2$). Reproduced from D'Araújo et al. (2022).

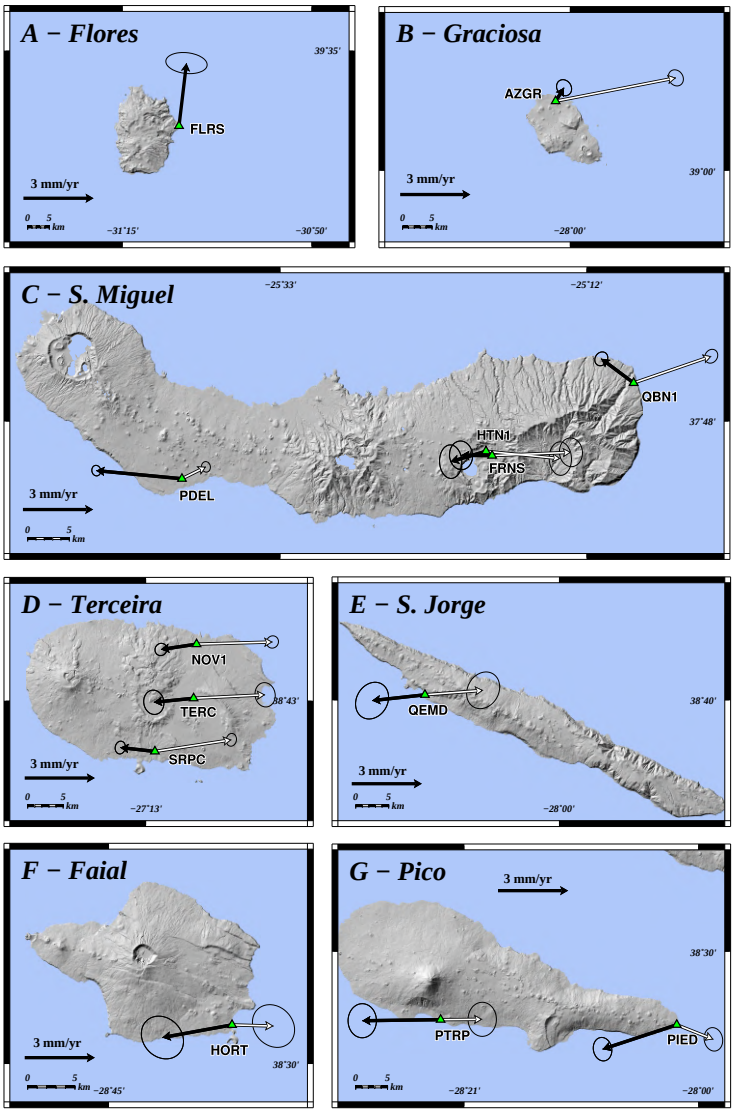

Figure 3.3: Horizontal velocities of continuous GNSS stations located on Flores (A), Graciosa (B), São Miguel (C), Terceira (D), São Jorge (E), Faial (F) and Pico (G). In figure A, the black arrow represents the velocity from Table 3.1 relative to predicted North American motion. In figures from B to G, the black and white arrows represent the velocities from Table 3.1 relative to predicted Eurasian and Nubian motions, respectively. The ellipses represent the 1σ confidence level, and the green triangles are the continuous GNSS stations. Reproduced from D'Araújo et al. (2022).

The results show that Flores Island has a very distinct motion compared with the other islands, consistent with its location on the North American plate. The station on Flores Island (FLRS) (Figure 3.3A) moves with a velocity close to predicted North American velocity. The lack of significant recorded seismic activity in the area indicates that the island is relatively stable. However, the deviation of $\sim$3 mm yr^{-1} between estimated and predicted motion suggests that Flores island may be subject to local deformation. This deviation may also relate to the lack of data from this area on the eastern edge of the North American plate used to compute global plate motion models.

Graciosa Island shows a displacement close to predicted Eurasian motion, as shown by the station located on the island (AZGR) (Figure 3.3B). The maximum estimated Eurasian-Nubian motion is found between this station and the PIED station located in the eastern part of Pico Island. The AZGR station is moving at a rate of 3.7 $\pm$ 0.5 mm yr^{-1} to N(64 $\pm$ 9)°E relative to the PIED station, which is $\sim$80% of predicted spreading in the area, indicating that the inter-plate deformation zone is broader than the area between the two stations. Despite the displacement close to Eurasian predicted motion, the recurrent seismicity west of Graciosa indicates that the island is located in an active deformation area.

São Miguel, Terceira, São Jorge, Faial, and Pico islands have displacements between predicted Eurasian and Nubian motions. The stations located in the eastern part of São Miguel Island (HTN1, FRNS, and QBN1) (Figure 3.3C) and Terceira Island (NOV1, TERC, and SRPC) (Figure 3.3D) are moving close to predicted Eurasian motion, but at a lower rate compared to station AZGR located on Graciosa Island. The small deviation of the QBN1 velocity indicates that the eastern part of São Miguel Island is not fully within predicted stable Eurasian plate and is subject to some inter-plate deformation.

On the other hand, the PDEL station on the western part of São Miguel Island and the stations located on São Jorge (Figure 3.3E), Faial (Figure 3.3F) and Pico (Figure 3.3G) islands have higher displacements away from the Eurasian predicted motion and displacements closer to the Nubian motion. Spreading between the western and eastern parts of São Miguel Island is revealed from the differential motion between PDEL station and stations HTN1, FRNS, and QBN1, with a maximum displacement of 2.4 ± 0.3 mm yr^{-1} in the direction of N(73 ± 8)°E and 0.17 μstrain. The station QEMD on São Jorge Island is moving closer to the Eurasian motion than the stations on Faial and Pico islands. The station PIED in the eastern part of Pico Island has the fastest displacement away from Eurasian motion and closer to Nubian motion. The other stations, HORT on Faial and PTRP on Pico, move with intermediate displacements relative to QEMD and PIED stations. The similar velocities found at HORT and PTRP stations located on Faial and Pico islands, respectively, suggest that the eastern part of Faial Island and the western part of Pico Island are moving as a block as indicated from previous campaign GNSS surveys (Marques et al., 2013). HORT and PTRP stations move about 1 mm yr^{-1} away from QEMD station located on São Jorge Island. The small differential motion observed between the stations of São Jorge and Faial/Pico islands constitute evidence of spreading occurring between the islands.

Compared with previous GNSS studies in the Azores, the values of the vertical velocities in this study are well constrained, with uncertainties ranging from sub-millimeter level to a few millimeters. The results from the more stable continuous GNSS stations show that the Azores Islands are subsiding at an average rate of 2.7 ± 0.7 mm yr^{-1} during the study period (see Table 3.1).

3.1.3 Modeling Results

Before the inversion, the velocity field was corrected from a local subsidence in Terceira Island by estimating the deformation generated by a spherical source of pressure decrease within uniform elastic half-space (Mogi, 1958) located between Guilherme Moniz caldera and Pico Alto volcano summit at 5 km depth, with a volume change of -2.5×10^5 m^3 yr^{-1}. During the inversion, a locking depth was searched in the range of 1-20 km, following estimates of crustal thickness in the Azores. The opening and slip motion variables were constrained between zero (no displacement) and the maximum predicted Eurasian-Nubian relative plate motion of 4.8 mm yr^{-1} (see Table A8 in Appendix A).

Geologic, geodetic and seismic data were used to constrain the location and direction of the dislocations. Neotectonic studies show that the dominant morpho-tectonic structures at São Miguel Island are NW-SE to WNW-ESE trending faults (Carmo et al., 2015). The location of the boundary in the central part of São Miguel Island, between Fogo and Furnas volcanoes, is constrained from previous geodetic and seismic studies (Jónsson et al., 1999; J. Okada et al., 2015; R. Silva et al., 2012; Trota et al., 2006). A dislocation model was used with the N112.5°E direction (WNW-ESE), crossing the seismically active Congro fissure zone, where the main morpho-tectonic structures have a WNW-ESE direction.

There was more uncertainty about the location of the spreading axis in the Central Group. In this area, the dislocation model was tested with two different locations: between Faial-Pico islands and São Jorge Island (CG1) and between Graciosa-Terceira islands and São Jorge Island (CG2). The dislocation orientation in the Central Group was defined as N112.5°E following the main orientation of the shape of the islands and surrounding bathymetric

structures (Lourenço et al., 1998).

The model results (Table 3.2 and Figure 3.4) for São Miguel Island predicts a deep motion of 2.3 mm yr^{-1} in N82.3°E direction, with 1.2 mm yr^{-1} opening motion, and 2.0 mm yr^{-1} right-lateral slip motion. The locking depth is about 2 km, much shallower than the crustal thickness in the Azores. It may be underestimated because of the relatively low number of continuous GNSS stations from São Miguel Island used in the modeling. For the Central Group, the model CG1 is favored over CG2, despite the slightly higher chi-square value. The fit quality in the stations on Terceira Island is similar in the CG1 and CG2 models. On the other hand, the quality of fit in the stations located on São Jorge, Faial, and Pico islands is better in the CG1 model. In comparison, the fit quality in the AZGR station located on Graciosa Island is better in the CG2 model. The CG1 model predicts a deep motion of 2.5 mm yr^{-1} at N88.7°E direction, with 1.0 mm yr^{-1} opening motion, and 2.3 mm yr^{-1} right-lateral slip motion. The locking depth is at least 20 km, agreeing well with crustal thickness estimates. The velocities obtained from modeling the data of São Miguel Island and the Central Group account for ∼50% of predicted Eurasian-Nubian relative plate motion.

Table 3.2: Elastic Half-space Dislocation Model Parameter Estimates for São Miguel Island (SM) and Central Group (CG)

			Velocity (mm yr^{-1})				
Model	Stations	Depth	Open	Slip	Deep Motion[a]	Azimuth[b] (N°E)	$\chi_\nu{}^2$
SM	4	2	1.2	2.0	2.3	82.3	1.3
CG1	8	20	1.0	2.3	2.5	88.7	4.5
CG2	8	20	1.5	2.8	3.1	85.0	4.1

[a]Magnitude of the vector sum of the right-lateral slip and opening.

[b]Direction of the deep motion.

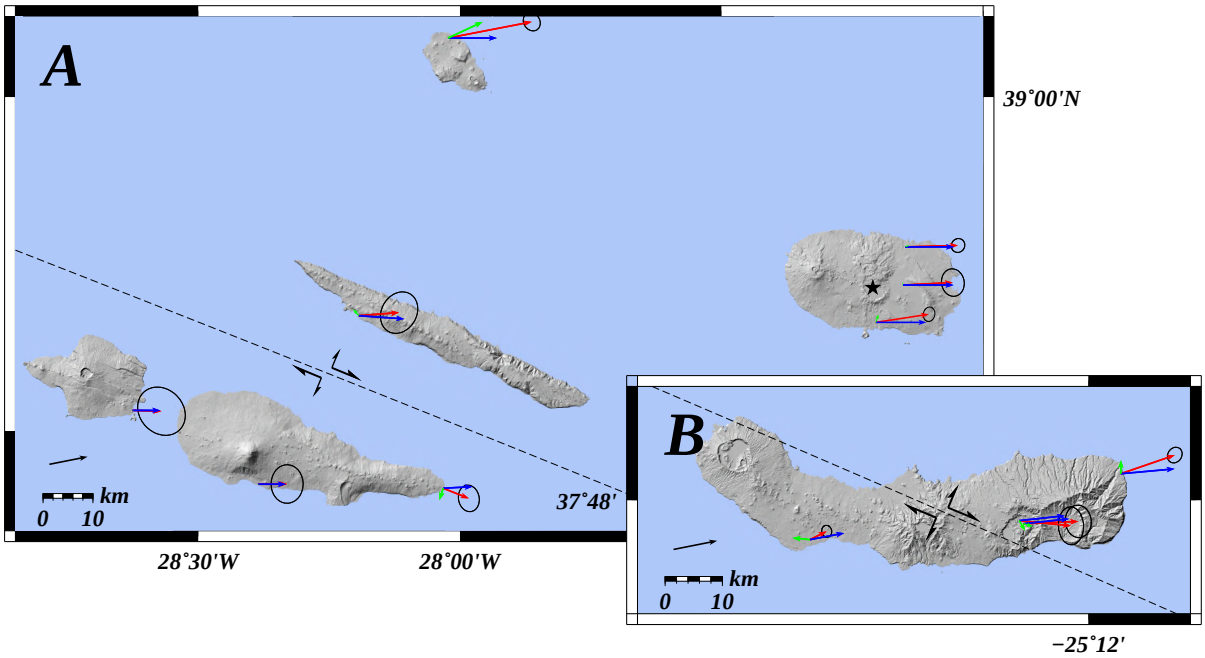

Figure 3.4: Results of kinematic plate boundary modeling of the horizontal velocities for Central Group islands (A) and São Miguel Island (B). The colored velocity arrows show observed corrected from Mogi source (red, 2σ confidence ellipses), predicted from data inversion using Okada dislocations (blue) and residuals (green). The black velocity arrows show predicted deep motion displacements, and the half-arrows are predicted opening and slip displacements from the dislocations. The dislocations CG1 (A) and SM (B) are shown with dashed black lines. Mogi source is shown with a black star (A). Reproduced from D'Araújo et al. (2022).

3.2 São Miguel Intra-Island Spreading

The time series of episodic GNSS stations of São Miguel Island in the ITRF2014 reference frame for the 2004-2016 period, excluding the stations located in the central area of the island from Fogo volcano to the Congro volcanic system, show stable motion with no episodic transient deformation. The velocities of the episodic GNSS stations in the island relative to predicted stable Eurasian plate motion show a differential motion between the stations located in the western part of the island, from Sete Cidades volcano to the Picos volcanic system and the stations located in the eastern part of the island, from Furnas volcano to the Povoação volcano (Figure 3.5). The differential motion is consistent with the spreading revealed previously from the differential motion between the continuous GNSS stations located in the eastern and western parts of the island.

The GNSS velocities were interpolated in each component using a minimum curvature spline interpolation (Sandwell, 1987) to get a better spatial overview of the deformation field (Figure 3.6). The velocity fields were interpolated with an equidistant sampling interval of 10 arc-seconds.

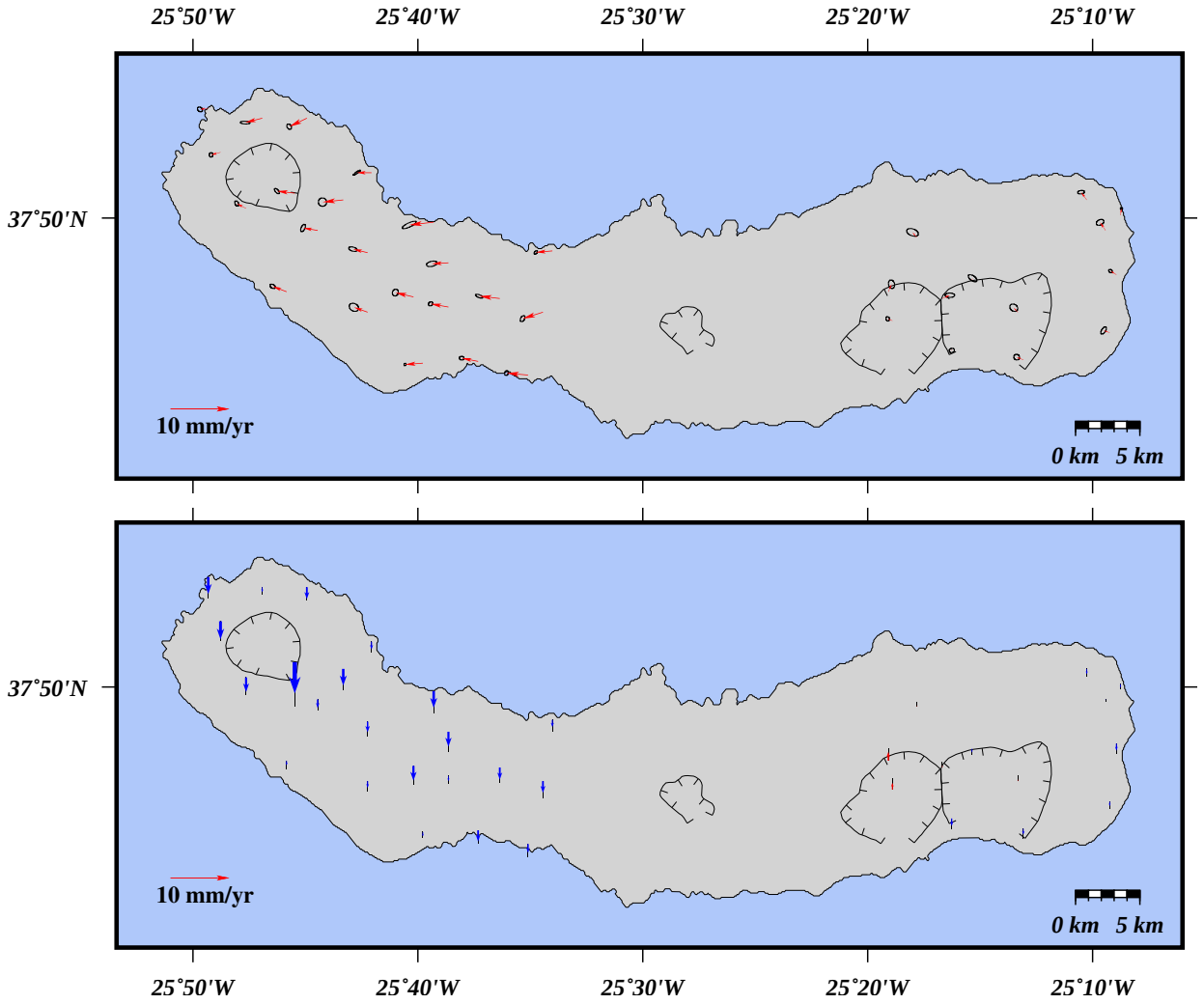

Figure 3.5: (Top) Horizontal velocities of GNSS stations in São Miguel Island relative to predicted Eurasian motion. The ellipses represent the 1σ confidence level. (Bottom) Vertical velocities of GNSS stations from São Miguel Island. GNSS stations from the central area of São Miguel Island with transient volcano deformation are excluded.

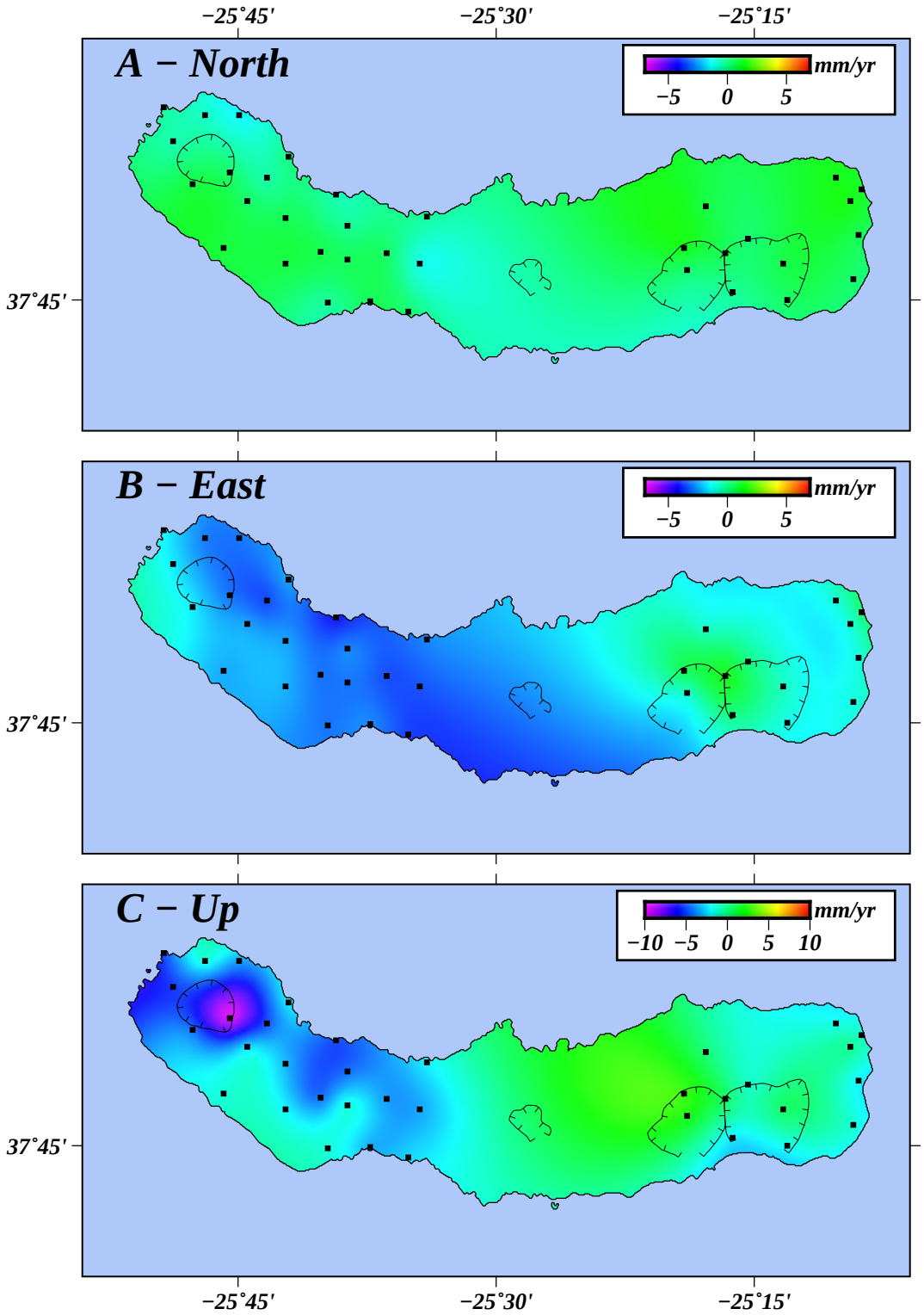

Figure 3.6: Velocity field interpolated in the north (A), east (B), and up (C) components. Black rectangles are the GNSS stations used in the interpolation.

The small horizontal velocity arrows of the GNSS stations located on the eastern part of São Miguel Island show that this area moves close to predicted Eurasian plate motion. On the other hand, the velocity arrows of the GNSS stations located on the western part of São Miguel Island have displacements to the west direction, indicating that this area moves away from predicted Eurasian plate motion and closer to predicted Nubian plate motion. The interpolated velocity field shows that the spreading occurs almost entirely in the E-W direction with nearly no displacement in the N-S component. The average differential velocity between the eastern and western stations is 2.2 ± 0.5 mm yr^{-1} in the N(80.5)°E direction (Figure 3.7).

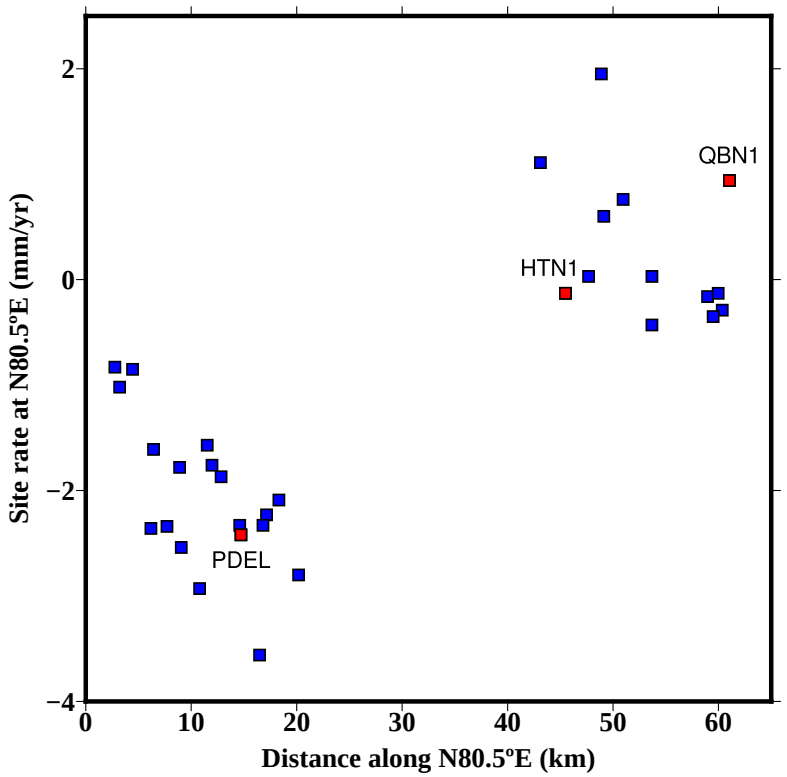

Figure 3.7: Horizontal velocities of the GNSS stations of São Miguel Island in the direction N80.5°E, relative to predicted Eurasian motion. Squares are the GNSS stations. Red squares are the continuous GNSS stations PDEL, HTN1, and QBN1.

The small vertical velocity arrows of the GNSS stations located on the eastern part of São Miguel Island show that this area is more stable and has no inflation or deflation. On the other hand, the vertical velocity arrows of the GNSS stations located on the western part of São Miguel Island have displacements consistent with deflation, indicating that this part of the island is subsiding. The stations on the western part of the island are subsiding at an average rate of 3.5 ± 1.5 mm yr^{-1}.

Besides spreading between the western and eastern parts of the island, the interpolated velocity in the east component shows relatively higher velocities in the western flank of Sete Cidades volcano to the east direction (see Figure 3.6B). These higher velocities can be explained by the existence of a local deformation source consistent with a contraction centered in the Sete Cidades volcano. The higher deflation in the interpolated velocity in the up component indicates that Sete Cidades is subject to local subsidence.

3.3 Discussion

Observations from morpho-tectonic analysis (Lourenço et al., 1998) and previous campaign GNSS surveys in the Central Group (Fernandes et al., 2006; Marques et al., 2013) show evidence that the Eurasian-Nubian boundary in the Azores is diffuse. The observations from continuous GNSS data in the current study align with this assessment. The Eurasian-Nubian motion in the Azores appears not to change gradually across the inter-plate deformation zone. Instead, it is more focused in some areas, namely in the central area of São Miguel Island and between Faial-Pico ridge and Terceira Island. In particular, a narrow area in the central part of São Miguel Island accommodates at least half of predicted regional

spreading. The existence of active plate spreading in São Miguel Island is suggested from other studies using both campaign (Trota et al., 2006) and continuous GNSS data (J. Okada et al., 2015).

The results show spatial variations of the differential motion along the Eurasian-Nubian plate boundary in the Azores Plateau. The broader deformation zone in the Central Group islands is consistent with volcanism distributed over a wider area, while in São Miguel Island, the deformation is more focused. Seismic activity is also focused in some areas of the Eurasian-Nubian boundary, with stronger earthquakes more concentrated in rift basins between the islands and in the central area of São Miguel Island. From 2002 to 2010, the central area of São Miguel Island experienced higher seismic activity than in the previous decades, mainly as swarms with events of small magnitude (R. Silva et al., 2012).

There is evidence of low degrees of partial melting beneath the thick lithosphere caused by a mantle anomaly centered under the Central Group islands (Gente et al., 2003; Moreira et al., 1999; T. Yang et al., 2006). The existence of deep processes in the Central Group is also suggested by the large locking depth of the preferred model dislocation in the area (see Table 3.2) and the deep earthquake activity (see Figure 3.1B).

Analysis of geochemical data indicates that focused magmatism occurs along the Terceira Rift below volcanic systems (Beier et al., 2008; Haase & Beier, 2003; Storch et al., 2020). The existence of shallow processes in São Miguel Island is inferred from the shallow locking depth of the modeled dislocation for the island (see Table 3.2) and the shallow earthquake activity (see Figure 3.2B). The shallow processes may weaken the crust and cause strain localization. Strain focusing in the central area of the island may relate to the episodic intrusions at Fogo during volcano unrest.

The high temporal resolution of the continuous GNSS data allows for calculating velocities with high precision and performing an inversion of the data using simple analytical models. On the other hand, the low spatial resolution and poor distribution of GNSS stations are limitations to the modeling. There is no geodetic data from large submarine areas, and some islands have no GNSS stations or only a single station. In particular, the preference for the CG1 model for the Central Group is constrained by the higher number of GNSS stations located in Terceira, São Jorge, Faial, and Pico islands, compared with the Graciosa Island area.

The spatial variation of the crustal deformation and the seismicity distribution suggest partitioning of strain release in rift basins with tectonic earthquakes and on the islands with volcano unrest. The spreading in the Eurasian-Nubian plate boundary in the Azores follows patterns similar to other ultraslow mid-ocean ridges (Sibrant et al., 2015; Storch et al., 2020). The ultra-slow spreading axes of the Gakkel Ridge and the South Indian Ridge comprise segments showing amagmatic extension and other segments with magmatic extension (Cannat et al., 2019; Cochran, 2008).

It is inferred that some submarine areas of the Eurasian-Nubian plate boundary in the Azores are presently subject to rifting, contributing to the remaining predicted plate spreading not detected with current observations, such as the Povoação basin to the east of São Miguel Island, the Hirondelle basin between São Miguel and Terceira islands, and the area between the Mid-Atlantic Ridge, Faial and Graciosa islands.

Previous campaign GNSS surveys show evidence of continuous subsidence of Terceira Island (Marques et al., 2015; Miranda et al., 2012). The previous surveys show horizontal residual velocities compatible with a deflation in the center of the island, but no confirmation

from the vertical component was possible. The horizontal velocities of Terceira stations from this study show a deviation towards the center of the island, which agrees with a deflation source located in that area. The higher subsidence rate found in TERC station in the central part of Terceira confirms the existence of deflation in the area. The extended deformation period and modeling results suggest that the deflation can be due to the crystallization and degassing of an underlying magma body or the decompression of a hydrothermal system in the center of the island. The deflation can contribute to concentrated seismicity occurring in the center of the island.

The time series of the stations located around Fogo volcano (BVF1, RCHA, RIB1, PCNG, and VFDC), on São Miguel Island, show disturbances related to unrest activity, signaling the likely accumulation of volcanic fluids below the volcano. The deflation in Sete Cidades volcano inferred from the episodic GNSS stations from São Miguel Island is possibly due to the crystallization and degassing of an underlying magma body or the reduced pressure in a hydrothermal system below the volcano.

4 Fogo Volcano Deformation

The central part of São Miguel Island has been the stage of recurrent unrest in the last 20 years. Processes occurring in this area, relating to the Fogo volcano and the Congro fissure zone, are evaluated using GNSS, InSAR, and seismic data.

In this chapter, results from seismicity and GNSS time-series for the 2000-2016 period are initially presented. In addition, the chapter presents results from modeling and velocity fields from multiple transient deformation episodes that occurred in the 2000-2016 period (D'Araújo et al., 2022), namely the 2004-2006 inflation, 2007-2011 stable period, 2011-2013 inflation, and 2013-2016 deflation. Results of the more recent 2018-2019 inflation are also presented. The velocities of the GNSS stations (Figure 4.1) were estimated relative to the average velocity of reference stations located in the island (see Methods). A general discussion is presented in the end of the chapter.

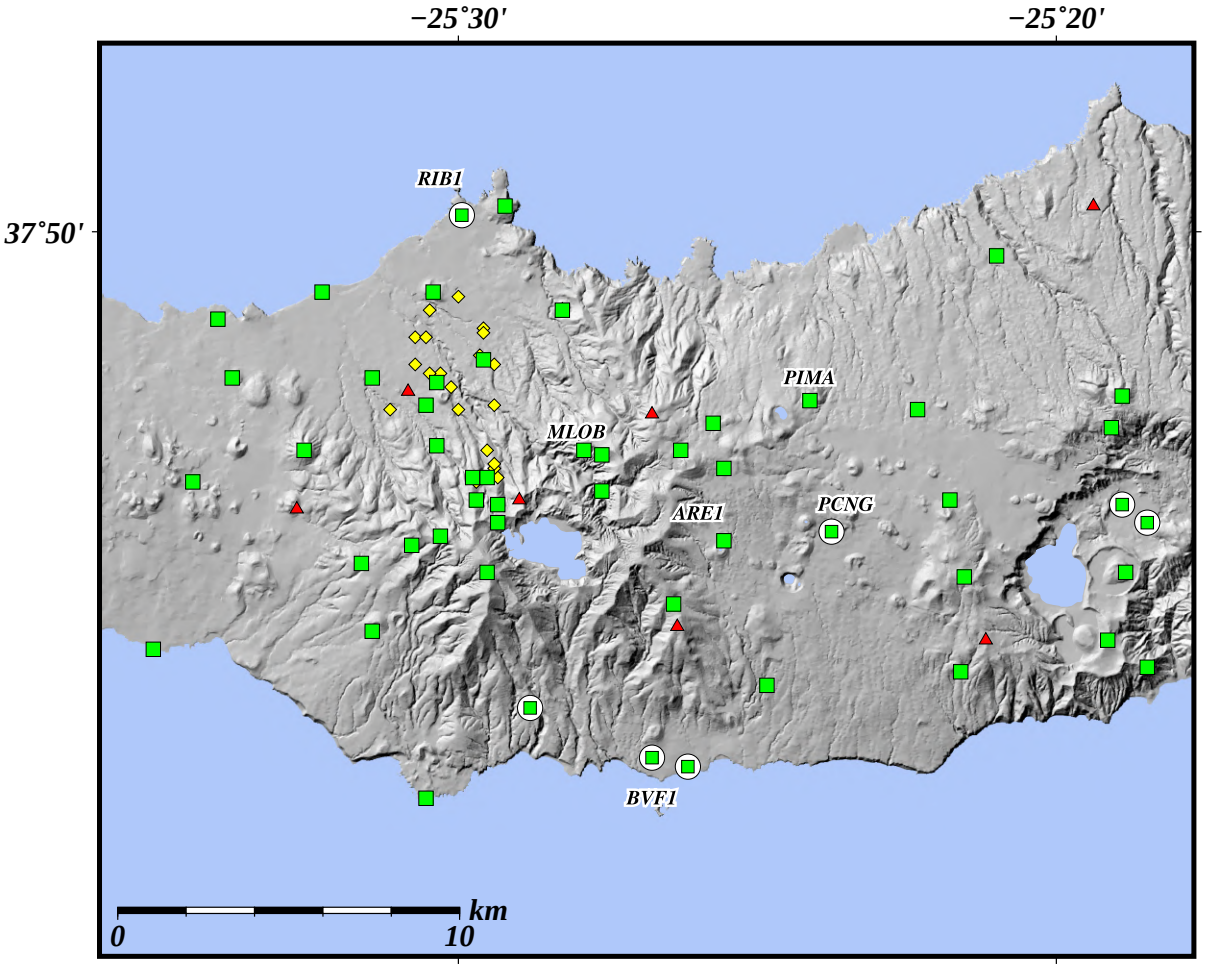

Figure 4.1: Fogo volcano GNSS network. Episodic GNSS benchmarks (green squares), continuous GNSS (green squares and white circles), seismic stations (red triangles), and geothermal wells (yellow diamonds) are shown. 4-character codes are shown for GNSS stations mentioned in text and with time series shown in Figures 2.6 and 2.7. Modified from D'Araújo et al. (2022).

4.1 Time-Series and Seismicity

The seismic activity in São Miguel is mainly concentrated in the central part of the island, from the Fogo volcano to the Congro fissure zone. The seismic activity is characterized by many small-magnitude events along the main fault system (Figure 4.2). Most seismic events in the area have hypocenters above the 5 km depth level. Evidence of volcano deformation at Fogo volcano, with both inflation and deflation, is inferred from the time series of continuous GNSS stations RIB1, RCHA, BVF1, VFDC, and PCNG located in the area (see Figure 3.2C).

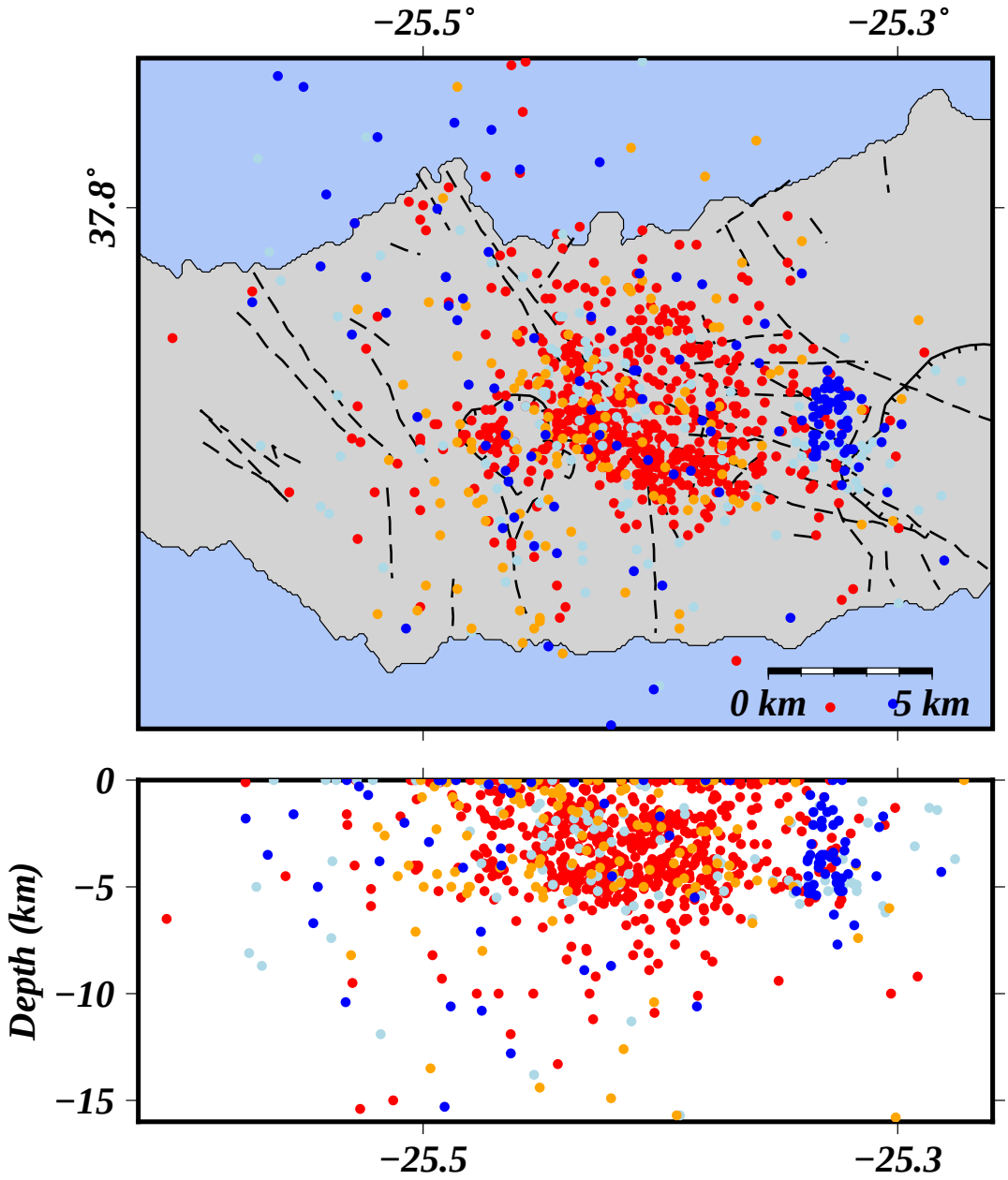

Figure 4.2: Seismic activity in the central area of São Miguel. Colored circles are recorded earthquakes ($M_D \geq 2$) between 2004 and 2016 (CIVISA database). Circles in red are from 2004-2006, light blue from 2007-2011, orange from 2011-2013, and dark blue from 2013-2016. Dashed lines are faults and volcanic alignments (Carmo et al., 2015).

The time series of the RIB1 continuous GNSS station for the period between 2002 and 2016 (Figure 4.3A) located on the north flank of Fogo volcano shows transient deformation mainly in 2004-2006, 2011-2013, and 2013-2016.

For the 2002-2004 period, the time series of the RIB1 station shows differential motion to NW direction, away from the Fogo volcano, and consistent with inflation. There is an increment in seismicity and a relatively higher number of volcanic events during this period.

The seismic and geodetic data show that the activity in the Fogo volcano peaked in 2005. The time series of the RIB1 station shows an increase in the displacement rate to NW during 2005, consistent with higher inflation. During that year, a maximum of ∼1500 ($M_D \geq 2$) earthquakes are recorded. May and September of 2005 show higher seismic activity, with 270 and 280 events ($M_D \geq 2$) recorded, respectively. By comparison, 560 seismic events ($M_D \geq 2$) are recorded between September 2004 and April 2005. The largest magnitude earthquakes recorded in the study period occurred in September 2005. These are three events of magnitude 4.0-4.2 (M_L) at 2-4 km depth.

The time series of the RIB1 station shows a decrease in the displacement rate to NW in 2006-2007 and no significant deformation in 2007-2011. In general, the number of recorded seismic events gradually decreased from 2005 to 2011, but smaller seismic swarms were recorded in this period, namely in mid-2007 and late 2008. Besides increased seismic activity in 2011-2013, the time series of the RIB1 station shows an increase in the displacement rate to NW, consistent with inflation. After 2013, there was an inversion in the displacement rate direction to SE towards the volcano, consistent with deflation. The activity was primarily aseismic between 2013 and 2016, with only minor seismic unrest recorded in the eastern rim of Furnas volcano in late 2014.

4.2 Modeling

Histograms from GBIS software showing the posterior density functions of parameters from best fit sources are shown in Figures B1, B2, B3 and B4 in Appendix B.

For the 2004-2006 and 2011-2013 periods, the statistics shows that more complex models have lower χ^2_ν than the point-pressure source model (Table 4.1). For the 2004-2006 period, the spheroid source model has lower χ^2_ν, and for the 2011-2013 period, the models with a spheroid source and a penny source have lower χ^2_ν. The F-test results show that the null hypothesis is not violated with a spheroid model for the 2004-2006 period (Table 4.2), indicating that this model does not explain the deformation field better than the point-pressure model for this period. On the other hand, the F-test results show that the null hypothesis is violated with a 99% chance with a spheroid model for the 2011-2013 period, indicating that this model can better explain the deformation field than the point-pressure model for this period.

For the 2013-2016 deflation, the χ^2_ν statistics shows that a point-pressure source model is a better fit to the GNSS data than the other models since the other models have higher χ^2_ν and higher number of parameters compared with the point-pressure source model.

Table 4.1: Best fit model parameter results for Mogi's point-pressure (M), Yang's spheroid (Y), and Fialko's penny (F) sources (S) for the main periods (P) of deformation 2004-2006, 2011-2013 and 2013-2016. D is the source depth, and a represents the radius of the penny source and the major axis of the prolate spheroid source (km). A represents the ratio between the minor and major axis of the prolate spheroid source. ϕ and θ denote the strike and dip of prolate spheroid source, respectively (°). $\Delta P/\mu$ is the dimensionless excess pressure and ΔV the volume change for each period (10^6 m^3). Modified from D'Araújo et al. (2022).

P	S	Lon.	Lat.	D	a	A	ϕ	θ	$\Delta P/\mu$	ΔV
	M	-25.432	37.779	3.7						9.6
2004-2006	Y	-25.421	37.775	4.8	0.5	0.3	88	-24	0.18	
	F	-25.425	37.780	7.1	0.4				0.10	
	M	-25.461	37.766	3.3						1.1
2011-2013	Y	-25.463	37.766	3.4	0.2	0.2	208	-52	1.10	1.6*
	F	-25.458	37.763	6.1	0.1				0.19	
	M	-25.452	37.774	3.2						-3.6
2013-2016	Y	-25.451	37.773	3.2	0.1	0.8	29	-7	-0.19	
	F	-25.456	37.773	5.2	0.4				-0.02	
	M	-25.445	37.767	4.4						4.5
2018-2019	Y	-25.445	37.770	3.6	0.4	0.3	-82	321	0.1	5.8*
	F	-25.447	37.767	6.6	0.3				0.16	

*Yang's spheroid ΔV is calculated as $\pi \frac{\Delta P}{\mu} a^3 A^2 (A^{\frac{2}{3}} - 0.7A + 1.37)$

(Battaglia et al., 2013)

Table 4.2: Summary of chi-square and F-test statistics for model results using Mogi's point-pressure (M), Yang's spheroid (Y), and Fialko's penny (F) sources (S) for the main periods of deformation 2004-2006, 2011-2013, 2013-2016 and 2018-2019. Nd is the number of data points, Np is the number of model parameters, and ν is the number of degrees of freedom. χ^2 and χ^2_ν are the chi-square and chi-square per degree of freedom, respectively. The F statistic and the critical values F_{crit} of the F-distribution with 95% and 99% significance are also presented for the smaller χ^2_ν obtained with more complex models. Modified from D'Araújo et al. (2022).

Period	Nd	S	Np	ν	χ^2	${\chi_\nu}^2$	F	$F_{crit}[95\%]$	$F_{crit}[99\%]$
		M	4	18	56.2	3.1			
2004-2006	22	Y	8	14	40.8	2.9	1.3	3.8	7.0
		F	5	17	71.3	4.2			
		M	4	18	63.6	3.5			
2011-2013	20	Y	8	14	11.8	0.8	15.3	3.8	7.0
		F	5	17	50.7	3.0	1.5	4.5	8.4
		M	4	18	30.0	1.5			
2013-2016	22	Y	8	14	28.9	1.8			
		F	5	17	57.0	3.0			
		M	4	18	53.0	2.9			
2018-2019	25	Y	8	14	24.4	1.7	4.2	3.8	7.0
		F	5	17	114.0	6.7			

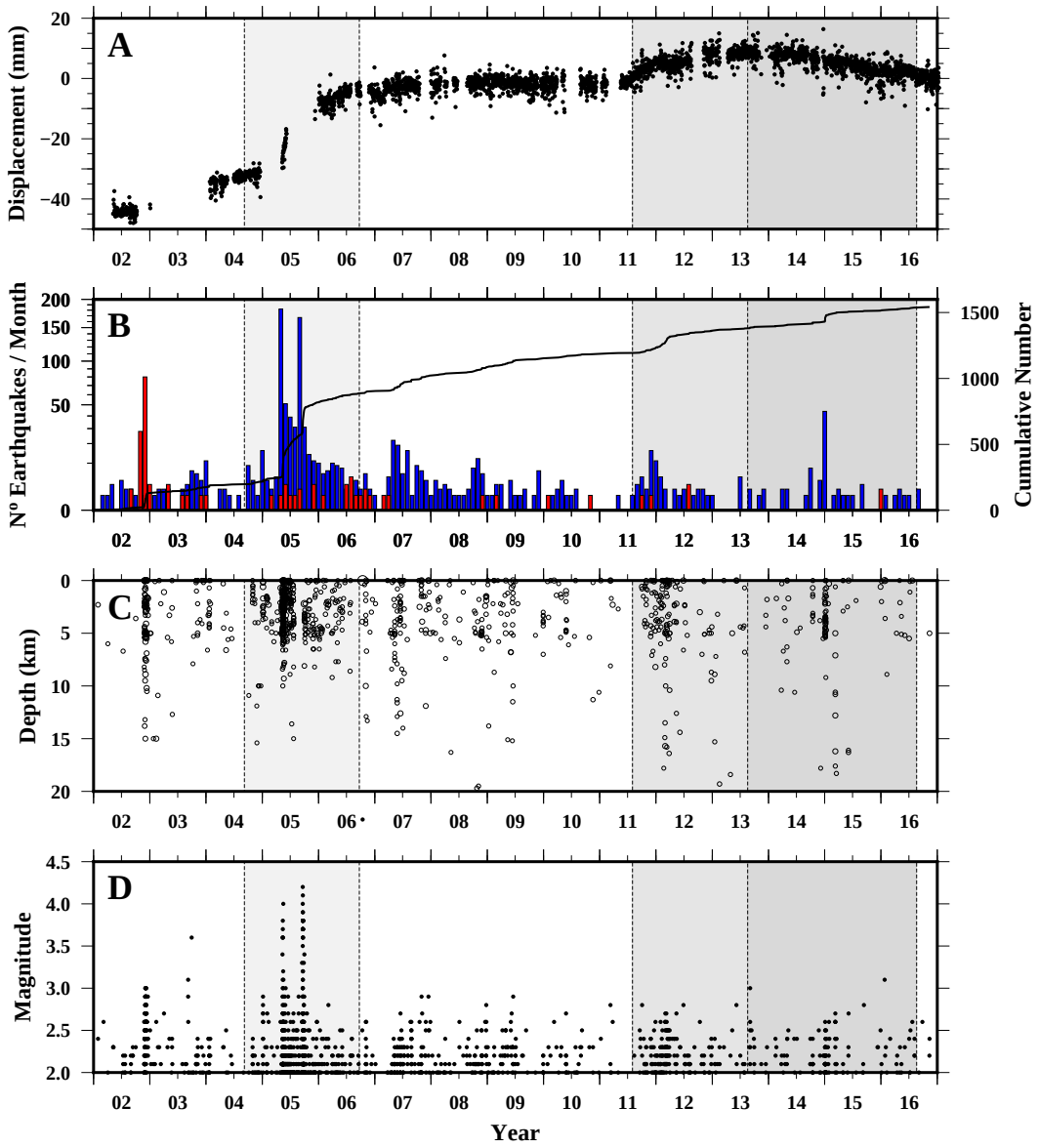

Figure 4.3: A - Time series of the horizontal component of station RIB1 in the N45°W (NW) direction between 2002 and 2016. B - Monthly number of earthquakes ($M_D \geq 2$), including volcano-tectonic events (blue) and volcanic events (red). The black line is the cumulative number of earthquakes. C - Depth of earthquakes. D - Magnitude of earthquakes. The grey panels represent the three main episodes of volcano deformation (2004-2006, 2011-2013, and 2013-2016). Reproduced from D'Araújo et al. (2022).

4.3 Velocity Field

4.3.1 2004-2006 Inflation

The 2004-2006 velocity field (Figure 4.4) is consistent with inflation and expansion centered in an area east of Fogo caldera. In the 2004-2006 period, a maximum uplift of 4.3 $\pm$ 3.5 cm yr^{-1} was recorded at MLOB station, located to the northeast of Fogo caldera. More than 600 earthquakes ($M_D \geq 2$) were recorded in this period.

The low inflation rate between 2002 and 2004 inferred from the time series of the RIB1 continuous GNSS station indicates that the inflation started before 2004, as suggested (Trota, 2008) previously. Many low-frequency volcanic events, which can be associated with the movement of fluids such as magma or hydrothermal water inside cracks (Cusano et al., 2008; Kumagai et al., 2002; Shapiro et al., 2017), occurred in late 2002, suggesting that volcanic fluids were accumulated below Fogo volcano before 2004.

During the 2004-2006 period, the seismic activity was dispersed over a broad radial area, with most events located between the Fogo caldera and the Congro fissure zone. The center of this area is where the best fit point-pressure modeled source is located (see Table 4.1). At the 95% confidence level, the 2004-2006 best fit point-pressure source model result gives a volume increase in the range of $8.8 - 10.4 \times 10^6$ m^3 at a depth of 3.4-4.1 km to the east of Fogo caldera. The 2004-2006 unrest can be explained by the intrusion of volcanic fluids in the Monte Escuro area to the east of Fogo caldera.

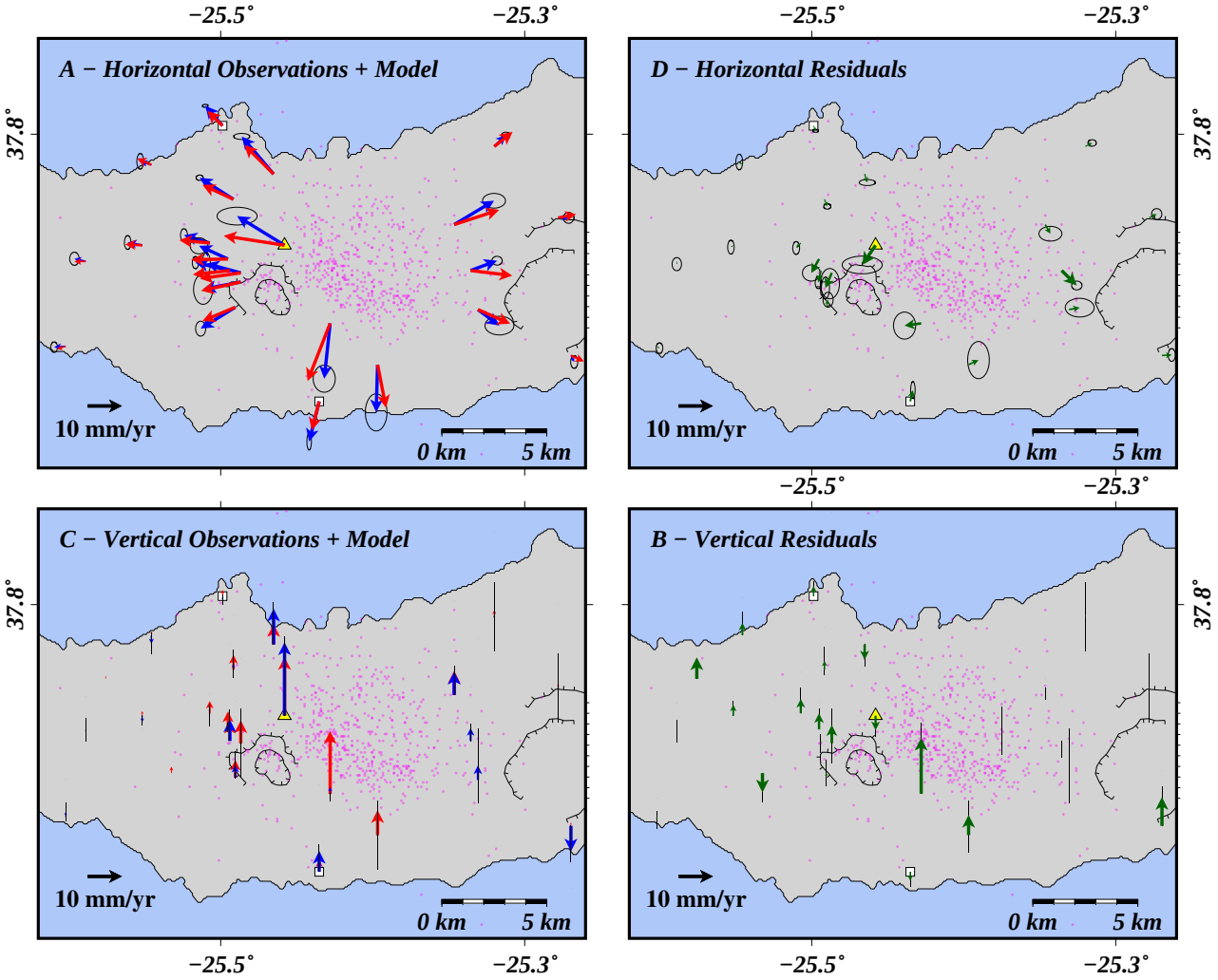

Figure 4.4: A - 2004-2006 horizontal displacements, observed (blue) and modeled (red). B - Horizontal residuals. C - Vertical displacements, observed (blue) and modeled (red). D - Vertical residuals. Colored circles are recorded earthquakes ($M_D \geq 2$). Yellow triangle is the episodic GNSS station MLOB located close to Monte Escuro. White squares are the continuous GNSS stations.

4.3.2 2007-2011 Stable Period

The 2007-2011 period was relatively quiet, with much less earthquake activity than the other periods and no significant deformation recorded (Figure 4.5). In this period, there was, however, a minor displacement in the time series of the PCNG continuous GNSS station located in the Congro fissure zone. In late 2008, there was a sudden displacement at the PCNG station towards north (Figure 4.6) as reported earlier (J. Okada et al., 2015) previously. However, the other continuous GNSS stations to the west, closer to the Fogo volcano, do not show significant displacements. The lack of significant displacement in other stations suggests that the deformation was localized in the Congro volcanic system, which can relate to readjustments in the area and faulting activity after the 2004-2006 unrest. The three episodic GNSS stations closer to the Fogo caldera show minor subsidence, but the lack of deformation in other stations does not support the existence of a general deflation of the Fogo volcano edifice in the 2007-2011 period.

During this period, the small seismic activity was focused in two main areas, the Monte Escuro area to the northeast of Fogo caldera, where the 2004-2006 best fit modeled source is located, and at the western rim of Furnas caldera.

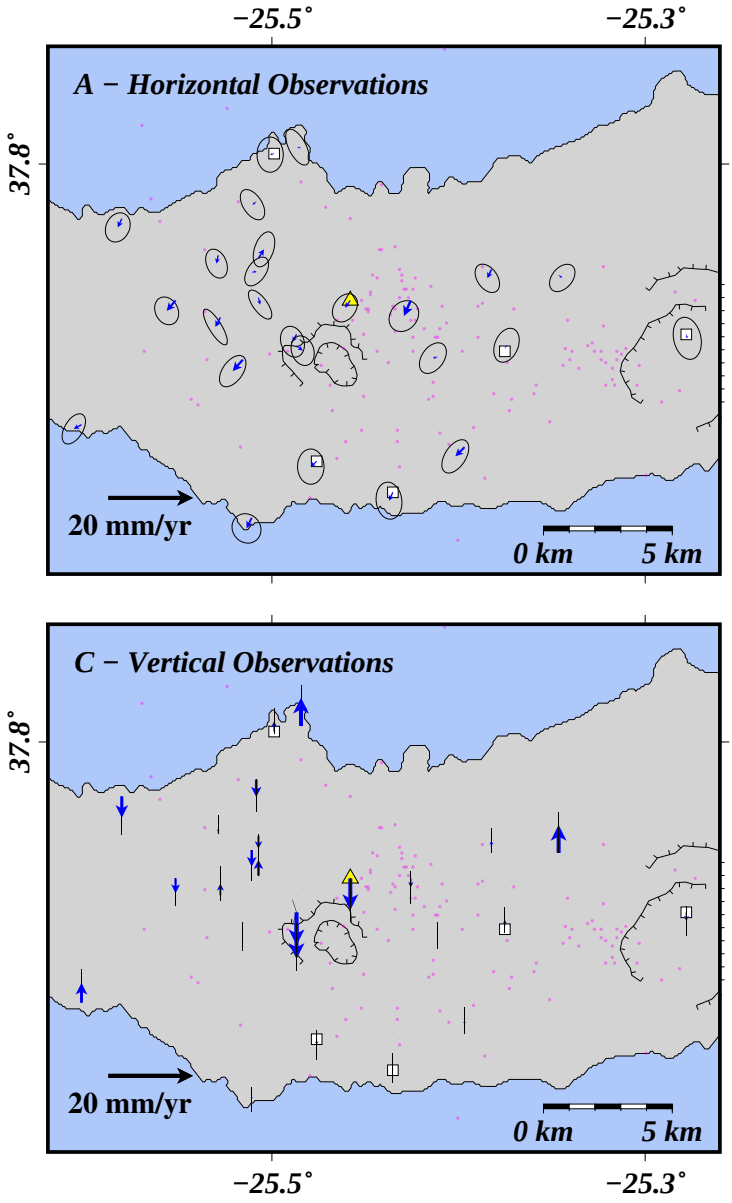

Figure 4.5: A - 2007-2011 horizontal observations. B - Vertical observations. Colored circles are recorded earthquakes ($M_D \geq 2$).

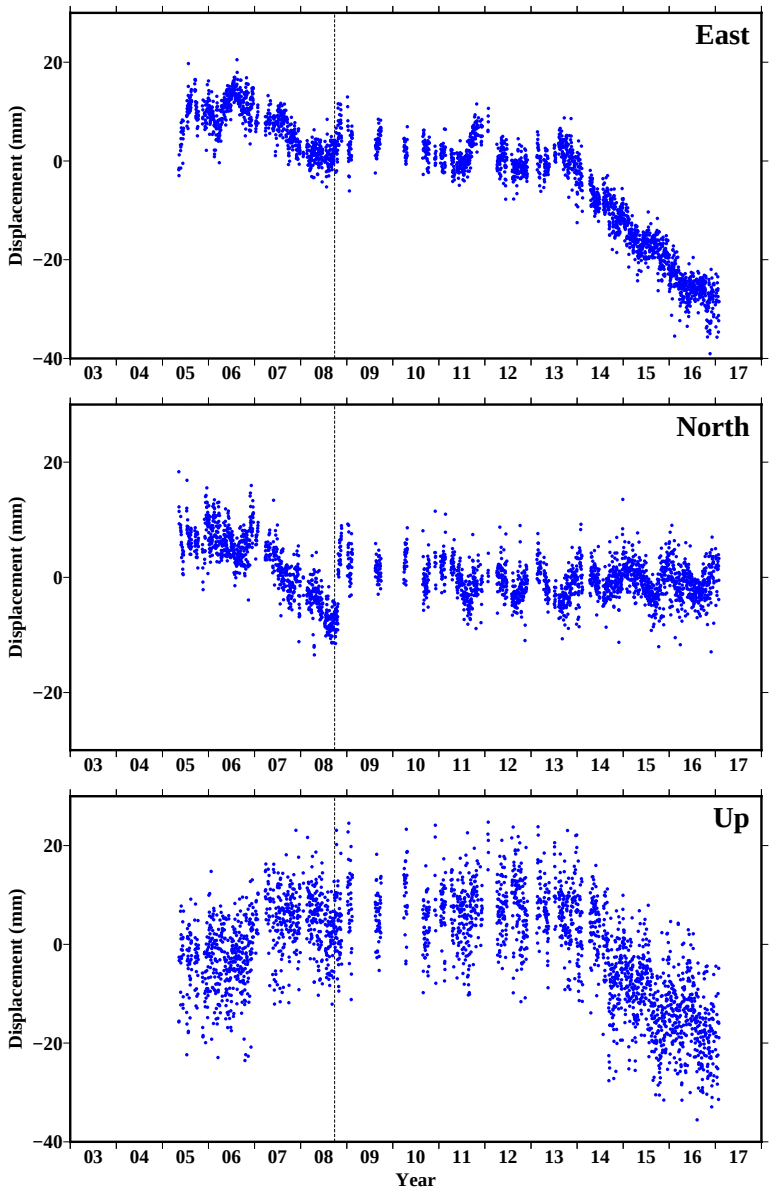

Figure 4.6: Time series of displacement (east, north and up components from top to bottom) at the continuous GNSS station PCNG located in the Congro fissure zone, relative to predicted Eurasian motion. The vertical dashed lines mark the sudden displacement at the station in late 2008, as reported earlier (J. Okada et al., 2015). Yellow triangle is the episodic GNSS station MLOB located close to Monte Escuro. White squares are the continuous GNSS stations.

4.3.3 2011-2013 Inflation

The 2011-2013 velocity field (Figure 4.7) is consistent with inflation and expansion centered in an area east of Fogo caldera. The magnitude of the 2011-2013 inflation is smaller than the 2004-2006 inflation. In the 2011-2013 period, an uplift of 1.8 $\pm$ 0.6 cm yr^{-1} was recorded at MLOB station. Around 70 earthquakes ($M_D \geq 2$) were recorded in this period.

The GNSS and seismic data show that the 2011-2013 activity was much lower compared to the 2004-2006 period. At the 95% confidence level, the 2011-2013 best fit point-pressure source model result gives a volume increase in the range of $0.7 - 5.4 \times 10^6$ m^3 at a depth of 2.4-4.9 at the eastern rim of Fogo caldera (see Table 2.2). Statistical analysis of the modeling results shows that a spheroid source can better explain the 2011-2013 deformation field (see Table 2.3). The 2011-2013 spheroid source is elongated in the direction NNE-SSW to NE-SW, dipping 52° vertically. The lower activity and differences in source location and shape in the 2011-2013 period compared to the 2004-2006 period suggest that the two periods of activity are related to different processes.

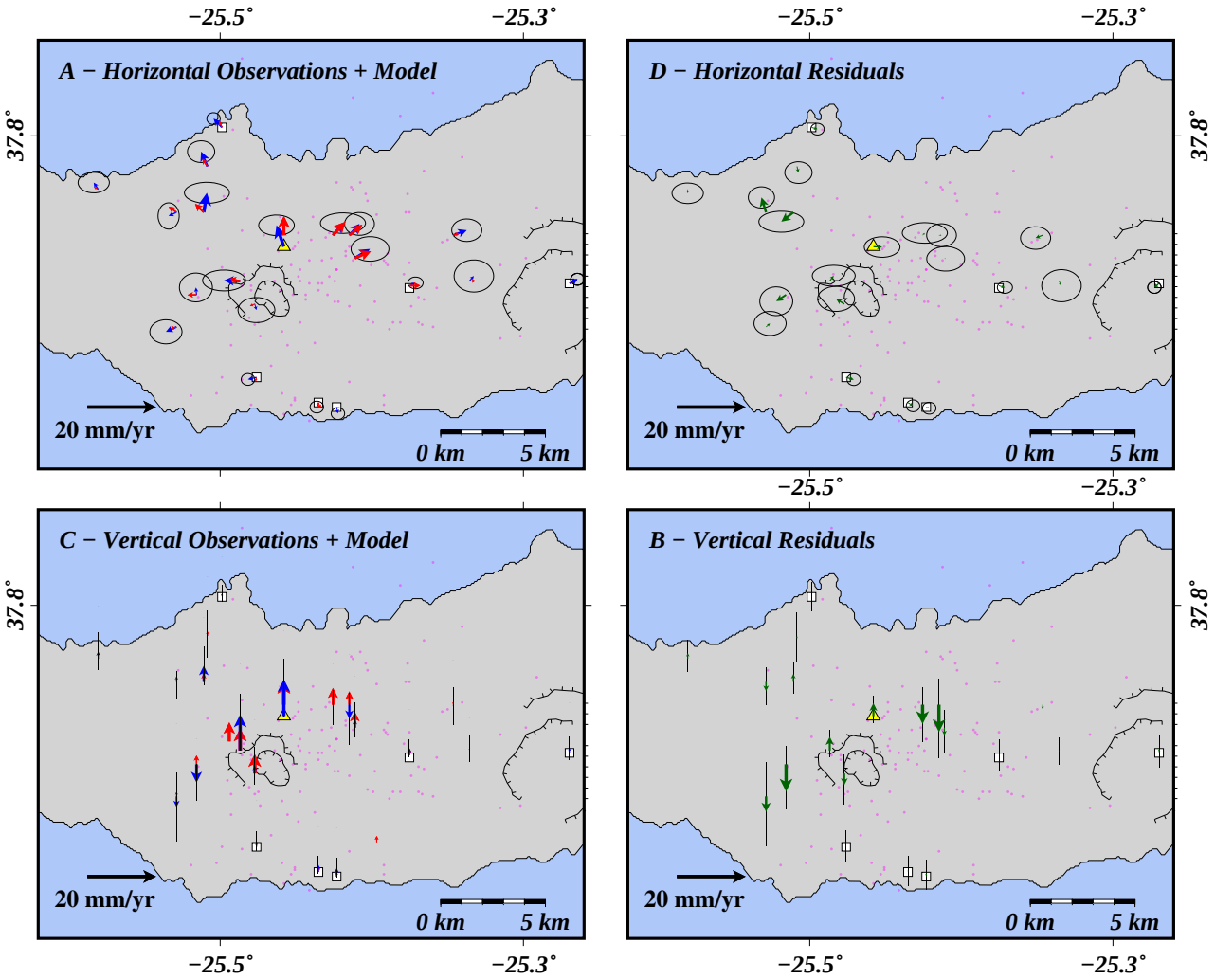

Figure 4.7: A - 2011-2013 horizontal displacements, observed (blue) and modeled (red). B - Horizontal residuals. C - Vertical displacements, observed (blue) and modeled (red). D - Vertical residuals. Colored circles are recorded earthquakes ($M_D \geq 2$). Yellow triangle is the episodic GNSS station MLOB located close to Monte Escuro. White squares are the continuous GNSS stations. Modified from D'Araújo et al. (2022).

4.3.4 2013-2016 Deflation

The 2013-2016 velocity field (Figure 4.8) is consistent with deflation and contraction centered in an area east of Fogo caldera. In this period, subsidence of 1.7 ± 1.0 cm yr^{-1} was recorded at MLOB station and around 80 earthquakes ($M_D \geq 2$) were recorded.

In contrast to the 2004-2006 and 2011-2013 inflation episodes, the 2013-2016 deflation is mostly aseismic. The deformation field of this period could be explained by the contraction of a volume centered in the Vale das Lombadas area, in the northeastern rim of Fogo caldera, between the two inflation centers. At the 95% confidence level, the 2013-2016 best fit point-pressure source model result gives a volume decrease in the range of $3.1 - 4.4 \times 10^6$ m^3 at a depth of 3.0-3.8 km at the northeastern rim of Fogo caldera.

During the 2013-2016 period, a seismic swarm occurred in the western rim of Furnas caldera, in the same area where seismicity was more active during the 2007-2011 period.

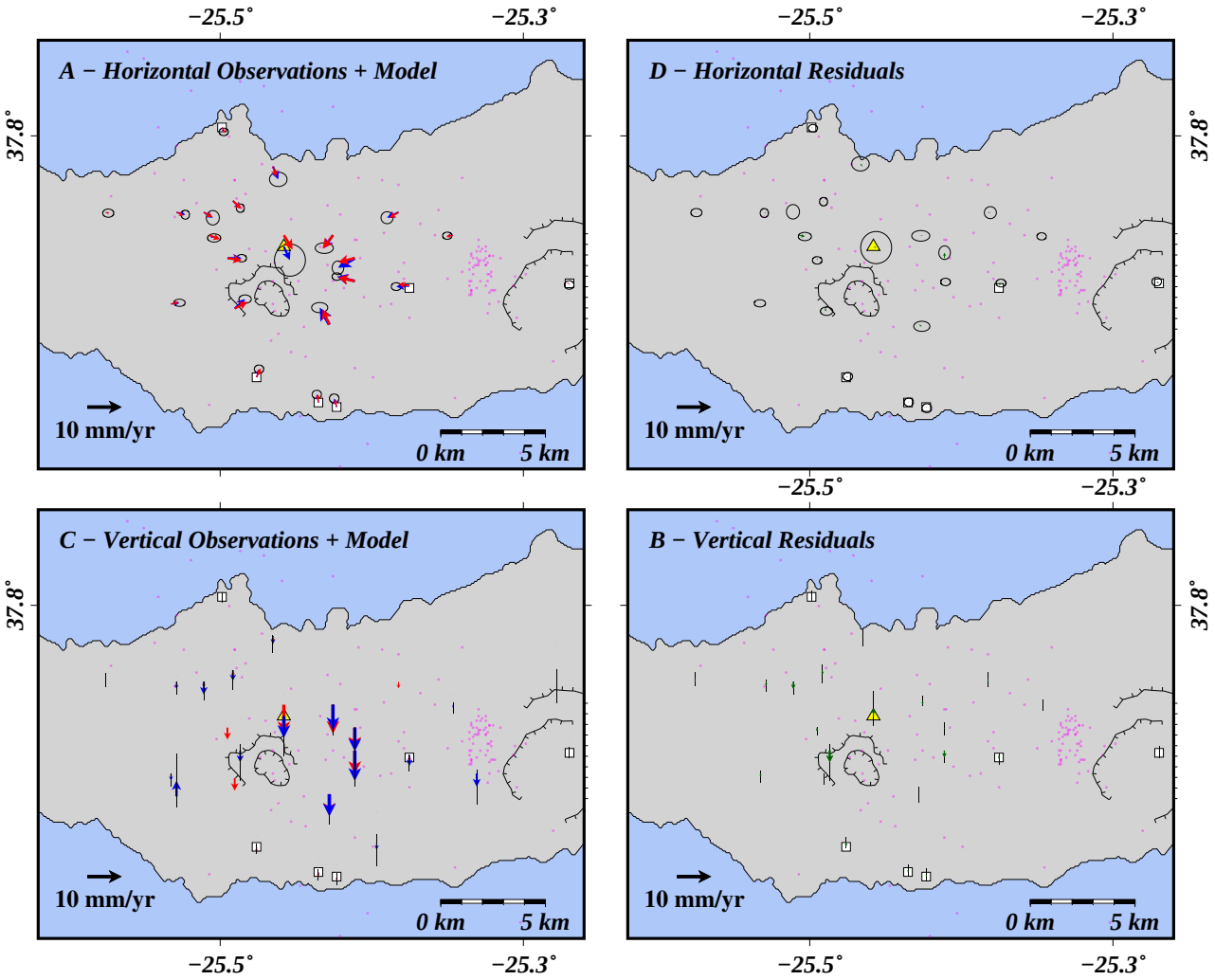

Figure 4.8: A - 2013-2016 horizontal displacements, observed (blue) and modeled (red). B - Horizontal residuals. C - Vertical displacements, observed (blue) and modeled (red). D - Vertical residuals. Colored circles are recorded earthquakes ($M_D \geq 2$). Yellow triangle is the episodic GNSS station MLOB located close to Monte Escuro. White squares are the continuous GNSS stations. Modified from D'Araújo et al. (2022).

4.3.5 2018-2019 Inflation

The 2018-2019 velocity field (Figure 4.9) is consistent with inflation and expansion centered east of the Fogo caldera. A maximum uplift of 2.6 ± 1.6 cm yr^{-1} was recorded at MLOB station in this period. The seismic activity in the 2018-2019 period was distributed over a broad area, with most events located between the Fogo caldera and the central part of the Congro fissure zone.

The LOS velocity map from InSAR data analysis between May 2017 and February 2018 (Figure 4.10A) shows an extended area to the east of Fogo caldera with displacement away from the satellite, consistent with deflation. In contrast, the velocity map between February 2018 and November 2018 (Figure 4.10B) shows an extended area in the Fogo caldera with displacement towards the satellite, consistent with inflation.

The time series of the north component of continuous GPS station BVF1 (Figure 4.11), located in the south flank of Fogo volcano, shows a relatively stable displacement before February 2018. The time series of a pixel with high coherence from InSAR data analysis located in the eastern rim of Fogo caldera shows a displacement away from the satellite, consistent with deflation. The start of the seismic activity in early 2018 was abrupt, with most seismic events occurring in a single day, on 12 February 2018.

After the seismic activity in 12 February 2018, the time series of the BVF1 station and the InSAR pixel changed direction towards the south and the satellite, respectively. The displacement direction change is consistent with inflation, which continued until mid-2019.

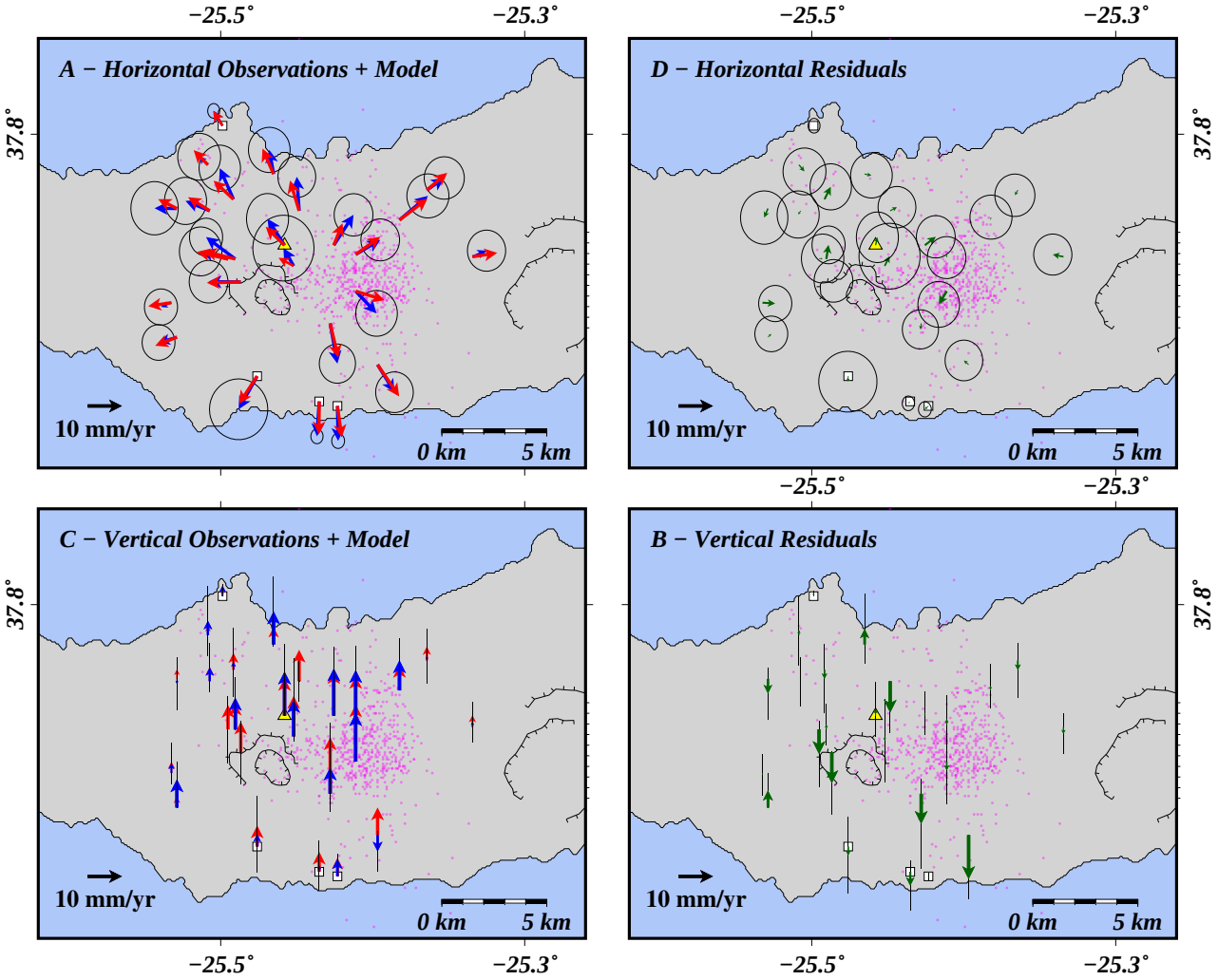

Figure 4.9: A - 2018-2019 horizontal displacements, observed (blue) and modeled (red). B - Horizontal residuals. C - Vertical displacements, observed (blue) and modeled (red). D - Vertical residuals. Colored circles are recorded earthquakes ($M_D \geq 2$).

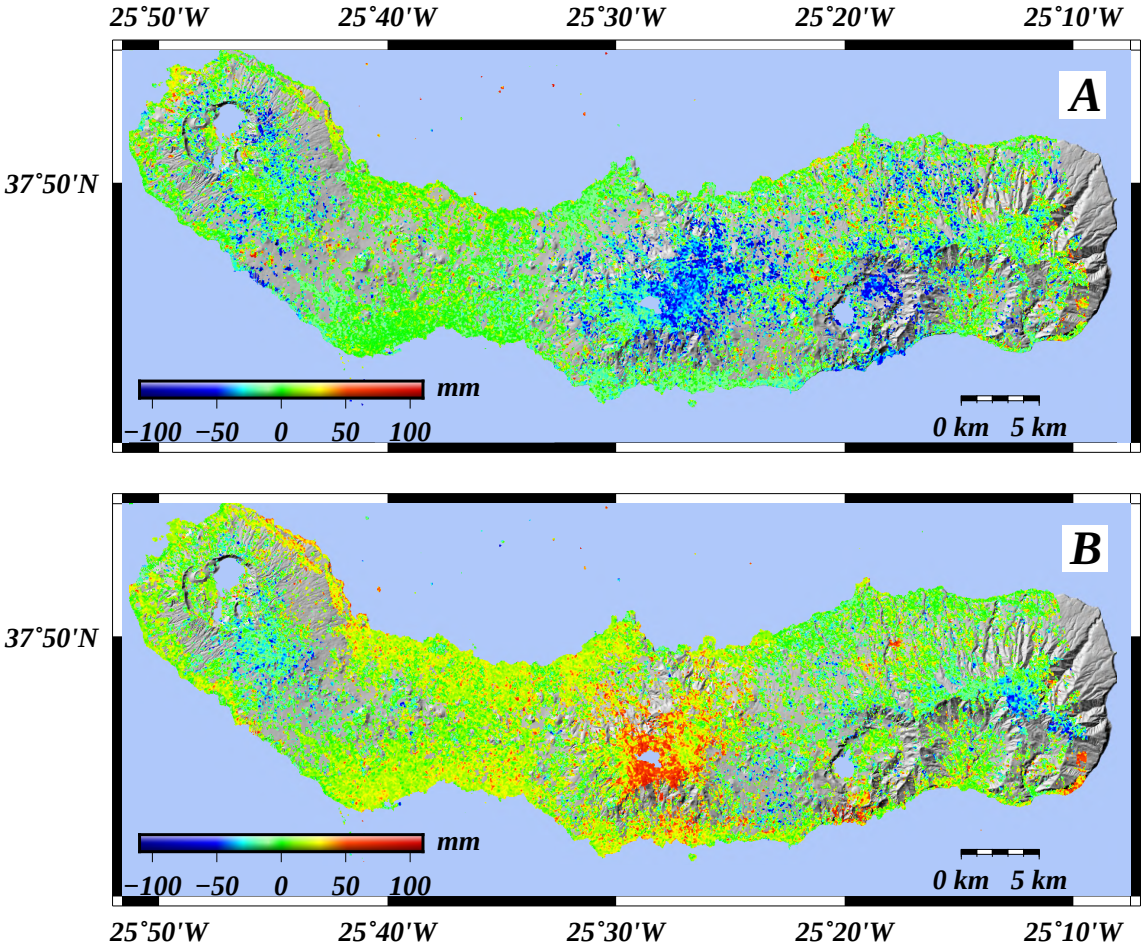

Figure 4.10: LOS velocity map derived from 61 interferograms (see Figure 2.8). A 0.15 coherence threshold was used to mask the data projected (gray areas). Red colors represent surface displacement towards the satellite (inflation). Blue colors represent displacement away from the satellite (deflation).

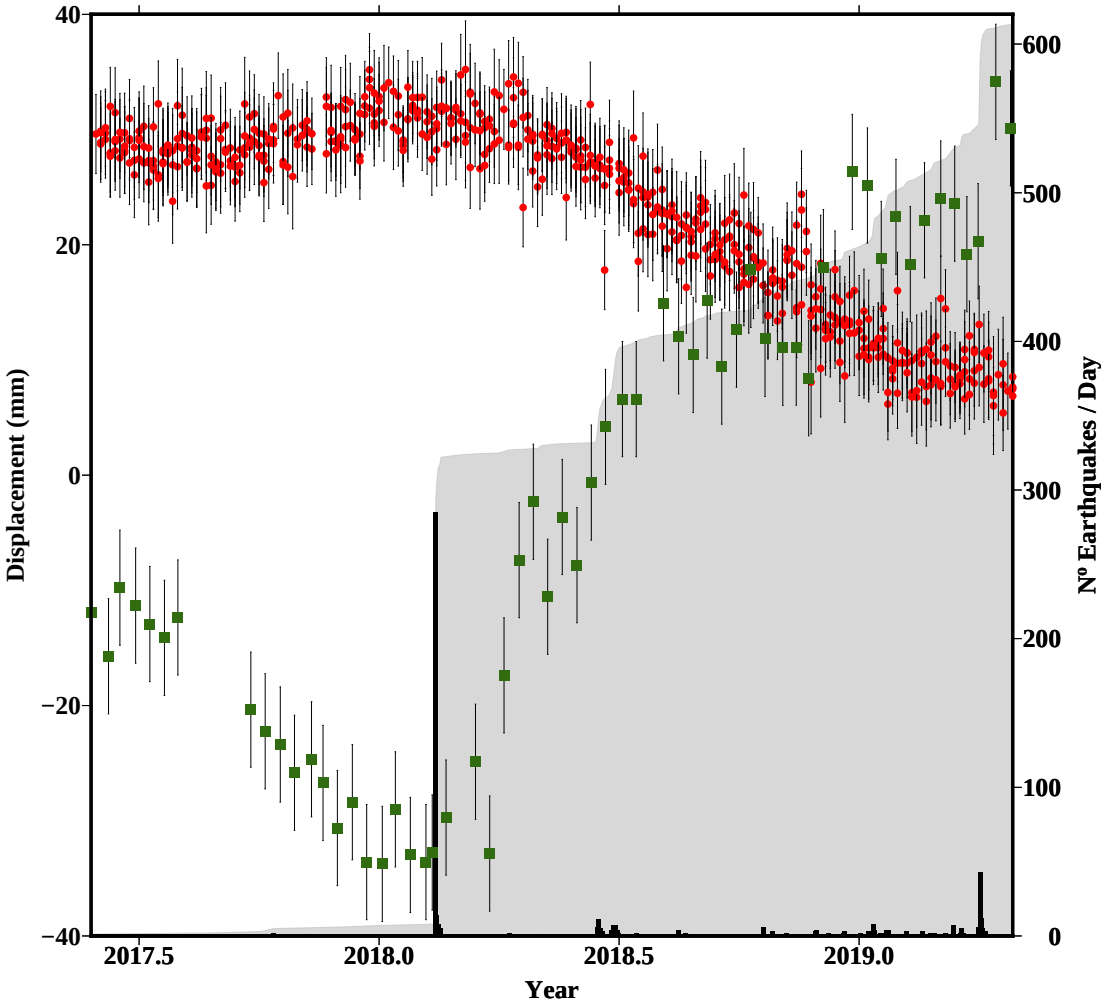

Figure 4.11: Time series of the north component of BVF1 continuous GNSS station relative to predicted Eurasian plate motion from June 2017 to June 2019 (red) and time series of LOS displacement of Sentinel-1 ascending track from a point located at Fogo volcano (-25.426°W; 37.765°N). The vertical black bars are the daily number of best-located earthquakes, and the grey area is the cumulative number of earthquakes. Yellow triangle is the episodic GNSS station MLOB located close to Monte Escuro. White squares are the continuous GNSS stations.

4.4 Discussion

In 2004-2016, most seismic events in the central part of São Miguel Island were recorded at shallow depths in the range of 0-5 km, the level where the best fit modeled sources are located (3.2-3.7 km). Besides deep processes below the Fogo volcano, other shallow processes may also have contributed to the activity, namely the activation of fissures at less depths. During the 2004-2006 period, surface fissures were observed in the study area (Trota, 2008).

At the 95% confidence level, the 2004-2006 best fit point-pressure source model result gives a volume increase in the range of $8.8 - 10.4 \times 10^6$ m^3 at a depth of 3.4-4.1 km to the east of Fogo caldera (Figure 4.12). For the 2011-2013 case, the best fit point-pressure source model gives a total volume increase in the range of $0.7 - 5.4 \times 10^6$ m^3 at a depth of 2.4-4.9 at the eastern rim of Fogo caldera. For the 2013-2016 case, the best fit point-pressure source model gives a total volume decrease in the range of $3.1 - 4.4 \times 10^6$ m^3 at a depth of 3.0-3.8 km at the northeastern rim of Fogo caldera. For the 2018-2019 case, the best fit point-pressure source model gives a total volume increase in the range of $3.8 - 5.4 \times 10^6$ m^3 at a depth of 4.0-5.1 km at the northeastern rim of Fogo caldera.

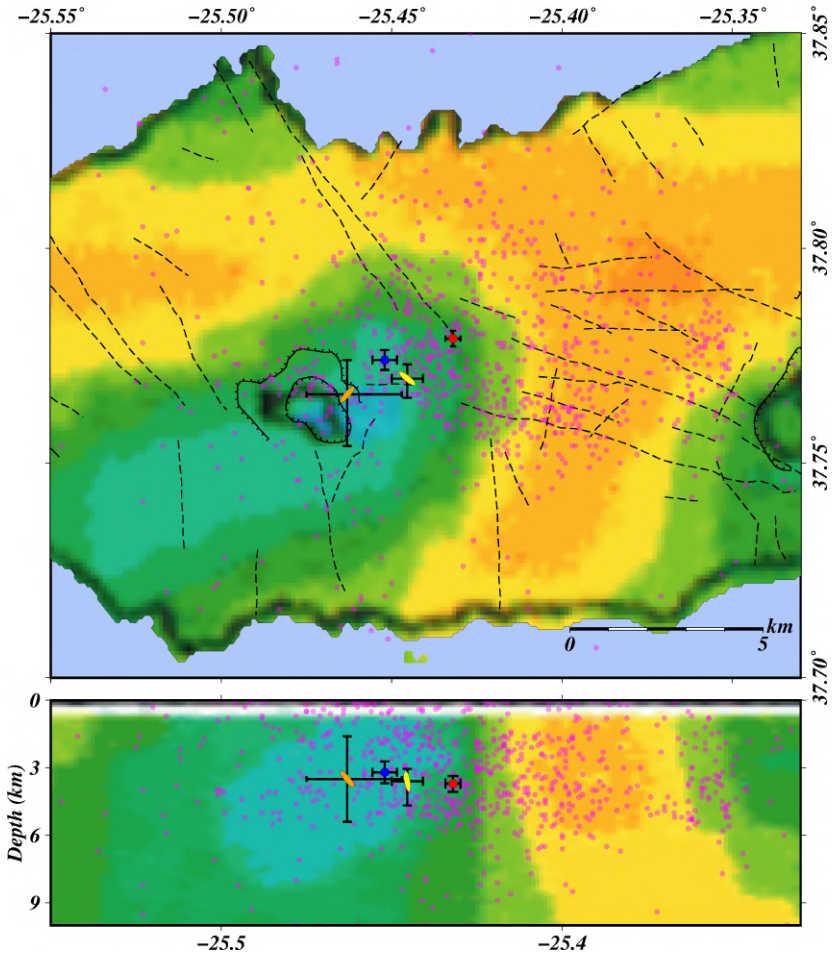

Figure 4.12: Horizontal location (top) and E-W depth profile (bottom) showing the best fit location of center of modeled sources, and their 95% confidence intervals, for the main periods of deformation. Red circle is the 2004-2006 best-fit point-pressure source (inflation). Orange ellipse is the 2011-2013 best-fit prolate spheroid (inflation). Blue circle is the 2013-2016 best-fit point-pressure (deflation). Yellow ellipse is the 2018-2019 best-fit prolate spheroid (inflation). Shape of best-fit sources is indicative, but does not represent their size. Color map represents anomalous density contrast in the area obtained from gravimetric inversion for the horizontal section at 4 km depth (top) and vertical E-W depth profile at latitude 37.76° (Camacho et al., 1997). Dashed lines are faults and volcanic alignments (Carmo et al., 2015). Pink circles are recorded earthquakes during the modeled periods of deformation. ($M_D \geq 2$). Modified from D'Araújo et al. (2022).

The eruptive activity of Fogo in the last thousands of years has been characterized by basaltic flank eruptions and trachytic explosive activity in the summit area (Moore, 1990; Walker & Croasdale, 1971; Wallenstein, 1999). Petrological analysis of rock samples from field deposits of previous eruptions at Fogo volcano suggests that a single magma chamber has been the source of the most recent trachytic volcanism (Storey, 1982; Widom et al., 1992). However, details about the location and depth of a trachytic magma chamber below the Fogo volcano still need to be better understood.

The 2004–2006 best-fit source is located close to the Monte Escuro cinder cone (see Figure 4.12), in an important fault system at depths of about 4 km. The location is about 3 km northeast of the Fogo caldera. The slow displacement of the RIB1 station and relatively higher number of volcanic seismic events in the 2002-2004 period suggest the accumulation of magma before the 2004-2006 inflation. The lack of significant subsidence after the 2004–2006 inflation can be explained by the permanence of a newly intruded magma body. The suggested spreading in the area (D'Araújo et al., 2022) can facilitate the gradual ascension of magma below the Fogo volcano.

The 95% confidence intervals of the locations of the 2011–2013 and 2013–2016 best-fit sources overlap. These sources are located in an area comprising the eastern and northeastern rim of the Fogo caldera (see Figure 4.12) at depths of 3.2–3.5 km. The 95% confidence intervals for the volume change from the 2011–2013 and 2013–2016 best-fit sources also overlap. The location and volume estimates of the 2011–2013 and 2013–2016 best-fit sources suggest that the two changes in volume are related to the same body at depth. The inflation-deflation reversal from 2011–2013 to 2013–2016 may relate to differences in properties of the 2011–2013 pressure increase compared with the 2004–2006 episode, such as higher content

of gas and differences in the rock medium surrounding the center of inflation, such as higher permeability. The location of the 2011–2013 and 2013–2016 best-fit sources, in an area with a low-density minimum below Fogo caldera (Camacho et al., 1997), suggest that the 2011–2013 pressure increase may have been in the magma chamber or hydrothermal system of the Fogo volcano. The 2013–2016 deflation can be explained by a similar process as described by J. Okada et al. (2015), of lateral diffusion of fluids percolating through existing fissures re-activated from local spreading and previous volcanic unrest in 2004–2006 and 2011–2013.

The 95% confidence intervals of the location of the 2018–2019 best-fit source overlap with the location of the 2011-2013 and 2013-2016 sources (see Figure 4.12), suggesting that the 2018–2019 source is related to the same body at depth. The abrupt seismic activity on 12 February 2022 may have marked the opening of a pathway for fluids, influencing the pressure in magma bodies or the hydrothermal system. The pressure increase after that day was mostly aseismic due to the likely accumulation of fluids at 4.5 km depth. The LOS velocity field from InSAR data shows that from early 2017 to February 2018, the Fogo volcano was still subject to deflation after the 2013-2016 period. The LOS velocity field also shows that after February 2018, inflation occurred in the Fogo caldera, where the 2011-2013 and 2013-2016 centers of pressure change estimates are located.

Only GNSS data was used to model the 2018-2019 inflation. A combined analysis of current GNSS and InSAR datasets could be tried in future analysis to test the hypothesis that the InSAR displacements reproduce an identical deformation field compared to the GNSS displacements in the same time span, allowing a joint inversion of the data.

There are numerous cases of unrest in other volcanoes with no recent eruptive activity. Campi Flegrei caldera in Italy, for example, has experienced several episodes of unrest with

ground uplift in the last decades without eruption (e.g., Battaglia et al., 2006; De Natale et al., 1991; D'Auria et al., 2015; Troise et al., 2019). Discriminating the relative contributions of hydrothermal effects and shallow magma intrusions during unrest episodes is critical at volcanoes such as Campi Flegrei and Fogo. Three main lines of interpretation try to explain the origin of the unrest episodes at Campi Flegrei in the last decades (Troise et al., 2019). These lines of interpretation state that the unrest episodes can be explained by magma intrusions at shallow depths, hydrothermal effects without the direct contribution of magma intrusions, or mixed magmatic-hydrothermal processes. Similar minor inflation episodes with rapid inflation-deflation recovery have been identified in Campi Flegrei. After the peak uplift rate of about one meter per year in 1983-1984 at Campi Flegrei, there were minor episodes of centimeter-level uplift with the duration of a few months and followed by fast recovery of the uplift, suggested to be related to the periodic increase of fluid injection in the hydrothermal system (Troise et al., 2019).

The detailed cause of ground deformation at Fogo volcano is uncertain, despite the ability to fit crustal deformation observations to models. A conceptual mixed magmatic-hydrothermal process at Fogo volcano in 2004-2019 is summarized in Figure 4.13, proposed in an attempt to explain the physical processes involved. After an inferred shallow 2004-2006 intrusion of a new magma body, likely originating from a deeper magma reservoir, the conditions for activity in the trachytic magma chamber and the hydrothermal system might be present, in relation to interaction with the 2004-2006 hot intrusion body. This interaction may have resulted in the accumulation of highly pressurized and self-contained magma-derived fluids in the magma chamber. After failure conditions between the fluid body and the host rock have been reached, fluids may have be injected into other parts of

the chamber or the hydrothermal system during the 2011-2013 and 2018-2019 intrusions. The dipping angle of the best fit elongated ellipsoid models of 2011-2013 and 2018-2019 can represent the direction of injection of fluids. The deflation in 2013-2016 indicates that the area is highly permeable. The deflation can be explained by lateral diffusion of magma-derived volatiles and hydrothermal fluids to the lower parts of the volcano, as previously suggested (J. Okada et al., 2015), facilitated by the low viscosity of the fluids and the existence of recently activated fissures during the 2004-2006 and 2011-2013 unrest.

It was not possible to detect an inferred deeper magma reservoir in this study due to the existence of multiple sources of pressure at shallower depths that would likely disturb the deformation field induced from a possible deeper source.

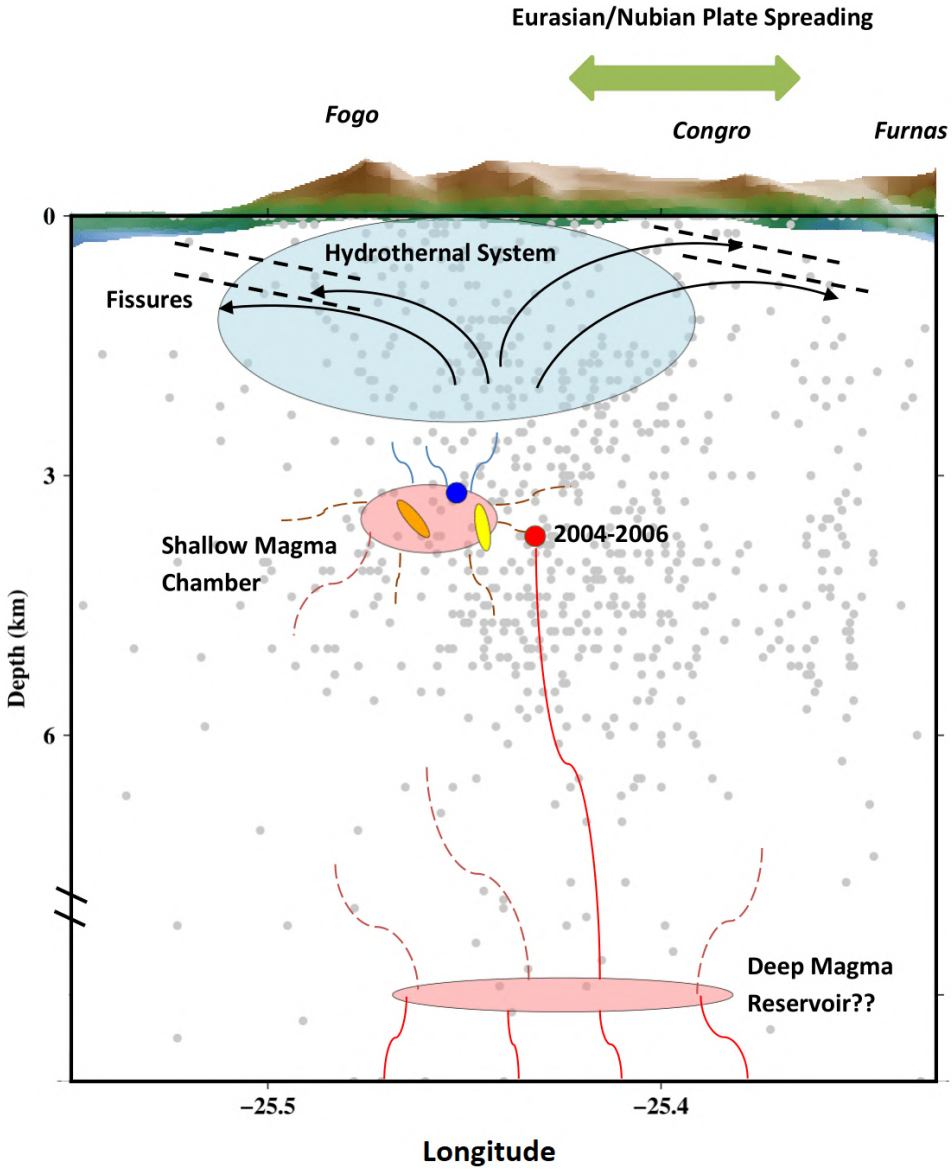

Figure 4.13: Schematic (depth-longitude profile) of suggested deep processes that occurred bellow Fogo volcano during the study period, including the 2004-2006, 2011-2013 and 2018-2019 intrusions. Red circle is the 2004-2006 best-fit point-pressure source (inflation). Orange ellipse is the 2011-2013 best-fit prolate spheroid (inflation). Blue circle is the 2013-2016 best-fit point-pressure (deflation). Yellow ellipse is the 2018-2019 best-fit prolate spheroid (inflation). Shape of best-fit sources is indicative, but does not represent their size. Large light blue area is the hydrothermal system. A shalow magma chamber is represented by a large red area where the 2011-2013, 2013-2016, and 2018-2019 best-fit sources are located. A possible deeper magma reservoir may exist at deeper levels, which may have fed the 2004-2006 intrusion. Black vectors represent diffusion of magma-derived volatiles and hydrothermal fluids to the lower parts of the volcano. Dashed black lines represent fissures. Gray circles are recorded earthquakes during the modeled periods of deformation. ($M_D \geq 2$).

Mapping of soil CO_2 degassing in Fogo volcano during the 2004-2006 unrest activity shows no significant changes (Viveiros et al., 2008). The main seismogenic areas during the activity coincide with an almost complete absence of soil diffuse degassing, eventually due to a buffer structure in depth that does not allow the gas to arise all the way to the surface.

In this study, the high spatial resolution of the GNSS data allows geodetic inversion with simple analytical models. However, the low temporal resolution of the episodic GNSS data is a limitation in calculating velocities with higher precision. In particular, the sparse data from continuous GNSS in the 2004-2006 period does not allow a detailed understanding of the deformation change in that period, whether it was gradual or sudden. The two periods with peak seismic activity in May and September of 2005 suggest the latter, with the possible occurrence of two intrusions during these months or activity related to conduit or cracks formation allowing fluid flow. The relatively higher χ^2_ν of the 2004-2006 best fit model compared to the other periods indicates that the 2004-2006 deformation field may result from multiple intrusions or was affected by other processes such as ground cracking, as mentioned previously. In addition to temporal resolution constraints, the uniform material properties assumed in the models may not adequately represent the study area due to heterogeneities and fracturing of the surface. Different rheologies, such as contrasts in shear modulus, can result in tilted ellipsoidal sources (Silverii et al., 2021), which can explain the best fit ellipsoid models of 2011-2013 and 2018-2019, which are elongated and tilted vertically.

5 São Jorge Volcano Deformation

São Jorge Island has been one of the most seismically quiet areas in the Azores in the past decades. Processes occurring on the island during the 2022 sudden unrest are here evaluated using GNSS, InSAR, and seismic data.

5.1 Seismicity

The seismic activity was mainly concentrated in the central area of São Jorge Island, in the Manadas volcanic system (Figure 5.1), and was characterized by a large number of small magnitude events ($M_D \leq 4$) along the main fault zones. Most seismic events in the area have hypocenters in the range of 3-12 km depth.

Analysis of seismic locations reveals two main stages of seismic activity during the São Jorge unrest. An initial activity occurred on March 19 with shallower events to the east, and a second activity occurred afterward with deeper events to the west (see Figure 5.1). The seismicity started on March 19, at around 6 PM, without precursory activity in the weeks before (Figure 5.2). During this day, most events were located to the east, between Pico do Carvão and Pico da Esperança, at shallow levels up to 6 km depth. The seismic activity shifted to NW after March 19, from the area between Pico do Carvão and Velas to deeper levels in the 7-12 km range. The two stages of seismic activity show events with a distinct set of epicenters and lining up on planes with different strikes. In the initial stage, seismic events show a distribution with an N115°E direction consistent with their location in the Picos Fault Zone. Events afterward show a distribution with an N105°E direction consistent with their location in the Pico do Carvão Fault Zone with a more eastward direction. The

seismicity along the N105-115°E direction follows the orientation of the main WNW-ESE fault zones on São Jorge, indicating the fault zones provided some form of control on the activity.

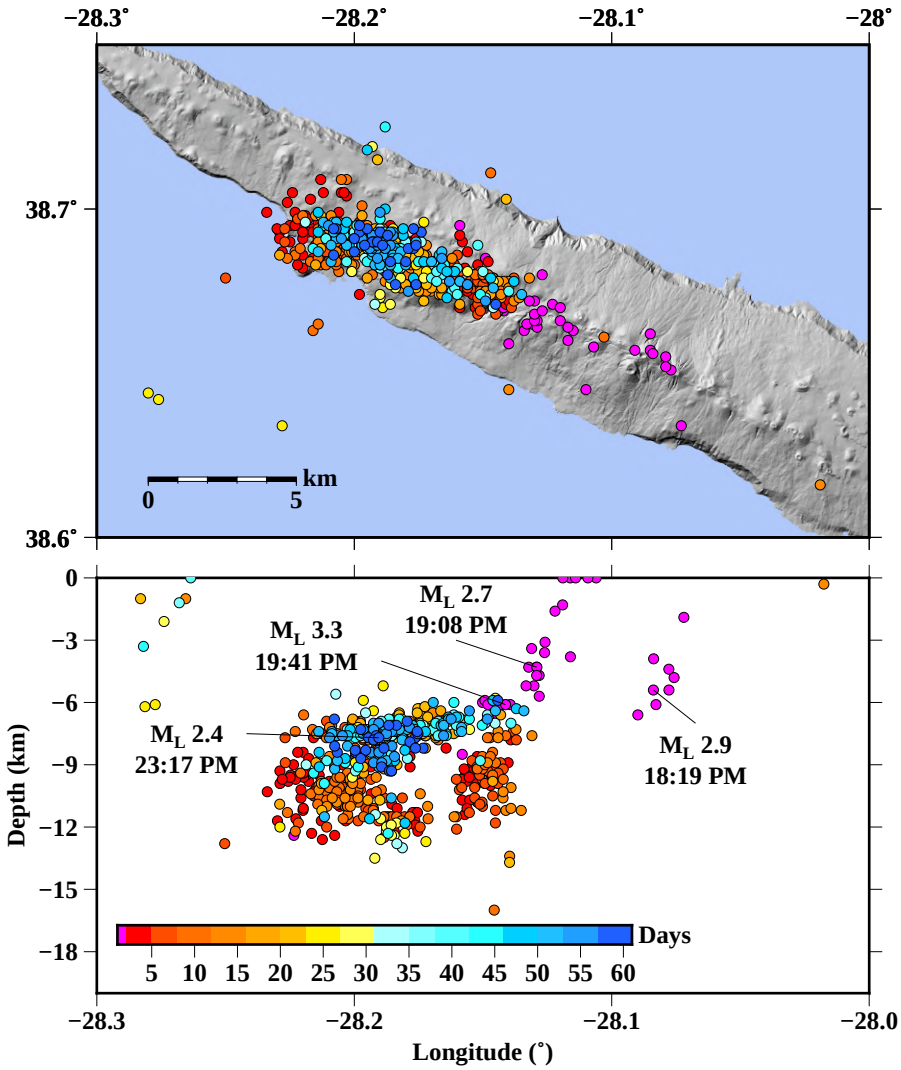

Figure 5.1: Upper - Horizontal location of best-located earthquakes during the first two months of activity between 19 March and 18 May color-coded according to their occurrence. Pink dots are earthquakes from the initial day of activity, March 19. Lower - Cross-section of best-located earthquakes during the first two months along longitude. Strongest earthquakes with magnitudes and recorded time from the four seismic clusters on March 19 related to dyke propagation are marked.

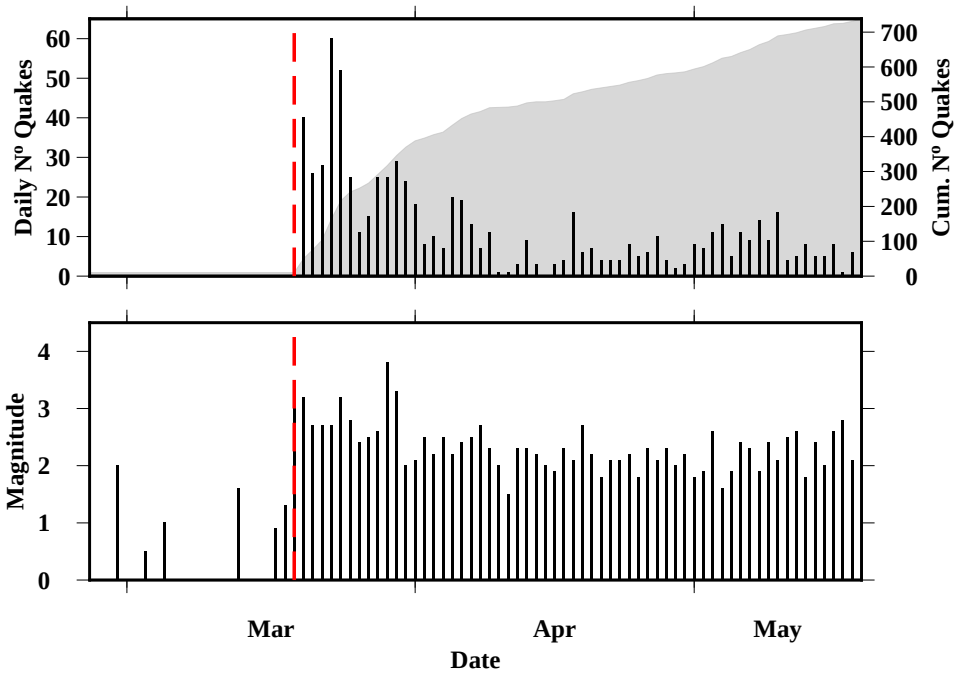

Figure 5.2: Upper - The vertical black bars are the daily number of the best-located earthquakes, and the grey area is the cumulative number of earthquakes. Lower - Maximum daily recorded magnitude (M_L). The vertical dashed lines represents 19 March.

5.2 GNSS

The sudden seismic activity during the onset of the unrest on 19 March coincides with change in position of continuous GNSS stations operating at São Jorge and neighboring islands. Deviations from their long-term behaviour occurred between 19 and 20 March (Figure 5.3). The crustal deformation associated with the event reached a distance of at least 45 km away from São Jorge. Evidence of dyke opening below São Jorge Island is inferred from the velocity field of station QEMD located at the island, and AZGR, BSRP, AZTP, and HORT stations located at the nearby islands Graciosa, Pico, and Faial. The highest displacement occurred at the BSRP station located in the north part of Pico Island, with a displacement of about 2 cm away from São Jorge Island. The displacements in the continuous GNSS stations are sudden, with most deformation occurring in the first days of activity and sharply decreasing after that. Small rate displacements in the GNSS stations continue for about two weeks and halt after that (Figure 5.4).

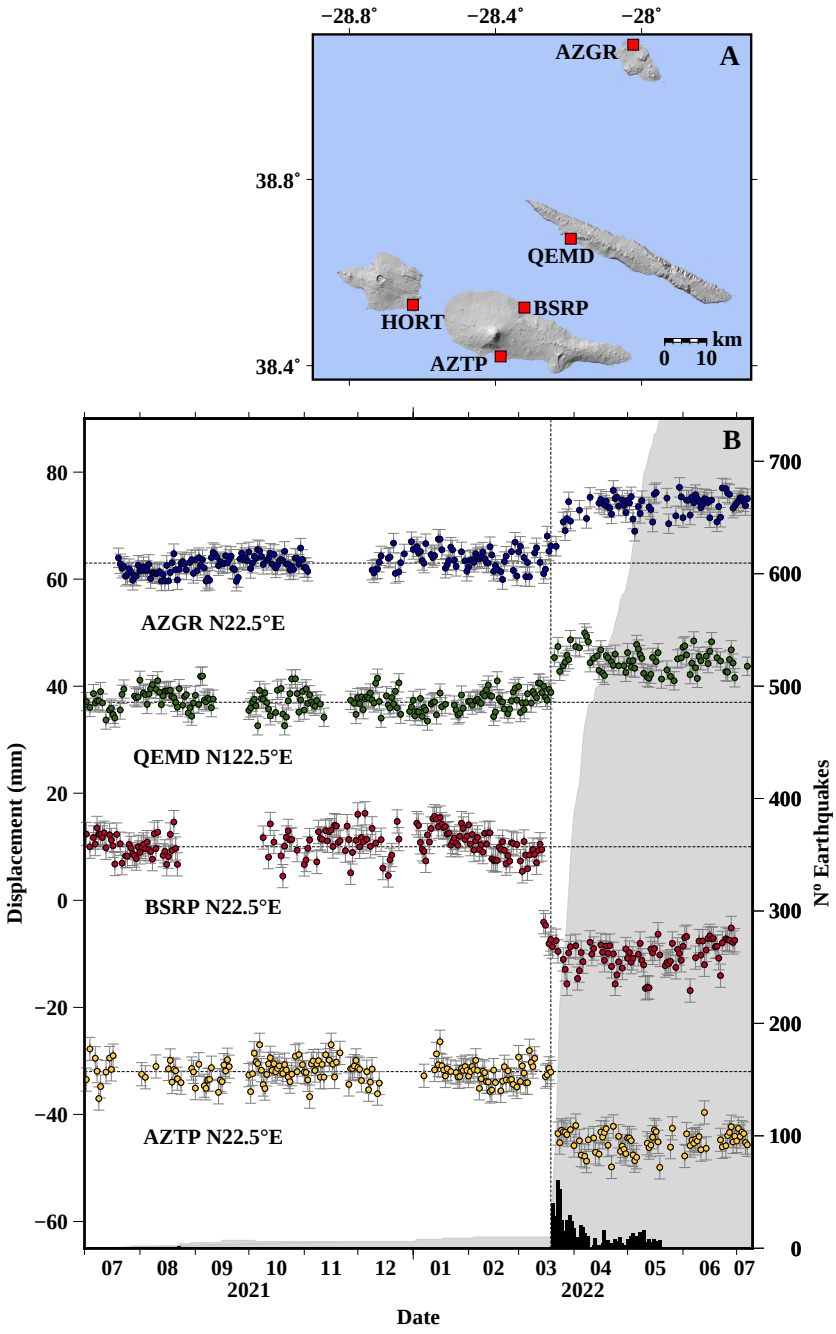

Figure 5.3: A - Location of the GNSS stations on Graciosa (AZGR), São Jorge (QEMD), Faial (HORT), and Pico (BSRP and AZTP) islands. B - Time series of the GNSS stations daily movement relative to predicted plate motion (D'Araújo et al., 2022), transformed onto the direction perpendicular to the dyke direction (N22.5°E) for stations AZGR, HORT, BSRP and AZTP, and parallel to the dyke direction (N112.5°E) for station QEMD. The times series are shifted from top to bottom to display the station movements from the north (AZGR) to the south (AZTP). The vertical dashed line represents 19 March. The vertical black bars are the daily number of the best-located earthquakes, and the grey area is the cumulative number of earthquakes.

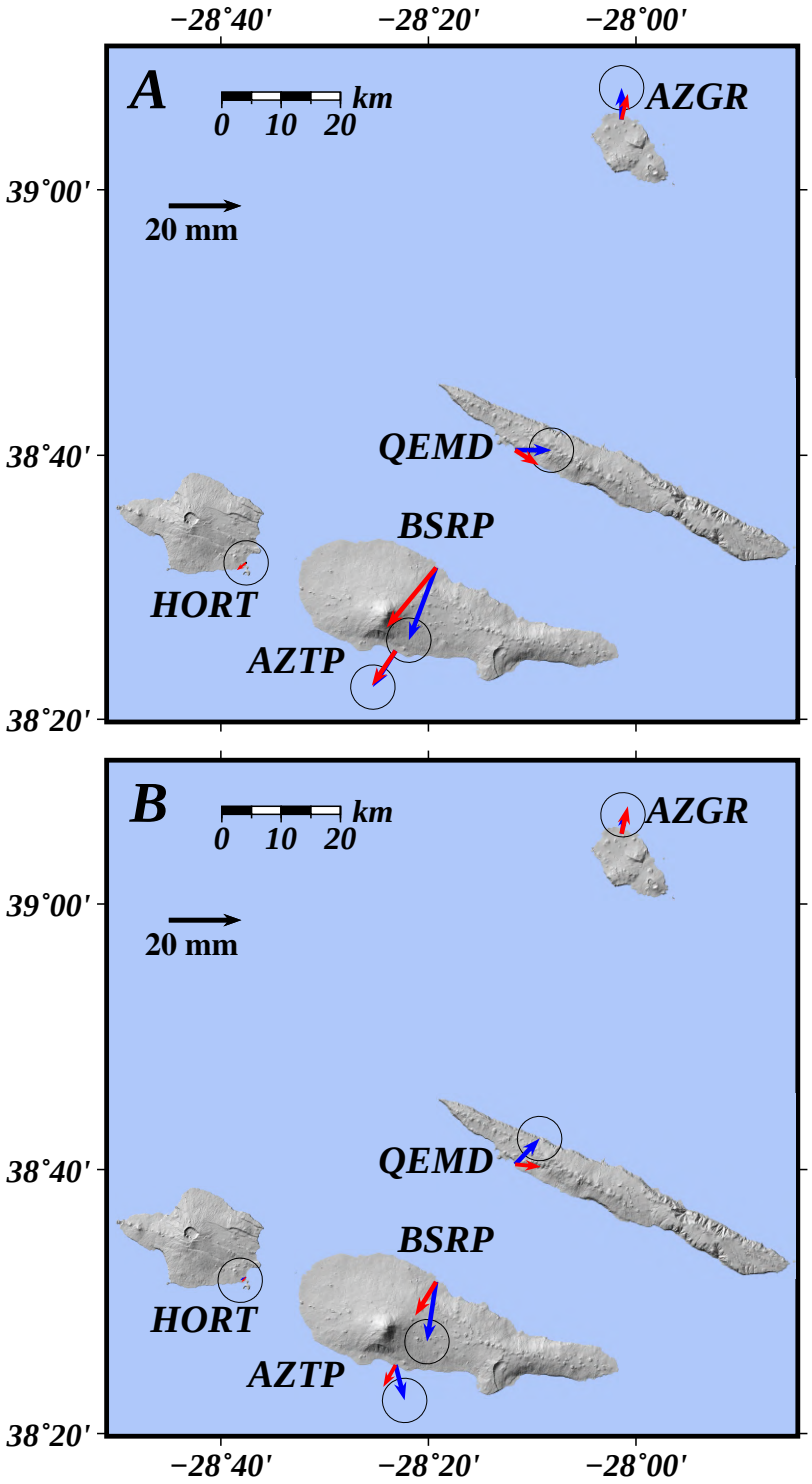

Figure 5.4: A - Horizontal velocity map of GNSS stations for the 19-20 March period. B - Horizontal velocity map of GNSS stations for the 20 March - 3 April period. Blue vectors are displacements observed and red vectors are displacements modeled.

5.3 InSAR

InSAR data was used to measure ground deformation at São Jorge with more spatial detail. The results were obtained in collaboration with researchers from Institute of Geophysics and Tectonics (University of Leeds). Despite covering two weeks, most deformation observed from InSAR dataset is from the initial 19-20 March activity.

The LOS deformation related with the 19-20 March activity (Figure 5.5), projected into vertical (plus N-S horizontal) and E-W horizontal components (see Methods), reveal uplift of up to 55 mm and a longitudinal horizontal deformation stretching through 60 mm in the northern part of São Jorge Island.

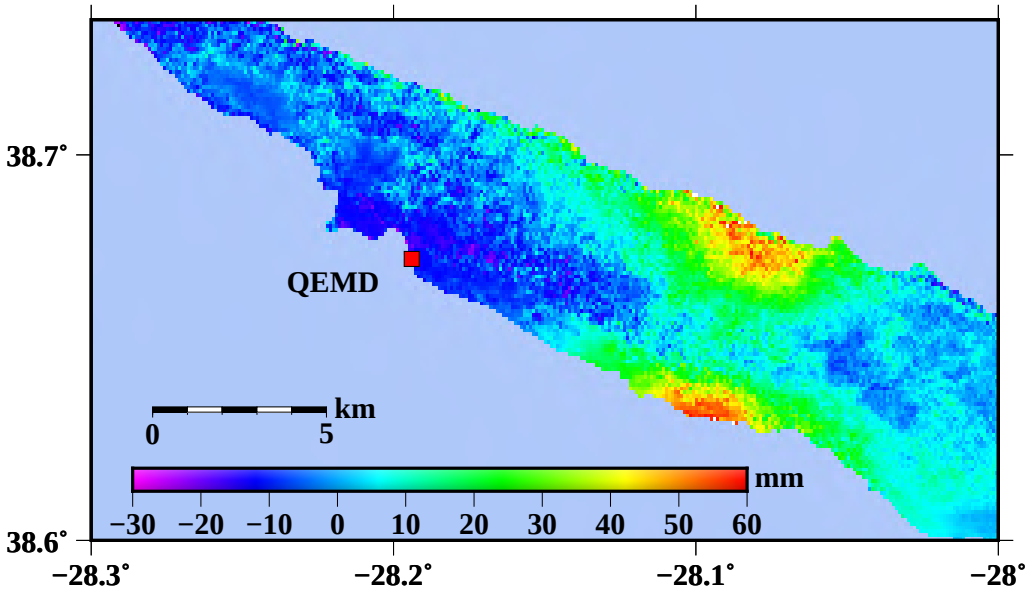

Figure 5.5: Deformation of the vertical (plus N-S horizontal) component retrieved from InSAR data analysis.

5.4 Modeling

The best fit results for the inversion of the 19-20 March deformation using a single opening rectangular dislocation (see Methods) were obtained for a near vertical 8 km long dyke placed at 3-10 km depth in the Manadas area with an opening of 0.5 m, indicating an intrusion of about $2.5 - 5 \times 10^7\ m^3$. The dyke location agrees well with the distribution of the seismic events. The second attempt using a single opening rectangular dislocation constrained with the location of seismic events in 19-20 March gives similar opening and volume estimates (see Figures C2, C3, and C4 in Appendix C).

The combined analysis of GNSS and InSAR data allows using a complex source model for inversion of the 19-20 March data (Figure 5.6). The model consists of two 8 km length segments with different orientations and depths, each comprising multiple smaller rectangular dislocation patches. The distribution of opening inferred from the modeling reveals the intrusion of magma on both dyke segments, each with a separate locus of maximum opening, namely a maximum opening of 1.7 m at 4-6 km depth in the eastern segment and a maximum opening of 1.8 m at 7-9 km depth in the western segment.

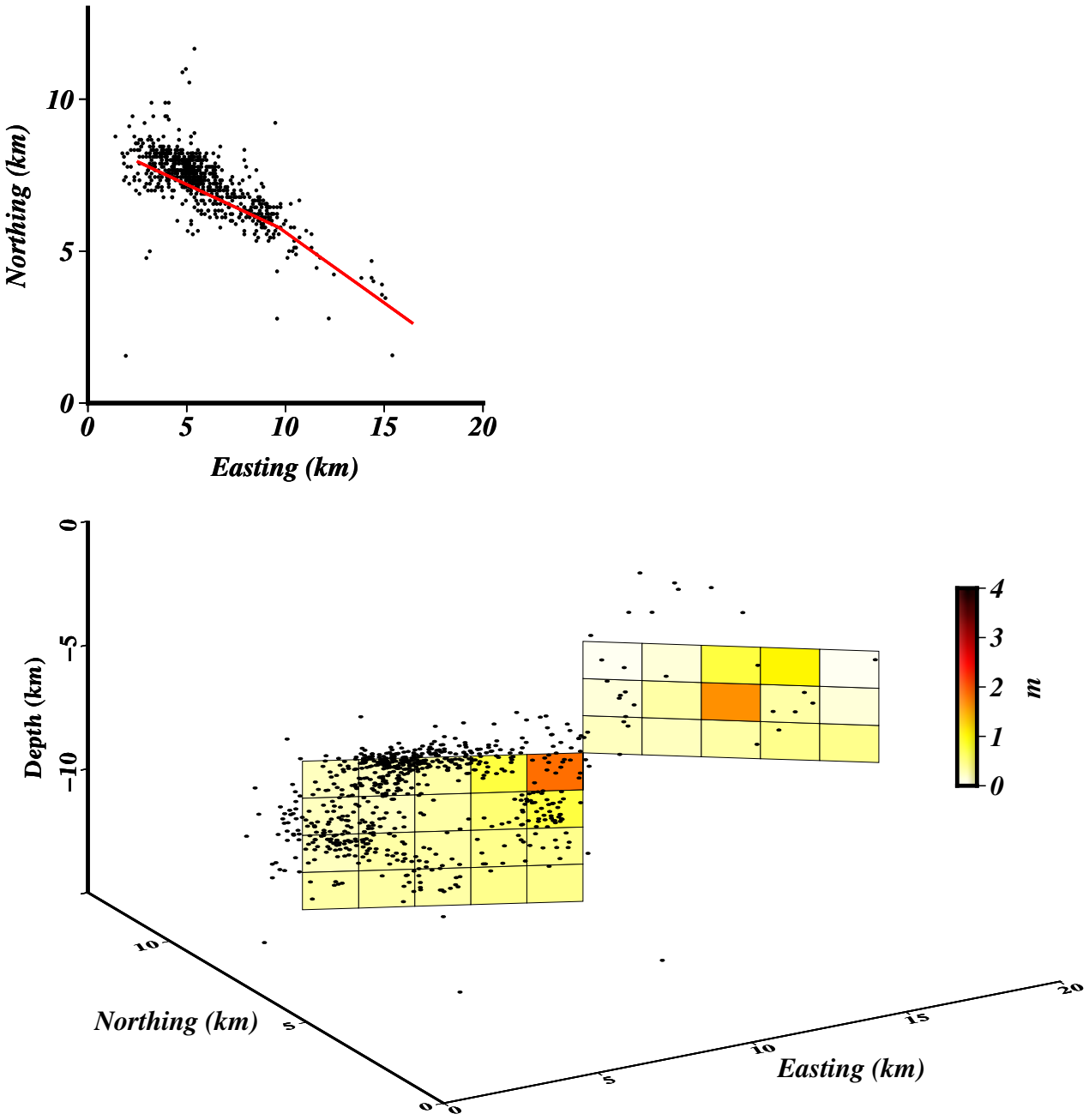

Figure 5.6: Upper - Horizontal profile of the segmented dyke for 19-20 March (red line). Lower - Best fit modeling results of opening along the two segmented dyke for 19-20 March. Black dots represent the best-located earthquakes during the first two months of activity.

5.5 Discussion

The geodetic and seismic data is consistent with a dyke intrusion along the central area of São Jorge, where previous historical sub-aerial eruptions occurred, with the seismicity lying within the axial fault zone orientation. The existence of two dyke segments with slightly different orientations is inferred from the seismicity, with an eastern segment fitting the initial seismic activity on 19 March and a western segment fitting the activity afterward. Far-field GNSS stations located north on Graciosa Island and south on Pico Island, perpendicular to the axial dyke orientation, show horizontal displacements away from São Jorge Island consistent with a dyke intrusion.

During the activity, seismicity therefore propagated westward, with the emplacement of a two-segmented dyke system. Analysis of the temporal distribution of seismic clusters suggests that it propagated faster in the eastern dyke segment and slower in the western segment. The eastern segment was the first to start propagating, as revealed by a cluster of M_L 2.4–2.9 earthquakes on 19 March between 18:19 and 18:24, located at the bottom eastern part of the dyke segment at depths of 4.8-6.6 km. The dyke propagated laterally to the west about 4 km, as revealed by a cluster of M_L 2.2-2.7 earthquakes between 18:55 and 19:00, located at the bottom western part of the segment at depths of 4.3-5.2 km. This can be taken as an indication of a dyke propagation speed of about 1.8 m/s at the start of the intrusion in the eastern shallow dyke segment.

After the initial dyke propagation and eventual relaxation of stored tectonic stress at shallow levels, the next most energetically favorable location for dyke propagation appears to have been deeper. Seismicity migrated to the west and deeper levels and slowly decayed

in frequency and magnitude. In addition, the speed of the dyke propagation decreased. Initiation of the western dyke propagation occurred between 19:04 and 19:52 with an inferred rate of about 0.5 m/s rate, as revealed by a cluster of M_L 2.2-3.3 earthquakes at depths of 5.9-6.6 km in the area connecting the two dyke segments. The slower rate of dyke propagation and the strong M_L 3.3 earthquake can be explained by the structural discontinuity of the area where the Picos and Pico do Carvão fault zones meet, which likely increased the resistance to magma flow. After that, seismicity continued migrating further west to deeper levels at a rate of 0.2 m/s, as revealed from a cluster of M_L 1.7-2.4 earthquakes between 23:17 and 00:37, located at the top central part of the western segment at depths of 7.5-7.7 km.

While the propagation rates calculated for the western dyke segment are consistent with reported values of 0.2-0.8 m/s for non-erupting dykes, e.g. at the Afar region (Belachew et al., 2011), the initial rate calculated for the eastern dyke segment is higher. There were intermittent shallower earthquakes located from the surface to 2 km depth that likely originated from faulting due to the accumulated strain released from the pressure of the dyke emplacement below, as indicated for episodic dyking episodes in other regions (Wright et al., 2012).

The analysis of the geodetic data shows that there were at least two main stages of deformation. The first period was a rapid episode that lasted less than 24 hours between 19 and 20 March, with a higher deformation rate. During this period, the station AZGR located on Graciosa Island, moved to the north, while stations BSRP and AZTP, located on Pico Island, moved to the south (see Figure 5.4A). On the other hand, the station QEMD located on São Jorge moved towards the island's center. In addition, offsets from InSAR data analysis for the 19-20 March period are consistent with uplift and opening on the lateral

areas off-axis, perpendicular to the dyke segments in the central area of São Jorge Island.

Seismicity concentrates around the locus of maximum opening in the eastern segment stopped after 19 March, indicating that magma injection may have halted there. On the other hand, seismicity continued in the western segment after 19 March, indicating that injection of magma may have continued there. After 20 March, seismicity decreased in frequency and magnitude, and opening continued to the west to deeper levels, suggesting a slower, more gradual injection of magma in that period.

The second period of deformation was an episode with a more gradual and lower deformation rate that occurred in the two weeks following the 19-20 March episode. During this period of 15 days, a maximum horizontal displacement of 0.9 mm/day was recorded on the BSRP station (see Figure 5.4B). InSAR data show no significant LOS changes at São Jorge Island during this period. A simple modeling source is used during the inversion of the data for this period since only GNSS data is available. It is assumed that the opening and injection of magma only occurred at deeper levels in the western dyke segment after 20 March, as suggested by the lack of seismic activity in the eastern segment and lack of deformation at São Jorge Island from the InSAR data. A single rectangular dislocation is used with the dimension and location of the western dyke segment. The modeling results are consistent with an opening of 0.5 m in the western dyke between 19 March and 3 April.

The lack of seismic activity prior to the start of the activity suggests that magma was already present in the magmatic system. The most likely location of a magma reservoir is below the eastern dyke segment. Magma accumulation and crystallization have been suggested for previous eruptions, with the extrusion of more evolved magma in the initial stages of the 1580 and 1808 eruptions (Zanon & Viveiros, 2019). The lack of seismicity in

the area may relate to eventual ductile nature of the possible magma reservoir.

Initially, the most favorable location for magma intrusion was at shallow levels, likely due to triggered failure conditions between the magma body and the host rock. The end of activity in the shallow dyke segment may eventually be explained by the depressurization after the emplacement of the dyke to the west. The abrupt dyke propagation and injection of magma at shallow levels appears to have triggered the continuation of the dyke propagation to the west and to deeper levels. The dyke propagation to the west may reflect the least resistance pathway for magma, as the extension is accommodated across the existing main fault zones in the area.

The InSAR data allows a detailed coverage of the deformation in São Jorge, but the small size and shape of the island, which is very elongated and narrow, limits the spatial resolution. Far-field data points perpendicular to the dyke axis are essential for estimating the model parameters. It was found that using more distant GNSS stations is critical to measure the ground deformation in small adjacent islands, as subaereal land is limited in the area affected by the dyke intrusion.

6 Conclusions

Analysis of continuous GNSS data from the Azores shows the importance of estimating high precision velocities from long time series for accurately measuring oblique ultra-slow spreading in the region. The results show that Flores and Graciosa islands have displacements close to predicted North American and Eurasian motions, respectively. In contrast, São Miguel, Terceira, São Jorge, Faial, and Pico islands have displacements intermediate between predicted Eurasian and Nubian motions. The spreading in the Eurasian-Nubian plate boundary in the Azores occurs in a wide area between the Mid-Atlantic Ridge and southeast of São Miguel Island. The GNSS observations indicate that the inter-plate motion does not change gradually across the whole boundary. Rather, it appears to be focused in some areas, including the central area of São Miguel Island and between Faial-Pico ridge and Terceira Island. Modeling, using a freely sliding dislocation below a locking depth in a uniform elastic half-space, predicts a deep motion in the range of 2.3-2.5 mm yr^{-1} directed N(82.3-88.7)°E in the Central Group islands and on the São Miguel Island. This motion accounts for about half of the predicted Eurasian-Nubian relative plate motion. The results suggest that spreading in the Central Group islands is dominated by deep processes while in São Miguel Island is dominated by shallow processes. Due to unrest activity, transient deformation occurs at Fogo volcano, São Miguel Island. Local subsidence occurs on Terceira Island, explained by a continuous deflation source centered on the island.

Spreading at São Miguel Island is revealed in more detail from the velocities of episodic GNSS stations in the island relative to the predicted ITRF2014 plate motion model for the 2004-2016 period. The velocities show that the western and eastern parts of the island are

spreading apart at an average rate of 2.2 ± 0.5 mm yr^{-1} in the N(80.5)°E direction. As a result of spreading, strain accumulates in the central part of the island from the Fogo volcano to the Congro fissure zone, and is eventually released during unrest periods.

Analysis of GNSS and seismic data show that the central part of São Miguel Island was very active during the study period of 2004-2019, with three periods of inflation in 2004-2006, 2011-2013, and 2018-2019, and a deflation period in 2013-2016. The best-fit modeled sources are located east of the Fogo volcano caldera at depths of 3.2-4.4 km. Best-fit point-pressure source models indicate volume increases in the range of $8.8 - 10.4 \times 10^6\ m^3$ in 2004-2006, $1.1 - 3.8 \times 10^6\ m^3$ in 2011-2013 and $3.8 - 5.4 \times 10^6\ m^3$ in 2018-2019, and volume decrease in the range of $3.1 - 4.4 \times 10^6\ m^3$ in 2013-2016. The results suggest that mixed magmatic-hydrothermal processes may explain the activity in the area during the study period.

The 2004–2006 best-fit source, located in an important fault system 3 km east of Fogo caldera, and the lack of significant subsidence after the 2004–2006 inflation can be explained by the permanence of a newly intruded magma body below Fogo volcano.

The overlap of the locations of the 2011–2013, 2013–2016, and 2018-2019 best-fit sources (95% confidence) in an area comprising the eastern and northeastern rim of Fogo caldera suggests that the volume changes during these three periods of deformation are related to the same body at depth. The location of the three best-fit sources, in an area with a low-density minimum below Fogo caldera (Camacho et al., 1997), suggests that the activity during these periods may have been in the magma chamber or hydrothermal system of the Fogo volcano. The inflation-deflation reversal from 2011–2013 to 2013–2016 may relate to differences in the nature of the 2011–2013 pressure increase compared with the 2004–2006 episode, such as higher content of gas and differences in the rock medium surrounding the center of inflation,

such as higher permeability. The 2013–2016 deflation can be explained by a similar process as described by J. Okada et al. (2015), of lateral diffusion of fluids percolating through existing fissures re-activated from local spreading and previous volcanic unrest in 2004–2006 and 2011–2013.

Results from GNSS and InSAR show that a shallow dyke intrusion occurred at São Jorge Island started in 19 March 2022, with magma reaching almost the surface in a few hours with no precursory signals. The geodetic and seismic data is consistent with a dyke intrusion along the central area of São Jorge, where previous historical sub-aerial eruptions occurred. Modeling results show a maximum opening in the range of 1.7-1.8 m at 4-9 km depth in the 19-20 March period. Elastic strain accumulated from regional spreading was released by a sudden, episodic dyking event. The lack of seismic activity prior to the start of the activity suggests that magma was already present in the Manadas volcanic system at São Jorge Island. Initially, the most favorable location for dyke intrusion was at shallow levels. After that, dyke propagation continued to the west and to deeper levels. The dyke propagation to the west may reflect the least resistance pathway for magma, as the extension is accommodated across the existing main fault zones in the area. The InSAR data allows a detailed coverage of the deformation in São Jorge, but the small size and shape of the island limit the spatial resolution. The analysis of the geodetic data from São Jorge Island in 2022 shows that using far-field data points from GNSS stations perpendicular to the dyke axis is critical to measure the ground deformation in small adjacent islands.

7 Appendix A

Here are presented auxiliary Tables from chapter Methods.

This includes information about continuous and episodic GNSS stations, results from FODITS program analysis, GNSS surveys, and predicted Eurasian-Nubian displacements from plate motion models.

Table A1: Location and Initial Date of Continuous GNSS Stations.

Station	Longitude (°)	Latitude (°)	Height (m)	Initial Date
AZGR	-28.023	39.088	91	2008-July
BSRP	-28.321	38.525	97	2018-August
BVF1	-25.446	37.717	114	2007-July
FLRS	-31.126	39.454	80	2008-April
FRNS	-25.000	37.769	275	2008-April
HORT	-28.626	38.531	67	2013-March
HTN1	-25.315	37.773	273	2006-February
NOV1	-27.149	38.776	156	2004-February
PCNG	-25.396	37.768	644	2009-January
PDEL	-25.663	37.748	111	2000-January
PIED	-28.032	38.414	72	2009-January
PTRP	-28.386	38.420	78	2010-May
QBN1	-25.146	37.835	204	2003-February
QEMD	-28.194	38.672	86	2012-November
RIB1	-25.499	37.837	117	2002-May
SRPC	-27.205	38.663	169	2003-February
TERC	-27.153	38.719	407	2008-September
VFDC	-25.436	37.715	103	2009-July

Table A2: Location and Initial Date of Episodic GNSS Stations.

Station	Longitude (°)	Latitude (°)	Height (m)	Initial Date
ARE1	-25.426	37.765	654	2004-September
ARE2	-25.319	37.743	529	2004-September
ARR1	-25.704	37.778	288	2004-September
BARR	-25.492	37.758	977	2004-September
BPCO	-25.507	37.786	332	2004-September
CALH	-25.493	37.805	239	2004-September
CAVE	-25.496	37.779	612	2004-September
CED1	-25.359	37.757	765	2004-September
CIN1	-25.487	37.839	224	2004-September
CMT1	-25.567	37.814	95	2004-September
COMT	-25.471	37.816	298	2004-September
COVA	-25.489	37.772	759	2004-September
CPR1	-25.722	37.844	460	2004-September
CRZ1	-25.440	37.751	741	2004-September
EGU1	-25.755	37.827	931	2004-September
ESC1	-25.834	37.870	394	2004-September
FOG3	-25.489	37.769	778	2004-September
FOG4	-25.505	37.766	781	2004-September
FRE1	-25.507	37.820	244	2004-September
FUR4	-25.372	37.793	566	2004-September

FUR5	-25.364	37.774	630	2004-September
GAF1	-25.318	37.790	655	2004-September
GAF2	-25.315	37.797	773	2004-September
GAR2	-25.360	37.736	378	2004-September
GAS2	-25.314	37.758	422	2004-September
GIE2	-25.606	37.787	234	2004-September
GIN1	-25.844	37.848	272	2004-September
GTE1	-25.495	37.774	703	2004-September
HMP1	-25.794	37.839	645	2004-September
KATA	-25.267	37.777	455	2004-September
LAG1	-25.297	37.822	489	2004-September
LAG2	-25.585	37.741	64	2004-September
LOF1	-25.460	37.776	624	2004-September
LOFA	-25.171	37.844	278	2004-September
LOM1	-25.350	37.828	326	2004-September
LPI1	-25.763	37.872	669	2004-September
MAA1	-25.414	37.733	321	2004-September
MAF1	-25.804	37.891	416	2004-September
MAR1	-25.658	37.740	59	2004-September
MCR1	-25.741	37.826	752	2004-September
MLF1	-25.481	37.761	635	2004-September
MLOB	-25.465	37.785	718	2004-September

MLV1	-25.813	37.872	482	2004-September
MOE2	-25.438	37.785	863	2005-August
MOE3	-25.429	37.791	766	2005-August
MOE4	-25.426	37.781	795	2005-August
MRH1	-25.736	37.870	468	2004-September
MRN1	-25.524	37.745	477	2004-September
MST2	-25.822	37.899	73	2004-September
MUL2	-25.704	37.813	372	2004-September
NOR2	-25.157	37.826	358	2004-September
NOR2	-25.218	37.750	469	2004-September
PBR1	-25.513	37.764	638	2004-September
PCA1	-25.739	37.822	871	2004-September
PCR2	-25.758	37.848	903	2004-September
PEN1	-25.644	37.807	200	2004-September
PF01	-25.426	37.807	411	2004-September
PGA1	-25.509	37.708	59	2004-September
PIMA	-25.402	37.796	634	2004-September
PIV1	-25.509	37.795	231	2004-September
PIV2	-25.506	37.800	231	2004-September
PIVA	-25.562	37.802	210	2004-September
PJFE	-25.527	37.760	532	2004-September
POC1	-25.308	37.737	469	2004-September

POSO	-25.149	37.800	427	2004-September
POV1	-25.574	37.778	242	2004-September
PPRA	-25.538	37.820	72	2004-September
PRO2	-25.644	37.781	256	2004-September
PVR1	-25.749	37.892	323	2004-September
QBP1	-25.233	37.746	243	2004-September
QUE1	-25.543	37.785	426	2004-September
REM1	-25.762	37.865	719	2004-September
RETO	-25.154	37.766	366	2004-September
RST1	-25.638	37.745	82	2004-September
S001	-25.271	37.756	427	2004-September
S002	-25.224	37.759	290	2004-September
S003	-25.222	37.778	415	2004-September
SALA	-25.287	37.789	835	2004-September
SAN1	-25.701	37.860	101	2004-September
SBAR	-25.524	37.801	177	2004-September
SCAV	-25.278	37.786	821	2004-September
SEB1	-25.256	37.797	986	2004-September
SET2	-25.807	37.843	585	2004-September
SET3	-25.782	37.892	363	2004-September
SOG1	-25.492	37.779	583	2004-September
SOG2	-25.490	37.782	545	2004-September

VELO	-25.460	37.784	722	2004-September
VGI1	-25.655	37.831	90	2004-September
VIG2	-25.764	37.790	379	2004-September
VTI1	-25.523	37.779	357	2004-September

Table A3: Equipment Changes in continuous GNSS Stations.

Station	Date	Receiver Type	Antenna Type	Heigh (m)
AZGR	2008/07/26	TRIMBLE NETR5	TRM55971.00 NONE	0.000
	2012/04/31	TRIMBLE NETR9	TRM55971.00 NONE	0.000
BVF1	2007/07/18	TRIMBLE NETRS	TRM29659.00 NONE	0.498
FLRS	2009/01/01	LEICA GRX1200GGPRO	LEIAT504GG NONE	0.498
FRNS	2008/04/16	LEICA GX1230GG	LEIAX1202GG NONE	0.498
HORT	2013/01/01	LEICA GX1230GG	LEIAR25 NONE	0.000
HTN1	2005/05/23	LEICA RS500	LEIAT504 NONE	0.861
	2006/02/15	TRIMBLE NETRS	TRM29659.00 NONE	0.571
	2007/07/18	LEICA GRX1200	LEIAT504 NONE	0.571
NOV1	2003/02/23	LEICA RS500	LEIAT504 LEIS	0.483
	2013/07/29	LEICA SR520	LEIAT504 LEIS	0.483
	2014/07/29	LEICA GR25	LEIAT504 LEIS	0.483
PCNG	2005/07/11	LEICA RS500	LEIAT504 NONE	0.485

	2012/08/01	LEICA GRX1200	LEIAT504 NONE	0.485
	2013/02/15	LEICA RS500	LEIAT504 NONE	0.485
	2014/07/23	LEICA GR25	LEIAT504 NONE	0.485
PDEL	2001/11/06	LEICA CRS1000	LEIAT504 NONE	0.000
	2002/12/19	LEICA RS500	LEIAT504 NONE	0.000
	2008/04/06	LEICA GRX1200GGPRO	LEIAT504GG NONE	0.000
PTRP	2010/05/19	LEICA GRX1200GGPRO	LEIAT504GG LEIS	0.000
QBN1	2003/02/21	TRIMBLE 5700	TRM29659.00 TCWD	0.485
QEMD	2012 11 01	LEICA GRX1200GGPRO	LEIAT504 LEIS	0.000
RCHA	2005/02/01	ASHTECH Z-X	ASH701975.01A NONE	0.932
	2005/12/14	TRIMBLE NETRS	TRM29659.00 NONE	0.932
RIB1	2002/05/07	LEICA RS500	LEIAT504 LEIS	0.485
	2015/06/12	LEICA GR25	LEIAT504 LEIS	0.485
SRPC	2003/02/25	LEICA RS500	LEIAT504 LEIS	0.485
	2014/10/29	LEICA GR25	LEIAT504 LEIS	0.485
TERC	2008/09/18	LEICA GRX1200GGPRO	LEIAT504GG LEIS	0.000

VFDC	2009/07/14	LEICA GRX1200+GNSS	LEIAX1203+GNSS	0.000
			NONE	

Table A4: Discontinuities of the continuous GNSS time series in East, North, and Up Components. [a] is unreported equipment change. [b] is possible influence from volcano deformation. [c] is global standard deviation.

Station	Date	Event	N(mm)	E(mm)	U(mm)	SD[c](mm)
AZGR	2009/05/30	*Equipment*[a]	2.3	2.6	8.1	0.3
	2013/11/17	*Equipment*[a]	1.0	-1.0	4.1	0.2
	2015/06/25	*Equipment*[a]	0.0	-1.5	13.4	0.2
*BVF*1	2011/11/20	*Deformation*	-5.7	-0.3	2.6	0.3
PDEL	2006/12/13	*Equipment*[a]	6.0	1.5	1.3	0.2
	2008/04/06	*Equipment*	2.3	-0.4	11.5	0.3
	2012/10/17	*Equipment*[a]	-4.3	-1.2	-3.6	0.2
PCNG	2007/01/10	*Deformation*	-1.7	-1.1	7.4	0.4
	2007/09/08	*Deformation*	-6.5	-5.3	-0.3	0.4
	2008/11/04	*Deformation*	6.4	1.7	2.3	0.4
	2014/07/23	*Equipment*[b]	1.6	-2.8	-6.1	0.4
RCHA	2005/12/14	*Equipment*[b]	-21.9	-4.2	1.7	0.7
	2006/11/12	*Equipment*[b]	-8.4	-6.1	6.0	0.5
	2011/10/03	*Deformation*	-5.3	-3.0	4.3	0.3
*RIB*1	2005/06/05	*Deformation*	10.7	-9.2	-7.8	0.5
	2011/09/28	*Deformation*	5.1	-3.1	0.9	0.3
	2015/07/08	*Deformation*	-4.1	3.0	-3.2	0.2
SRPC	2013/01/24	*Equipment*[a]	-0.3	-5.0	-0.6	0.3

$HTN1$	2006/02/15	$Equipment$	-5.1	10.2	296.9	0.9
$AZGR$	2009/05/30	$Equipment^a$	2.3	2.6	8.1	0.3
$AZGR$	2009/05/30	$Equipment^a$	2.3	2.6	8.1	0.3

Table A5: Annual Amplitudes and Phases of the continuous GNSS time series in East, North, and Up Components

	Amplitude (mm)			Phase (°)		
Station	N	E	U	N	E	U
AZGR	1.5	0.7	1.3	157.6	20.8	-158.6
*BVF*1	1.3	0.7	1.2	170.1	16.5	-177.7
FLRS	1.3	1.9	2.0	157.5	-28.5	-67.9
FRNS	1.6	0.8	1.8	168.3	-14.9	179.2
PDEL	1.6	0.8	2.1	158.2	-18.4	179.6
PIED	1.8	0.9	0.6	153.4	-9.5	-94.9
PCNG	1.6	1.0	0.9	138.1	21.8	-150.8
PTRP	1.8	0.8	1.9	135.9	47.4	147.1
*QBN*1	1.6	1.0	1.3	151.2	17.8	-169.9
RCHA	1.8	0.7	1.0	160.4	48.5	146.9
*RIB*1	1.2	0.9	1.2	159.0	17.9	167.2
SRPC	1.7	0.7	1.9	141.8	63.5	166.7
TERC	1.9	0.9	1.5	137.1	-19.1	-99.5
VFDC	1.7	0.9	0.5	156.4	38.4	176.0

Table A6: Velocity Changes of the continuous GNSS Stations in East, North, and Up Components

		Velocity (mm yr^{-1})			
Station	Date	North	East	Up	SD [c]
PDEL	2008-01-05	0.4	1.1	-0.3	0.1
*BVF*1	2013-08-24	6.9	-0.9	-3.5	0.2
FRNS	2012-08-31	0.6	-2.8	-2.8	0.2
PCNG	2014-09-08	0.5	-7.5	-6.3	0.2
RCHA	2007-12-22	6.6	5.1	-4.3	0.3
RCHA	2013-10-19	6.0	1.8	-1.9	0.2
*RIB*1	2006-12-22	-4.3	3.1	-2.9	0.2
*RIB*1	2014-09-30	-4.6	3.1	-3.0	0.2
SRPC	2008-02-23	0.0	0.5	-0.3	0.1
VFDC	2013-08-18	9.2	-1.5	-2.9	0.2

[c] Global Standard Deviation.

Table A7: Date interval of episodic GNSS campaign surveys in São Miguel Island

Campaign	Initial Date	Final Date
2004	2004-September-06	2004-September-30
2005	2005-July-11	2005-August-06
2006	2006-September-04	2006-September-23
2007	2007-September-03	2007-September-18
2008	2008-September-03	2008-September-21
2009	2009-August-18	2009-September-04
2010	2010-September-02	2010-September-20
2011	2011-August-02	2011-September-12
2012	2012-July-28	2012-August-26
2013	2013-August-19	2013-September-17
2014	2014-August-23	2014-September-20
2015	2015-August-07	2015-August-14
2016	2016-July-30	2016-August-20
2018	2018-July-04	2018-July-19
2019	2019-August-05	2019-August-22

Table A8: Eurasian-Nubian Plate Motion for Plate Motion Models ITRF2014, GEODVEL2010 and MORVEL2010

	Full Plate Velocities (mm yr^{-1})			
Model	East	North	Speed	Azimuth (°)
$ITRF2014$	$4.8^{+0.1}_{-0.1}$	$0.5^{+0.3}_{-0.4}$	$4.7^{+0.1}_{-0.0}$	$88.0^{+0.7}_{-3.8}$
$GEODVEL$	$4.8^{+0.1}_{-0.0}$	$0.5^{+0.3}_{-0.1}$	$4.8^{+0.1}_{-0.0}$	$83.5^{+0.7}_{-3.9}$
$MORVEL$	$4.0^{+0.3}_{-0.0}$	$1.2^{+0.7}_{-0.1}$	$4.2^{+0.4}_{-0.0}$	$72.7^{+1.7}_{-8.0}$

Plate motion is calculated at the average location of all continuous GNSS stations located to east of MAR (-26.556°E 38.187°N).

8 Appendix B

Here are included auxiliary figures from chapter São Miguel Volcano Deformation.

This includes histograms showing the posterior density functions for source parameters of 2004-2006, 2011-2013, 2013-2016, and 2018-2019 best fit models.

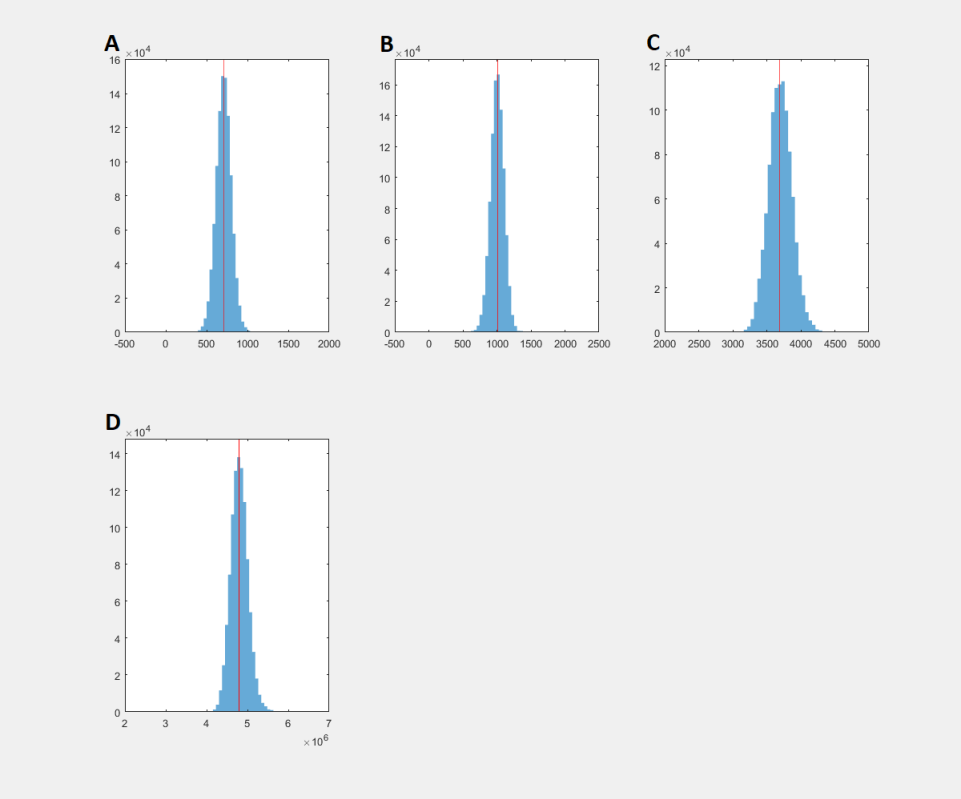

Figure B1: Histograms showing the posterior density functions for all source parameters of 2004-2006 best fit point-pressure model (blue bars) A - east local coordinate (m), B - north local coordinate (m), C - depth (m), and D - volume change (m^3). Red lines are the optimal values of the parameters.

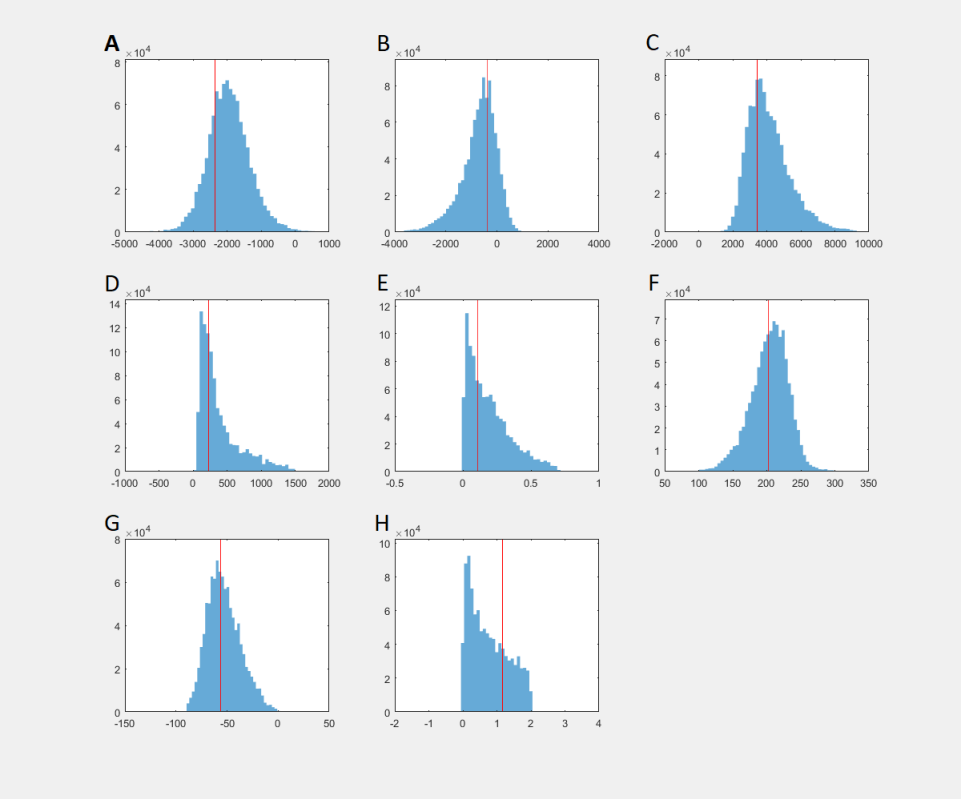

Figure B2: Histograms showing the posterior density functions for all source parameters of 2011-2013 best fit prolate spheroid model (blue bars) A - east local coordinate (m), B - north local coordinate (m), C - depth (m), D - length of major semi-axis (m), E - dimensionless aspect ratio between minor and major semi-axes, F - strike angle of major semi-axis with respect to north (°), G - inclination angle of major semi-axis with respect to horizontal (°), and H - dimensionless excess pressure (pressure change/shear modulus). Red lines are the optimal values of the parameters.

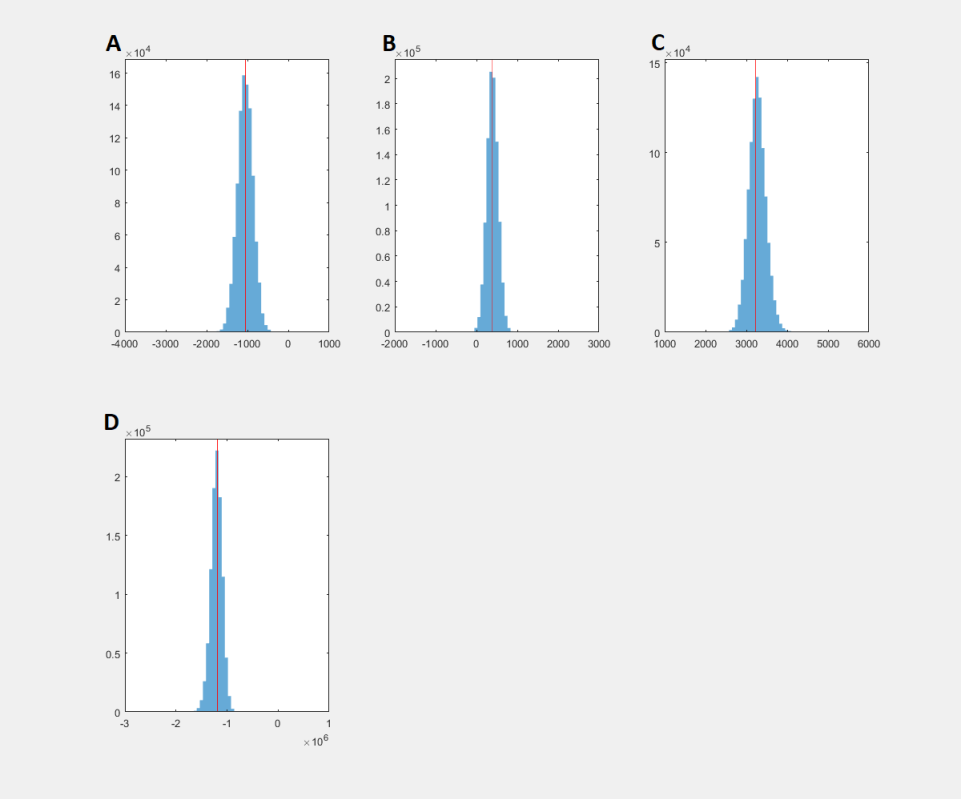

Figure B3: Histograms showing the posterior density functions for all source parameters of 2013-2016 best fit point-pressure model (blue bars) A - east local coordinate (m), B - north local coordinate (m), C - depth (m), and D - volume change (m^3). Red lines are the optimal values of the parameters.

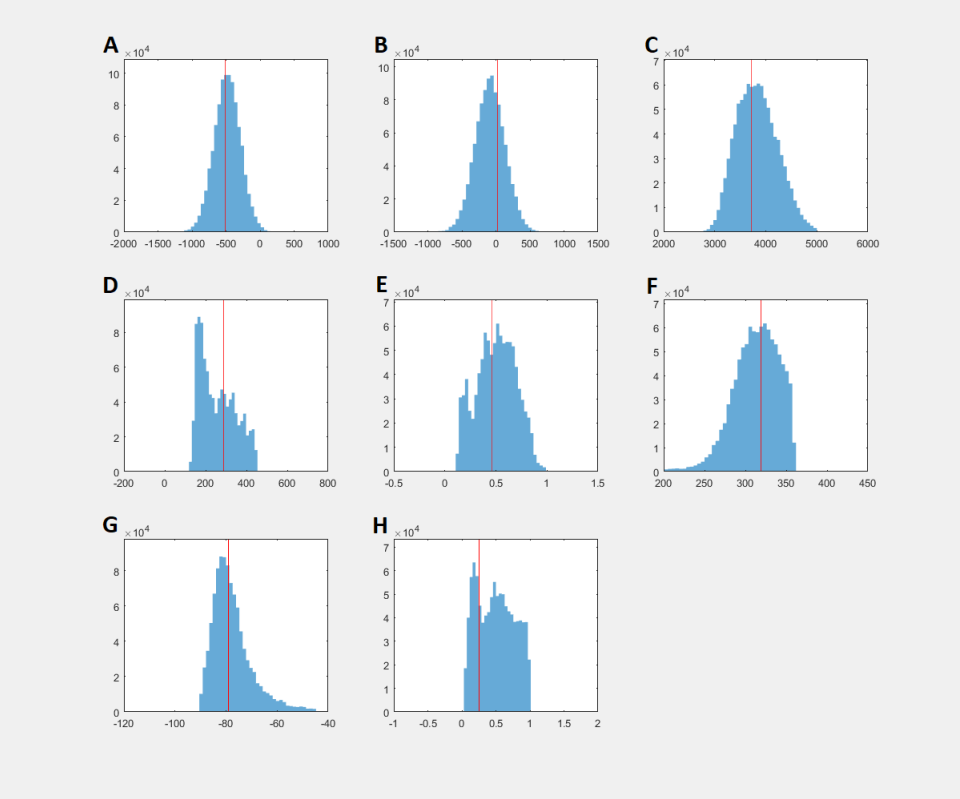

Figure B4: Histograms showing the posterior density functions for all source parameters of 2018-2019 best fit prolate spheroid model (blue bars) A - east local coordinate (m), B - north local coordinate (m), C - depth (m), D - length of major semi-axis (m), E - dimensionless aspect ratio between minor and major semi-axes, F - strike angle of major semi-axis with respect to north (°), G - inclination angle of major semi-axis with respect to horizontal (°), and H - dimensionless excess pressure (pressure change/shear modulus). Red lines are the optimal values of the parameters.

9 Appendix C

Here are included auxiliary figures from chapter São Jorge Volcano Deformation.

This includes LOS displacement of São Jorge Island and best-fit results from modeling using a single opening rectangular dislocation source.

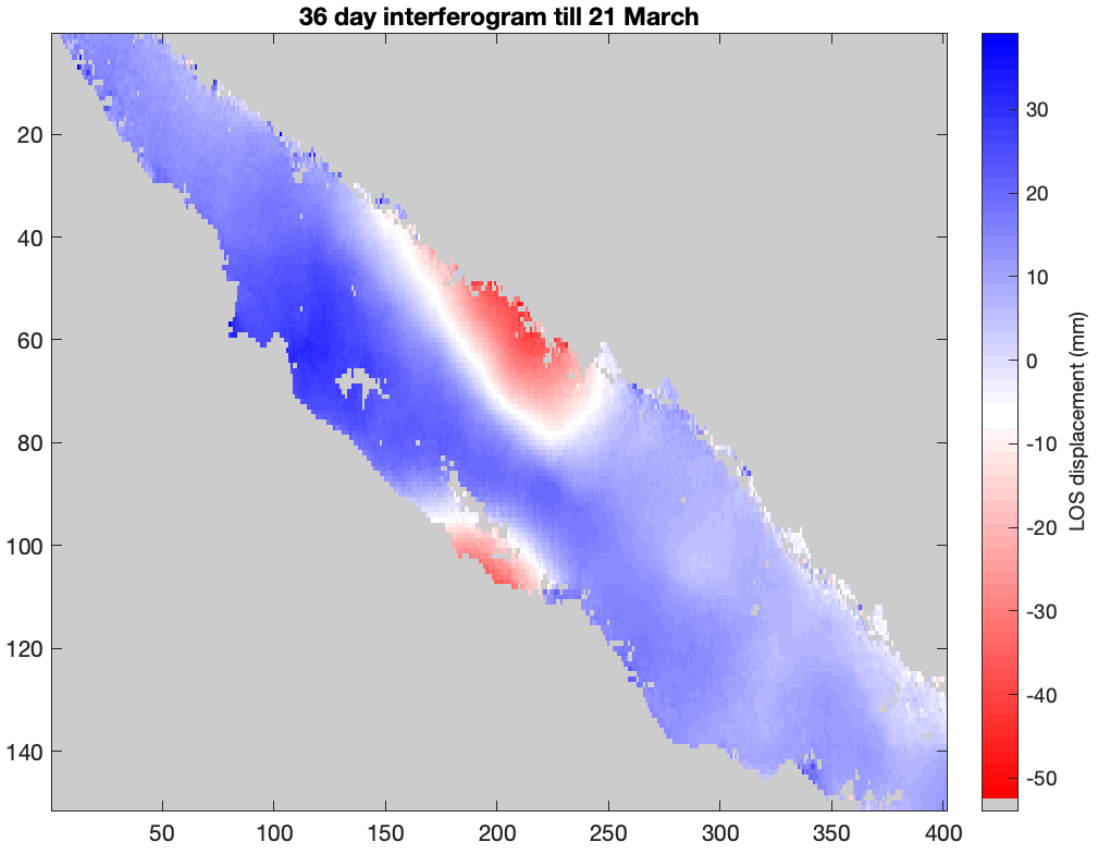

Figure C1: LOS displacement of São Jorge from 36 day interferogram (13 February 2022 - 21 March 2022)

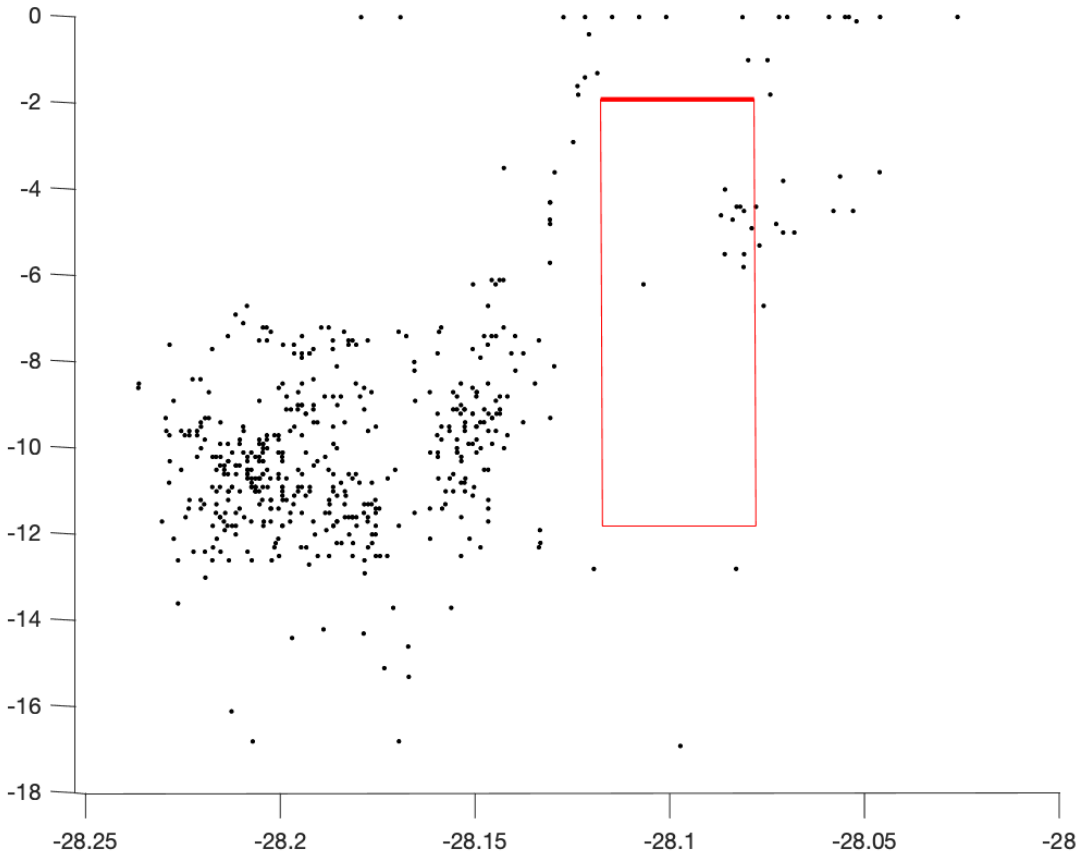

Figure C2: Vertical-Strike profile of best-fit model of São Jorge 19-20 March deformation using a single opening rectangular dislocation source constrained from location of seismic events.

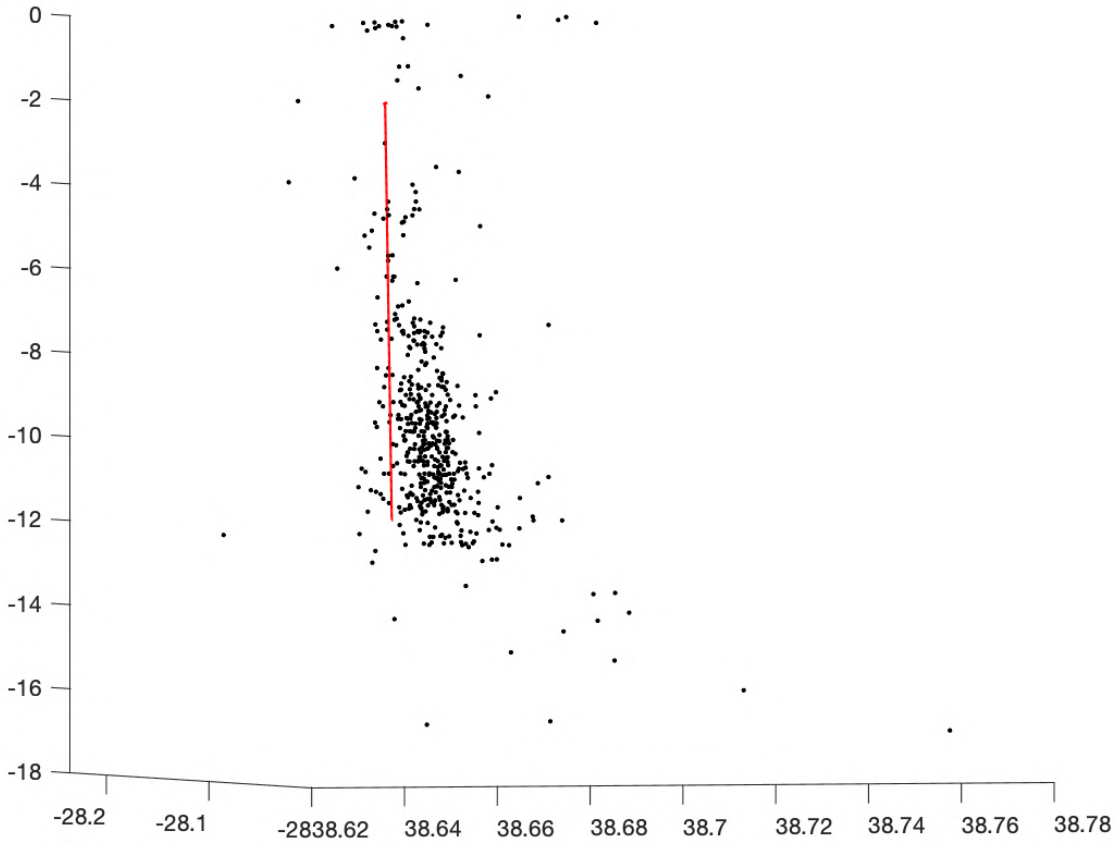

Figure C3: Vertical-Side profile of best-fit model of São Jorge 19-20 March deformation using a single opening rectangular dislocation source constrained from location of seismic events.

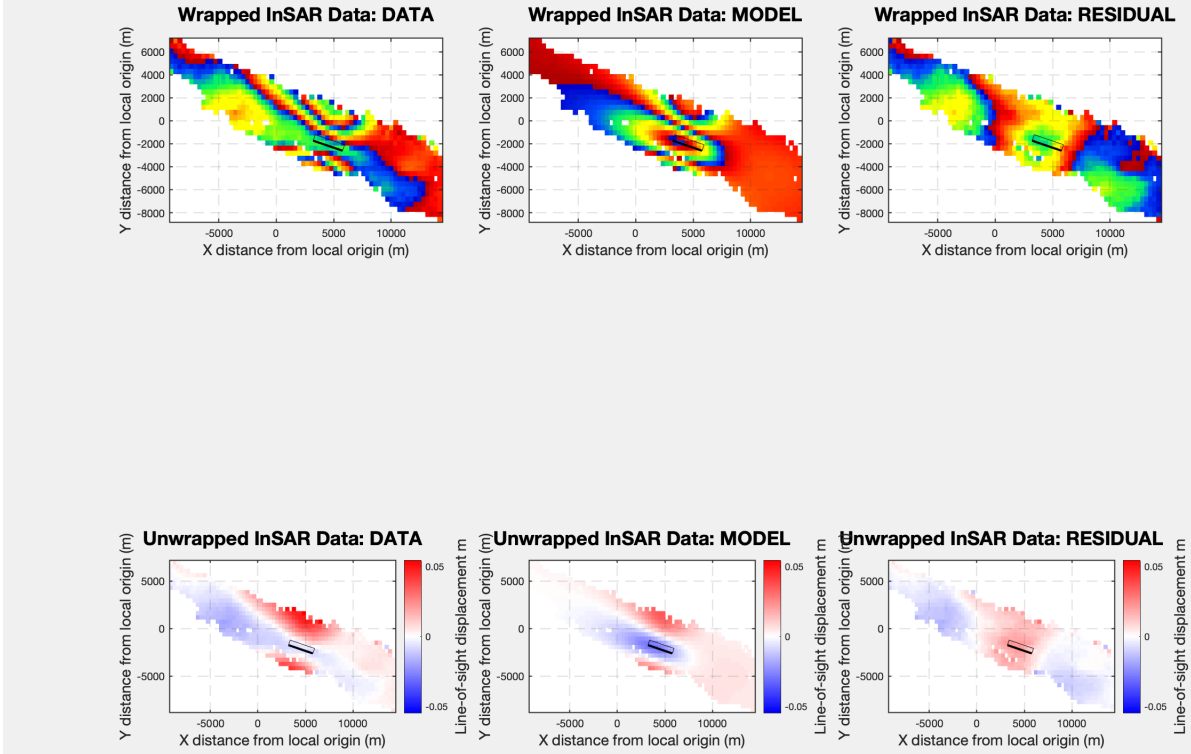

Figure C4: Results of modeling the São Jorge 19-20 March deformation using a single opening rectangular dislocation source constrained from location of seismic events.

10 References

Altamimi, Z., Métivier, L., Rebischung, P., Rouby, H., & Collilieux, X. (2017). Itrf2014 plate motion model. *Geophysical Journal International*, *209*(3), 1906–1912. doi: 10.1093/gji/ggx136

Altamimi, Z., Rebischung, P., Métivier, L., & Collilieux, X. (2016). ITRF2014: A new release of the International Terrestrial Reference Frame modeling nonlinear station motions. *Journal of Geophysical Research: Solid Earth*, *121*(8), 6109–6131.

Argus, D. F., Gordon, R. G., Heflin, M. B., Ma, C., Eanes, R. J., Willis, P., ... Owen, S. E. (2010). The angular velocities of the plates and the velocity of Earth's centre from space geodesy. *Geophysical Journal International*, *180*(3), 913–960. doi: 10.1111/j.1365-246X.2009.04463.x

Árnadóttir, T., Jiang, W., Feigl, K. L., Geirsson, H., & Sturkell, E. (2006). Kinematic models of plate boundary deformation in southwest Iceland derived from GPS observations. *Journal of Geophysical Research: Solid Earth*, *111*(B7). doi: 10.1029/2005JB003907

Bagnardi, M., & Hooper, A. (2018). Inversion of surface deformation data for rapid estimates of source parameters and uncertainties: A Bayesian approach. *Geochemistry, Geophysics, Geosystems*, *19*(7), 2194–2211. doi: 10.1029/2018GC007585

Battaglia, M., Cervelli, P. F., & Murray, J. R. (2013). dMODELS: A MATLAB software package for modeling crustal deformation near active faults and volcanic centers. *Journal of Volcanology and Geothermal Research*, *254*, 1–4. doi: /10.1016/j.jvolgeores.2012.12.018

Battaglia, M., & Hill, D. (2009). Analytical modeling of gravity changes and crustal defor-

mation at volcanoes: The Long Valley caldera, California, case study. *Tectonophysics*, *471*(1-2), 45–57. doi: 10.1016/j.tecto.2008.09.040

Battaglia, M., Troise, C., Obrizzo, F., Pingue, F., & De Natale, G. (2006). Evidence for fluid migration as the source of deformation at Campi Flegrei caldera (Italy). *Geophysical Research Letters*, *33*(1). doi: 10.1029/2005GL024904

Becker, J., Sandwell, D., Smith, W., Braud, J., Binder, B., Depner, J., ... others (2009). Global bathymetry and elevation data at 30 arc seconds resolution: SRTM30_PLUS. *Marine Geodesy*, *32*(4), 355–371. doi: 10.1080/01490410903297766

Beier, C., Haase, K. M., Abouchami, W., Krienitz, M.-S., & Hauff, F. (2008). Magma genesis by rifting of oceanic lithosphere above anomalous mantle: Terceira Rift, Azores. *Geochemistry, Geophysics, Geosystems*, *9*(12).

Belachew, M., Ebinger, C., Coté, D., Keir, D., Rowland, J., Hammond, J. O., & Ayele, A. (2011). Comparison of dike intrusions in an incipient seafloor-spreading segment in Afar, Ethiopia: Seismicity perspectives. *Journal of Geophysical Research: Solid Earth*, *116*(B6). doi: 10.1029/2010JB007908

Bezzeghoud, M., Adam, C., Buforn, E., Borges, J. F., & Caldeira, B. (2014). Seismicity along the Azores-Gibraltar region and global plate kinematics. *Journal of Seismology*, *18*(2), 205–220. doi: 10.1007/s10950-013-9416-x

Böhm, J., Niell, A., Tregoning, P., & Schuh, H. (2006). Global Mapping Function (GMF): A new empirical mapping function based on numerical weather model data. *Geophysical Research Letters*, *33*(7). doi: 10.1029/2005GL025546

Borges, J., Bezzeghoud, M., Buforn, E., Pro, C., & Fitas, A. (2007). The 1980, 1997 and 1998 Azores earthquakes and some seismo-tectonic implications. *Tectonophysics*, *435*(1-4),

37–54. doi: 10.1144/M44.4

Buforn, E., Udias, A., & Colombas, M. (1988). Seismicity, source mechanisms and tectonics of the Azores-Gibraltar plate boundary. *Tectonophysics*, *152*(1-2), 89–118. doi: 10.1016/0040-1951(88)90031-5

Camacho, A., Montesinos, F., & Vieira, R. (1997). A three-dimensional gravity inversion applied to São Miguel Island (Azores). *Journal of Geophysical Research: Solid Earth*, *102*(B4), 7717–7730. doi: 10.1029/96JB03667

Cannat, M., Sauter, D., Lavier, L., Bickert, M., Momoh, E., & Leroy, S. (2019). On spreading modes and magma supply at slow and ultraslow mid-ocean ridges. *Earth and Planetary Science Letters*, *519*, 223–233. doi: 10.1016/j.epsl.2019.05.012

Carmo, R., Madeira, J., Ferreira, T., Queiroz, G., & Hipólito, A. (2015). Volcano-tectonic structures of São Miguel Island, Azores. *Geological Society, London, Memoirs*, *44*(1), 65–86. doi: 10.1144/M44.6

Carvalho, M., Forjaz, V., & Almeida, C. (2006). Chemical composition of deep hydrothermal fluids in the Ribeira Grande geothermal field (São Miguel, Azores). *Journal of Volcanology and Geothermal Research*, *156*(1-2), 116–134. doi: 10.1016/j.jvolgeores.2006.03.015

CIVISA. (2022). *Centro de Informação e Vigilância Sismovulcânica dos Açores.* `http://www.ivar.{A}zores.gov.pt`. (Accessed: 2022-10-11)

Cochran, J. R. (2008). Seamount volcanism along the Gakkel Ridge, Arctic Ocean. *Geophysical Journal International*, *174*(3), 1153–1173. doi: 10.1111/j.1365-246X.2008.03860.x

Cole, P., Guest, J., Queiroz, G., Wallenstein, N., Pacheco, J., Gaspar, J., ... Duncan, A. (1999). Styles of volcanism and volcanic hazards on Furnas volcano, São Miguel,

Azores. *Journal of Volcanology and Geothermal Research*, *92*(1-2), 39–53. doi: 10.1016/S0377-0273(99)00066-9

Croasdale, R., Walker, G. P. L., & Booth, B. (1978). A quantitative study of five thousand years of volcanism on São Miguel, Azores. *Philosophical Transactions of the Royal Society of London. Series A, Mathematical and Physical Sciences*, *288*(1352), 271–319. doi: 10.1098/rsta.1978.0018

Cusano, P., Petrosino, S., & Saccorotti, G. (2008). Hydrothermal origin for sustained long-period (LP) activity at Campi Flegrei volcanic complex, Italy. *Journal of Volcanology and Geothermal Research*, *177*(4), 1035–1044. doi: 10.1016/j.jvolgeores.2008.07.019

Dach, R., & Walser, P. (2015). Bernese GNSS software version 5.2 [Computer software manual]. Citeseer. doi: 10.1002/2016JB013098

D'Araújo, J., Sigmundsson, F., Okada, J., Ferreira, T., Lorenzo, M., & Silva, R. (2022). Plate boundary deformation and volcano unrest at the Azores Triple Junction determined from continuous GPS measurements, 2002-2017. *Journal of Geophysical Research: Solid Earth*, *127*(1). doi: 10.1029/2021JB023007

DeGrandpre, K., Wang, T., Lu, Z., & Freymueller, J. T. (2017). Episodic inflation and complex surface deformation of Akutan volcano, Alaska revealed from GPS time-series. *Journal of Volcanology and Geothermal Research*, *347*, 337–359. doi: 10.1016/j.jvolgeores.2017.10.003

DeMets, C., Gordon, R. G., & Argus, D. F. (2010). Geologically current plate motions. *Geophysical Journal International*, *181*(1), 1–80. doi: 10.1111/j.1365-246X.2009.04491.x

De Natale, G., Pingue, F., Allard, P., & Zollo, A. (1991). Geophysical and geochemical modelling of the 1982–1984 unrest phenomena at Campi Flegrei caldera (southern Italy).

Journal of Volcanology and Geothermal Research, *48*(1-2), 199–222. doi: 10.1016/0377-0273(91)90043-Y

Di Vito, M. A., Acocella, V., Aiello, G., Barra, D., Battaglia, M., Carandente, A., ... others (2016). Magma transfer at Campi Flegrei caldera (Italy) before the 1538 AD eruption. *Scientific reports*, *6*(1), 1–9. doi: 10.1038/srep32245

Drouin, V., Heki, K., Sigmundsson, F., Hreinsdóttir, S., & Ófeigsson, B. G. (2016). Constraints on seasonal load variations and regional rigidity from continuous GPS measurements in Iceland, 1997–2014. *Geophysical Journal International*, *205*(3), 1843–1858. doi: 10.1093/gji/ggw122

Duffield, W., & Muffler, L. J. (1984). *Geothermal resources of São Miguel Island, Azores, Portugal* (Tech. Rep.). U.S. Geological Survey. doi: 10.3133/ofr84287

Dzurisin, D. (2007). *Volcano deformation: Geodetic monitoring techniques*. Springer.

D'Araújo, J., Sigmundsson, F., Ferreira, T., Okada, J., Lorenzo, M., Silva, R., ... Gaspar, J. L. (2022). Multiple inflation and deflation events from 2004 to 2016 at Fogo (água de Pau) volcano, São Miguel, Azores. *Journal of Volcanology and Geothermal Research*, 107694. doi: 10.1016/j.jvolgeores.2022.107694

D'Auria, L., Pepe, S., Castaldo, R., Giudicepietro, F., Macedonio, G., Ricciolino, P., ... others (2015). Magma injection beneath the urban area of Naples: a new mechanism for the 2012–2013 volcanic unrest at Campi Flegrei caldera. *Scientific reports*, *5*(1), 1–11. doi: 10.1038/srep13100

Elias, R. B., Gil, A., Silva, L., Fernández-Palacios, J. M., Azevedo, E. B., & Reis, F. (2016). Natural zonal vegetation of the Azores Islands: Characterization and potential distribution. *Phytocoenologia*, *46*(2), 107–123. doi: 10.1127/phyto/2016/0132

EMODnet. (2022). *EMODnet Bathymetry Portal.* https://www.emodnet-bathymetry.eu/. (Accessed: 2022-10-13)

Escartin, J., Cannat, M., Pouliquen, G., Rabain, A., & Lin, J. (2001). Crustal thickness of v-shaped ridges south of the Azores: Interaction of the Mid-Atlantic Ridge (36-39 N) and the Azores hot spot. *Journal of Geophysical Research: Solid Earth*, *106*(B10), 21719–21735. doi: 10.1029/2001JB000224

Fernandes, R., Bastos, L., Miranda, J., Lourenço, N., Ambrosius, B., Noomen, R., & Simons, W. (2006). Defining the plate boundaries in the Azores region. *Journal of Volcanology and Geothermal Research*, *156*(1-2), 1–9. doi: 10.1016/j.jvolgeores.2006.03.019

Ferreira, T. (2000). *Caracterização da actividade vulcânica recente da ilha de S. Miguel(açores): Vulcanismo basáltico subaéreo e zonas de desgaseificação. Avaliação de riscos* (Unpublished doctoral dissertation). PhD Thesis in Geology. Azores University.

Ferreira, T., Gomes, A., Gaspar, J., & Guest, J. (2015). Distribution and significance of basaltic eruptive centres: São Miguel, Azores. *Geological Society, London, Memoirs*, *44*(1), 135–146. doi: 10.1144/M44.10

Fialko, Y., Khazan, Y., & Simons, M. (2001). Deformation due to a pressurized horizontal circular crack in an elastic half-space, with applications to volcano geodesy. *Geophysical Journal International*, *146*(1), 181–190. doi: 10.1046/j.1365-246X.2001.00452.x

Forjaz, V. H., & Fernandes, N. S. M. (1975). *Carta geologica de Portugal. Noticia explicativa das folhas A e B da ilha de São Jorge (açores).* Serv. Geol. Portugal.

Gandino, A., Guidi, M., Merlo, C., Mete, L., Rossi, R., & Zan, L. (1985). Preliminary model of the Ribeira Grande geothermal field (Azores Islands). *Geothermics*, *14*(1), 91–105.

doi: 10.1016/0375-6505(85)90096-3

Gaspar, J., Queiroz, G., Ferreira, T., Medeiros, A., Goulart, C., & Medeiros, J. (2015). Earthquakes and volcanic eruptions in the Azores region: geodynamic implications from major historical events and instrumental seismicity. *Geological Society, London, Memoirs*, *44*(1), 33–49.

Geirsson, H., Árnadóttir, T., Völksen, C., Jiang, W., Sturkell, E., Villemin, T., ... Stefánsson, R. (2006). Current plate movements across the Mid-Atlantic Ridge determined from 5 years of continuous GPS measurements in Iceland. *Journal of Geophysical Research: Solid Earth*, *111*(B9). doi: doi.org/10.1029/2005JB003717

Gente, P., Dyment, J., Maia, M., & Goslin, J. (2003). Interaction between the Mid-Atlantic Ridge and the Azores hot spot during the last 85 Myr: Emplacement and rifting of the hot spot-derived plateaus. *Geochemistry, Geophysics, Geosystems*, *4*(10). doi: 10.1029/2003GC000527

Guest, J., Gaspar, J., Cole, P., Queiroz, G., Duncan, A., Wallenstein, N., ... Pacheco, J.-M. (1999). Volcanic geology of Furnas volcano, São Miguel, Azores. *Journal of Volcanology and Geothermal Research*, *92*(1-2), 1–29. doi: 10.1016/S0377-0273(99)00064-5

Haase, K. M., & Beier, C. (2003). Tectonic control of ocean island basalt sources on São Miguel, Azores? *Geophysical Research Letters*, *30*(16).

Heap, M. J., Villeneuve, M., Albino, F., Farquharson, J. I., Brothelande, E., Amelung, F., ... Baud, P. (2020). Towards more realistic values of elastic moduli for volcano modelling. *Journal of volcanology and geothermal research*, *390*, 106684. doi: 10.1016/j.jvolgeores.2019.106684

Hildenbrand, A., Madureira, P., Marques, F. o., Cruz, I., Henry, B., & Silva, P. (2008). Multi-

stage evolution of a sub-aerial volcanic ridge over the last 1.3 myr: S. Jorge Island, Azores Triple Junction. *Earth and Planetary Science Letters*, *273*(3–4), 289–298. doi: 10.1016/j.epsl.2008.06.041

Jónsson, S., Alves, M. M., & Sigmundsson, F. (1999). Low rates of deformation of the Furnas and Fogo volcanoes, São Miguel, Azores, observed with the Global Positioning System, 1993–1997. *Journal of Volcanology and Geothermal Research*, *92*(1-2), 83–94. doi: 10.1016/S0377-0273(99)00069-4

Keiding, M., Árnadóttir, T., Sturkell, E., Geirsson, H., & Lund, B. (2008). Strain accumulation along an oblique plate boundary: The Reykjanes Peninsula, southwest Iceland. *Geophysical Journal International*, *172*(2), 861–872. doi: 10.1111/j.1365-246X.2007.03655.x

Kumagai, H., Chouet, B. A., & Nakano, M. (2002). Temporal evolution of a hydrothermal system in Kusatsu-Shirane volcano, Japan, inferred from the complex frequencies of long-period events. *Journal of Geophysical Research: Solid Earth*, *107*(B10), ESE–9. doi: 10.1029/2001JB000653

Lazecký, M., Spaans, K., González, P. J., Maghsoudi, Y., Morishita, Y., Albino, F., ... Wright, T. J. (2020). LiCSAR: An automatic InSAR tool for measuring and monitoring tectonic and volcanic activity. *Remote Sensing*, *12*(15). doi: 10.3390/rs12152430

Lechner, H. N., Wauthier, C., Waite, G. P., & Escobar-Wolf, R. (2019). Magma storage and diking revealed by GPS and InSAR geodesy at Pacaya volcano, Guatemala. *Bulletin of Volcanology*, *81*(3), 1–13. doi: 10.1007/s00445-019-1277-x

Lourenço, N., Miranda, J., Luis, J., Ribeiro, A., Victor, L. M., Madeira, J., & Needham, H. (1998). Morpho-tectonic analysis of the Azores Volcanic Plateau from a new

bathymetric compilation of the area. *Marine Geophysical Researches*, *20*(3), 141–156. doi: 10.1023/A:1004505401547

Luis, J. F., Miranda, J., Galdeano, A., Patriat, P., Rossignol, J., & Victor, L. M. (1994). Ahe Azores Triple Junction evolution since 10 Ma from an aeromagnetic survey of the Mid-Atlantic Ridge. *Earth and Planetary Science Letters*, *125*(1-4), 439–459. doi: 10.1016/0012-821X(94)90231-3

Lyard, F., Lefevre, F., Letellier, T., & Francis, O. (2006). Modelling the global ocean tides: Modern insights from FES2004. *Ocean dynamics*, *56*(5-6), 394–415. doi: 10.1007/s10236-006-0086-x

Machado, F. (1959). Submarine pits of the Azores Plateau. *Bulletin of Volcanology*, *21*(1), 109–116. doi: 10.1007/BF02596510

Machado, F., & Forjaz, V. H. (1964). *Seismic swarm in the Azores, Feb. 1964 (Preliminary report)* (Vol. 15). Bol. Soc. Geol. Port. doi: 10.1007/BF02597016

Madeira, J., & da Silveira, A. B. (2003). Active tectonics and first paleoseismological results in Faial, Pico and S. Jorge islands (Azores, Portugal). *Annals of geophysics*, *46*(5). doi: 10.4401/ag-3453

Madeira, J., & da Silveira, A. B. (2013). Active tectonics and first paleoseismological results in Faial, Pico and S. Jorge Islands (Azores, Portugal. *Annals of geophysics*, *46*(5). doi: 10.4401/ag-3453

Marques, F., Catalão, J., DeMets, C., Costa, A., & Hildenbrand, A. (2013). GPS and tectonic evidence for a diffuse plate boundary at the Azores Triple Junction. *Earth and Planetary Science Letters*, *381*, 177–187. doi: 10.1016/j.epsl.2013.08.051

Marques, F., Catalão, J., Hildenbrand, A., & Madureira, P. (2015). Ground motion

and tectonics in the Terceira Island: Tectonomagmatic interactions in an oceanic rift (Terceira Rift, Azores Triple Junction). *Tectonophysics*, *651*, 19–34. doi: 10.1016/j.tecto.2015.02.026

Marques, F., Hildenbrand, A., & Hübscher, C. (2018). Evolution of a volcanic island on the shoulder of an oceanic rift and geodynamic implications: S. Jorge Island on the Terceira Rift, Azores Triple Junction. *Tectonophysics*, *738*, 41–50. doi: 10.1016/j.tecto.2018.05.012

Mattioli, G. S., Herd, R. A., Strutt, M. H., Ryan, G., Widiwijayanti, C., & Voight, B. (2010). Long term surface deformation of Soufrière Hills volcano, Montserrat from GPS geodesy: Inferences from simple elastic inverse models. *Geophysical Research Letters*, *37*(19). doi: 10.1029/2009GL042268

Mendes, V., Madeira, J., da Silveira, A. B., Trota, A., Elosegui, P., & Pagarete, J. (2013). Present-day deformation in São Jorge Island, Azores, from episodic GPS measurements (2001–2011). *Advances in Space Research*, *51*(8), 1581–1592. doi: 10.1016/j.asr.2012.10.019

Miranda, J., Navarro, A., Catalão, J., & Fernandes, R. (2012). Surface displacement field at Terceira Island deduced from repeated GPS measurements. *Journal of Volcanology and Geothermal Research*, *217*, 1–7. doi: 10.1016/j.jvolgeores.2011.10.009

Mogi, K. (1958). Relations between the eruptions of various volcanoes and the deformations of the ground surfaces around them. *Earthq Res Inst*, *36*, 99–134.

Moore, R. B. (1990). Volcanic geology and eruption frequency, São Miguel, Azores. *Bulletin of Volcanology*, *52*(8), 602–614.

Moreira, M., Doucelance, R., Kurz, M. D., Dupré, B., & Allègre, C. J. (1999). Helium

and lead isotope geochemistry of the Azores archipelago. *Earth and Planetary Science Letters*, *169*(1-2), 189–205. doi: 10.1016/S0012-821X(99)00071-0

Morishita, Y., & Hanssen, R. F. (2014). Temporal decorrelation in L-, C-, and X-band satellite radar interferometry for pasture on drained peat soils. *IEEE Transactions on Geoscience and Remote Sensing*, *53*(2), 1096–1104. doi: 10.1109/TGRS.2014.2333814

Morishita, Y., Lazecky, M., Wright, T. J., Weiss, J. R., Elliott, J. R., & Hooper, A. (2020). LiCSBAS: An open-source InSAR time series analysis package integrated with the LiCSAR automated Sentinel-1 InSAR processor. *Remote Sensing*, *12*(3). doi: 10.3390/rs12030424

Needham, H., & Francheteau, J. (1974). Some characteristics of the rift valley in the Atlantic Ocean near 36-48 North. *Earth and Planetary Science Letters*, *22*(1), 29–43. doi: 10.1016/0012-821X(74)90061-2

Nunes, J., & Oliveira, C. (1999). Actividade sísmica do vulcão do Fogo, ilha de São Miguel (açores). *Actas do I Simpósio de Meteorologia e Geofísica-Comunicações de Geofísica*, 55–60.

Nunes, J., & Ribeiro, E. (2001). Caracterizaçao da sismicidade instrumental dos açores no periodo 1950–1980. *SISMICA, Encontro Nacional de Sismologıa e Enghenaria Sısmica, Açores*.

Okada, J., Sigmundsson, F., Ófeigsson, B. G., Ferreira, T. J., & Rodrigues, R. M. (2015). Tectonic and volcanic deformationjavascript:; at São Miguel Island, Azores, observed by continuous GPS analysis 2008–13. *Geological Society, London, Memoirs*, *44*(1), 239–256. doi: 10.1144/M44.18

Okada, Y. (1985). Surface deformation due to shear and tensile faults in a half-

space. *Bulletin of the seismological society of America*, *75*(4), 1135–1154. doi: 10.1785/BSSA0750041135

Okada, Y. (1992). Internal deformation due to shear and tensile faults in a half-space. *Bulletin of the Seismological Society of America*, *82*(2), 1018–1040. doi: 10.1785/BSSA0820021018

Papoutsis, I., Papanikolaou, X., Floyd, M., Ji, K., Kontoes, C., Paradissis, D., & Zacharis, V. (2013). Mapping inflation at Santorini volcano, Greece, using GPS and InSAR. *Geophysical Research Letters*, *40*(2), 267–272. doi: 10.1029/2012GL054137

Queiroz, G. (1997). *Vulcão das Sete Cidades (S. Miguel, açores): História eruptiva e avaliação do hazard* (Unpublished doctoral dissertation). PhD Thesis in Geology. Azores University.

REPRAA. (2021). *Rede de Estações Permanentes da Região Autónoma dos açores.* `https://repraa.{A}zores.gov.pt/`. (Accessed: 2021-07-02)

Rodríguez-Molina, S., González, P. J., Charco, M., Negredo, A. M., & Schmidt, D. A. (2021). Time-scales of inter-eruptive volcano uplift signals: Three Sisters volcanic center, Oregon (United States). *Frontiers in Earth Science*, *8*. doi: 10.3389/feart.2020.577588

Sandwell, D. (1987). Biharmonic spline interpolation of GEOS-3 and SEASAT altimeter data. *Geophysical research letters*, *14*(2), 139–142. doi: 10.1029/GL014i002p00139

Sandwell, D., Mellors, R., Tong, X., Wei, M., & Wessel, P. (2011). Open radar interferometry software for mapping surface deformation. *Eos, Transactions American Geophysical Union*, *92*(28), 234–234. doi: 10.1029/2011EO280002

Schmid, R., Dach, R., Collilieux, X., Jäggi, A., Schmitz, M., & Dilssner, F. (2016). Absolute IGS antenna phase center model igs08.atx: Status and potential improvements. *Journal*

of Geodesy, *90*(4), 343–364. doi: 10.1007/s00190-015-0876-3

Searle, R. (1980). Tectonic pattern of the Azores spreading centre and triple junction. *Earth and Planetary Science Letters*, *51*(2), 415–434.

Selmke, I., Dach, R., Arnold, D., Prange, L., Schaer, S., Sidorov, D., ... Hugentobler, U. (2020). *CODE repro3 product series for the IGS.* Astronomical Institute, University of Bern. doi: 10.7892/boris.135946

Shapiro, N. M., Droznin, D., Droznina, S. Y., Senyukov, S., Gusev, A., & Gordeev, E. (2017). Deep and shallow long-period volcanic seismicity linked by fluid-pressure transfer. *Nature Geoscience*, *10*(6), 442–445. doi: 10.1038/ngeo2952

Sibrant, A., Hildenbrand, A., Marques, F., Weiss, B., Boulesteix, T., Hübscher, C., ... Catalão, J. (2015). Morpho-structural evolution of a volcanic island developed inside an active oceanic rift: S. Miguel Island (Terceira Rift, Azores). *Journal of Volcanology and Geothermal Research*, *301*, 90–106. doi: 10.1029/2003GL017500

Sigmundsson, F., Tryggvason, E., Alves, M. M., Alves, J. L., Pálsson, K., & Ólafsson, H. (1995). Slow inflation of the Furnas volcano, São Miguel, Azores, suggested from initial leveling and Global Positioning System measurements. *Geophysical Research Letters*, *22*(13), 1681–1684. doi: 10.1029/95GL01604

Silva, P., Henry, B., Marques, F. O., Hildenbrand, A., Madureira, P., Mériaux, C. A., & Kratinova, Z. (2012). Palaeomagnetic study of a subaerial volcanic ridge (São Jorge Island, Azores) for the past 1.3 myr: evidence for the cobb mountain subchron, volcano flank instability and tectonomagmatic implications. *Geophysical Journal International*, *188*(3), 959–978. doi: 10.1111/j.1365-246X.2011.05320.x

Silva, R., Ferreira, T., Medeiros, A., Carmo, R., Luis, R., Wallenstein, N., ... Sousa,

R. (2015). Seismic activity on São Miguel Island volcano-tectonic structures (Azores archipelago). *Geological Society, London, Memoirs*, *44*(1), 227–238. doi: 10.1144/M44.6

Silva, R., Havskov, J., Bean, C., & Wallenstein, N. (2012). Seismic swarms, fault plane solutions, and stress tensors for São Miguel Islandcentral region (Azores). *Journal of Seismology*, *16*(3), 389–407. doi: 10.1007/s10950-012-9275-x

Silverii, F., Pulvirenti, F., Montgomery-Brown, E., Borsa, A., & Neely, W. (2021). The 2011-2019 Long Valley caldera inflation: New insights from separation of superimposed geodetic signals and 3D modeling. *Earth and Planetary Science Letters*, *569*, 117055. doi: 10.1016/j.epsl.2021.117055

Spieker, K., Rondenay, S., Ramalho, R., Thomas, C., & Helffrich, G. (2018). Constraints on the structure of the crust and lithosphere beneath the Azores Islands from teleseismic receiver functions. *Geophysical Journal International*, *213*(2), 824–835. doi: 10.1093/gji/ggy222

Storch, B., Haase, K., Romer, R., Beier, C., & Koppers, A. (2020). Rifting of the oceanic Azores Plateau with episodic volcanic activity. *Scientific reports*, *10*(1), 1–12. doi: 10.1029/2008GC002112

Storey, M. (1982). Trachytic pyroclastics from água de Pau volcano, São Miguel, Azores: evolution of a magma body over 4,000 years. *Contributions to Mineralogy and Petrology*, *78*(4), 423–432.

Troise, C., De Natale, G., Schiavone, R., Somma, R., & Moretti, R. (2019). The Campi Flegrei caldera unrest: Discriminating magma intrusions from hydrothermal effects and implications for possible evolution. *Earth-science reviews*, *188*, 108–122. doi:

10.1016/j.earscirev.2018.11.007

Trota, A. (2008). *Crustal deformation studies in S. Miguel and Terceira islands (Azores). Volcanic unrest evaluation in Fogo/Congro area (S. Miguel)* (Unpublished doctoral dissertation). PhD Thesis in Geology. Azores University.

Trota, A., Houlié, N., Briole, P., Gaspar, J., Sigmundsson, F., & Feigl, K. (2006). Deformation studies at Furnas and Sete Cidades volcanoes (São Miguel Island, Azores). velocities and further investigations. *Geophysical Journal International*, *166*(2), 952–956. doi: 10.1111/j.1365-246X.2006.03039.x

Tryggvason, E., Dibble, R., & Okada, H. (1989). Água de Pau volcano/seismic crisis of 1989. *Final report on the UNESCO/WOVO Volcanology mission to São Miguel, Azores*, *2*.

Viveiros, F., Ferreira, T., Vieira, J. C., Silva, C., & Gaspar, J. (2008). Environmental influences on soil CO2 degassing at Furnas and Fogo volcanoes (São Miguel Island, Azores archipelago). *Journal of Volcanology and Geothermal Research*, *177*(4), 883–893. doi: 10.1016/j.jvolgeores.2008.07.005

Walker, G. P. L., & Croasdale, R. (1971). Two Plinian-type eruptions in the Azores. *Journal of the Geological Society*, *127*(1), 17–55. doi: 10.1144/gsjgs.127.1.001

Wallenstein, N. (1999). *Estudo da história eruptiva recente e do comportamento eruptivo do vulcão do Fogo (S. Miguel, Açores). Avaliação preliminar do hazard* (Unpublished doctoral dissertation). PhD Thesis in Geology. Azores University.

Wei, M., & Sandwell, D. T. (2010). Decorrelation of L-band and C-band interferometry over vegetated areas in California. *IEEE Transactions on Geoscience and Remote Sensing*, *48*(7), 2942–2952. doi: 10.1109/TGRS.2010.2043442

Widom, E., Schmincke, H.-U., & Gill, J. (1992). Processes and timescales in the evolution of

a chemically zoned trachyte: Fogo a, São Miguel, Azores. *Contributions to Mineralogy and Petrology*, *111*(3), 311–328. doi: 10.1007/BF00375204

Wright, T. J., Parsons, B. E., & Lu, Z. (2004). Toward mapping surface deformation in three dimensions using InSAR. *Geophysical Research Letters*, *31*(1). doi: 10.1029/2003GL018827

Wright, T. J., Sigmundsson, F., Pagli, C., Belachew, M., Hamling, I. J., Brandsdóttir, B., ... others (2012). Geophysical constraints on the dynamics of spreading centres from rifting episodes on land. *Nature Geoscience*, *5*(4), 242–250. doi: 10.1038/ngeo1428

Xu, X., Sandwell, D. T., Tymofyeyeva, E., Gonzalez-Ortega, A., & Tong, X. (2017). Tectonic and anthropogenic deformation at the Cerro Prieto geothermal step-over revealed by Sentinel-1a InSAR. *IEEE Transactions on Geoscience and Remote Sensing*, *55*(9), 5284–5292. doi: 10.1109/TGRS.2017.2704593

Yang, T., Shen, Y., van der Lee, S., Solomon, S. C., & Hung, S.-H. (2006). Upper mantle structure beneath the Azores hotspot from finite-frequency seismic tomography. *Earth and Planetary Science Letters*, *250*(1-2), 11–26. doi: 10.1016/j.epsl.2006.07.031

Yang, X.-M., Davis, P. M., & Dieterich, J. H. (1988). Deformation from inflation of a dipping finite prolate spheroid in an elastic half-space as a model for volcanic stressing. *Journal of Geophysical Research: Solid Earth*, *93*(B5), 4249–4257. doi: 10.1029/JB093iB05p04249

Yu, C., Li, Z., Penna, N. T., & Crippa, P. (2018). Generic atmospheric correction model for Interferometric Synthetic Aperture Radar observations. *Journal of Geophysical Research: Solid Earth*, *123*(10), 9202-9222. doi: 10.1029/2017JB015305

Zandomeneghi, D., Almendros, J., Ibáñez, J. M., & Saccorotti, G. (2008). Seismic tomog-

raphy of central São Miguel, Azores. *Physics of the Earth and Planetary Interiors*, *167*(1-2), 8–18. doi: 10.1016/j.pepi.2008.02.005

Zanon, V., & Viveiros, F. (2019). A multi-methodological re-evaluation of the volcanic events during the 1580 CE and 1808 eruptions at São Jorge Island (Azores archipelago, Portugal). *Journal of Volcanology and Geothermal Research*, *373*, 51–67. doi: 10.1016/j.jvolgeores.2019.01.028

Zbyszewski, G., & Rosa, T. P. (1977). *Os sismos de 1964 na ilha de S. Jorge (açores). Registo diário* (Vol. 3). Ciências da Terra. Universidade Nova de Lisboa.

UNIVERSIDADE DOS AÇORES
Faculdade de Ciências e Tecnologia

Rua da Mãe de Deus
9500-321 Ponta Delgada
Açores, Portugal